3-D Lidar Wind Airborne Profiling Using A Coherent-Detection Doppler Wind Lidar Designed For Space-Based Operation

Final Project Report In Response To:

"Measuring the Atmospheric Wind Profile (3D Winds): Call for Studies and Field Measurement Campaigns" NOAA Broad Agency Announcement (BAA)

Principal Investigator: Kristopher Bedka[1]

Contributors To This Report

John Cooney[1], G. David Emmitt[4], Aram Gragossian[1], Steven Greco[4], Sammy Henderson[3], Michael Kavaya[1], Konstantin Khlopenkov[2], John Marketon[1], Shelley Stover[1], and Sidney Wood[4]

Acknowledgements For Their AWP Wind Lidar Engineering and Aircraft Operations Efforts

Samantha Applin[1], Seth Begay[1], Ryan Bennett, Patrick Bookey[1], Charlie Boyer (retired)[1], Songsheng Chen[1], Maurice Cross[1], Greg Crowther[1], Joe Diamond[3], David Eckberg[1], Anjie Emmett[1], Patrick Kratovil[3], NASA Airborne Science Program, NASA Langley Research Services Directorate, Alan Little[1], David Macdonnell[1], Amin Nehrir[1], Anna Noe[1], Larry Petaway (retired) [2], Sev Rosario[2], Shane Seaman[1], Aboubakar Traore[1], F. Guy Wilson[1], Teh-Hwa Wong (retired) [5], Jirong Yu (retired) [2]

[1] NASA Langley Research Center, Hampton, Virginia

[2] Analytical Mechanics Associates, Hampton, Virginia (via RSES Contract)

[3] Beyond Photonics LLC, Boulder, Colorado

[4] Simpson Weather Associates, Charlottesville, Virginia

[5] Coherent Applications Inc., Hampton, Virginia (via RSES Contract)

[6] Bay Area Environmental Research Institute (NASA Airborne Science Program Contractor)

Table of Contents

List of Figures and Tables

highlighted in blue.

Figure 5.2.1: NASA Gulfstream-III flight tracks for the NOAA 3-D Wind Demo (left), and the WH^{2}yMSIE/APEX (right) campaigns. Dropsonde locations are shown with white X symbols. Cross-country transit flights to/from WH^{2}yMSIE/APEX are omitted from the right panel.

Figure 5.2.1.1: (left) NOAA GFS model six-hour forecasts of the 250 hPa wind speed and streamlines from the 12 UTC run on 15 October 2024. (right) 850 hPa wind barbs, geopotential height, and cyclonic vorticity. Graphics were acquired from the Tropical Tidbits website and used here with permission from the website developer (see "Terms of Use" at the bottom of https://www.tropicaltidbits.com/analysis/models/).

Figure 5.2.1.2: (left) AWP signal to noise ratio (SNR), wind speed and wind direction profiles on 15 October 2024 over the flight track shown in the upper-right panel. (lower-right) A comparison of the spatially-averaged AWP data profile and AVAPS dropsonde at 1720 UTC. The AWP spatial averaging/smoothing process is described in Section 3. White columns in the AWP data curtains indicate aircraft turns where AWP wind vector retrievals are not possible.

Figure 5.2.1.3: AWP SNR, wind speed, and wind direction curtains above an 8 km altitude, focused on the flight segment within the mid-latitude cyclone trough axis and stratosphere discussed in the text. The wind speed color bar range is compressed relative to Figure 5.2.1.2 to emphasize horizontally oriented wave features.

Figure 5.2.1.4: An ensemble of NOAA HYSPLIT back-trajectories initialized from Detroit, MI at a 5 km altitude, where AWP saw aerosol layers during flight, at 19 UTC on 15 October 2024. Back-trajectories were run to a period 120 hours prior to the initialization time. 0.25° GFS model output was used as the meteorology for this run. (right) Depictions of wildfire locations detected by MODIS, VIIRS (red), and Landsat (maroon) on 10 October displayed within the NASA FIRMS tool, showing that the trajectories overpassed many fires that could be responsible for the aerosol detected by AWP.

Figure 5.2.1.5: NASA GMAO GEOS-5 model forecast of total column aerosol optical thickness, valid at 12 UTC on 15 October 2024.

Figure 5.2.2.1: (left) NOAA GFS model six-hour forecasts of the 250 hPa wind speed and streamlines from the 12 UTC run on 24 September 2024. (right) 850 hPa wind barbs, geopotential height, and cyclonic vorticity. Graphics were acquired from the Tropical Tidbits website.

Figure 5.2.1.2: (left) AWP signal to noise ratio (SNR), wind speed and wind direction profiles on 15 October 2024 over the flight track shown in the upper-right panel. (lower-right) A comparison of the spatially-averaged AWP data profile and AVAPS dropsonde at 1720 UTC. The AWP spatial averaging/smoothing process is described in Section 3. White columns in the AWP data curtains indicate aircraft turns where AWP wind vector retrievals are not possible.

Figure 5.2.2.3: (left) An ensemble of NOAA HYSPLIT back-trajectories initialized from the time and location of a thick aerosol plume at 6 km altitude and 23 UTC on 13 November 2024. (right), HYSPLIT trajectories initialized from a thin aerosol layer in the pre-frontal airmass at 3 km altitude and 22 UTC. Back-trajectories were run to a period 120 hours prior to the initialization time. 0.25° GFS model output was used as the meteorology for this run.

Figure 5.2.2.4: (left) AWP SNR and (right) HALO 532 nm aerosol backscatter for the 13 November 2024 flight. Data prior to 22.75 (2245, vertical grey bar) UTC is based on 1200 pulse integration. 3000 pulses are integrated after 22.75 UTC.

Figure 5.2.3.1: (left) NOAA GFS model six-hour forecasts of the 250 hPa wind speed and streamlines from the 12 UTC run on 24 September 2024. (right) 850 hPa wind barbs, geopotential height, and cyclonic vorticity. Graphics were acquired from the Tropical Tidbits website.

Figure 5.2.3.2: (left) AWP signal to noise ratio (SNR), wind speed and wind direction profiles on 24 September 2024 over the flight track shown in the right panel. White columns in the AWP data curtains indicate aircraft turns where AWP wind vector retrievals are not possible. No dropsondes were released during this flight.

Figure 5.2.3.3: (left) AWP SNR derived from 1200 pulse and 256 data sample retrieval and (right) HALO 532 nm aerosol backscatter for the 24 September 2024 flight.

Figure 5.2.4.1: (left) NOAA GFS model six-hour forecasts of the 250 hPa wind speed and streamlines from the 12 UTC run on 15 November 2024. (right) 700 hPa wind barbs, geopotential height, and cyclonic vorticity. Graphics

Executive Summary

NASA Langley Research Center (LaRC), in collaboration with Beyond Photonics LLC and Simpson Weather Associates, were awarded funding as an "Objective A" project proposed to the 2022 "Measuring the Atmospheric Wind profile (3-D Winds): Call for Studies and Field Measurement Campaigns for NOAA/NESDIS" Broad Agency Announcement (BAA, NOAA NESDIS 2022). This BAA sought white papers for studies related to analyzing technologies and mission concepts for measuring 3-D winds (BAA Objective B), as well as suborbital 3-D wind measurement campaigns to demonstrate current 3-D wind profiling technologies that have a path to space (BAA Objective A). NOAA aims to gain a deeper understanding of existing 3-D wind measurement technologies and concepts to inform future space architecture planning that could potentially include 3-D wind requirements. NASA LaRC and partners proposed to conduct a suborbital 3-D wind measurement campaign extending for 60 flight hours with their Aerosol Wind Profiler (AWP) Doppler wind lidar instrument flown aboard NASA research aircraft. AWP is a coherent-detection wind lidar operating at a ~2 μm wavelength that uses optical heterodyning to measure Doppler shifts and derive 3-D wind profiles from Mie scattering by atmospheric aerosols and clouds.

Our project seeks to demonstrate:

1) *AWP wind and aerosol backscatter observations resulting from varied aerosol, cloud, and weather conditions over and offshore of the U.S.*
2) *The strengths/weaknesses of AWP and how it compares with dropsondes, GOES-16/18 atmospheric motion vectors (AMVs), and NWP model prediction.*
3) *What might data from an AWP-like sensor look like if it were collected from space?*

The project had its initial kickoff meeting in February 2023. AWP was initially slated to fly aboard the LaRC Gulfstream-3 (G-3) aircraft in May 2023 and February-April 2024. In March 2023, the project team was informed by the NASA Airborne Science Program that the G-3 was being reprioritized for other international missions during both the initially planned flight windows. The AWP team was provided NASA funding in May 2023 to rapidly fabricate components to fly aboard the NASA DC-8 to piggyback on the ecoDemonstrator flight mission, which would serve as the first phase of the AWP 3-D Demonstration. The second phase of the 3-D wind demonstration was re-scheduled to occur aboard the G-3 in September-October 2024.

NASA and Boeing partnered to conduct a contrail research campaign, based in Everett, Washington through Boeing's ecoDemonstrator program. The campaign focused on generating and analyzing data to assess sustainable aviation fuel's capacity to benefit the environment by measuring contrails with in-situ and lidar sensors. The AWP team designed and procured the required components to integrate aboard the DC-8 in August 2023, was successfully integrated aboard the DC-8, and flew throughout the month of October 2023. As ecoDemonstrator sought to measure contrails that are very small in size, the DC-8 was conducting high-frequency changes in attitude (pitch, roll, and yaw) to sample the contrails, maneuvers that are very detrimental to wind lidar measurements which require straight and level flight. In addition, lower-than-expected signal levels were being measured by the AWP, which were later found to be caused by poorly-aligned beam expanding telescopes from an industry vendor, that resulted in up to 95% signal loss. Despite these issues, 51 hours of AWP data were delivered to NOAA for their initial evaluation. The telescopes were rebuilt and realigned at LaRC in the first half of 2024 to provide excellent lidar system performance during 2024 flights.

AWP was integrated onto the G-3 in September 2024 to execute the NOAA-funded portion of the 3-D Wind Demonstration, based at NASA LaRC in Hampton, Virginia. Nine research flights were successfully executed from 18 September to 16 October across 47 flight hours. A wide variety of weather regimes and aerosol/cloud conditions were sampled, and 30 Airborne Vertical Atmospheric Profiling System (AVAPS) dropsondes were released for AWP validation to meet objectives 1) and 2) above. AWP was invited to remain onboard the G-3 and collect data during the NASA Westcoast & Heartland Hyperspectral Microwave Sensor Intensive Experiment (WH^2yMSIE) – Active Passive PBL profiling Experiment (APEX) mission, based in central California from 27 October to 15 November. 63 additional flight hours distributed across 12 flights were conducted during WH^2yMSIE/APEX in weather regimes and

aerosol/cloud conditions that differed from those sampled from Hampton, VA. 43 additional AVAPS dropsondes were released to add to the AWP validation database. Most flights featured long, straight flight segments with flight altitude above 11 km that sampled a variety of aerosol, cloud, and wind patterns necessary for addressing project objectives 1) and 2). A few other WH^{2}yMSIE/APEX flights were confined to a small region to study cloud and planetary boundary layer processes, at lower flight altitudes. Only flight data relevant for addressing project objectives were delivered to NOAA, which spanned ~74 hours. When combined with the reduced-quality ecoDemonstrator dataset, ~125 hours of AWP data were delivered which greatly exceeded the 60 hours initially proposed for the project.

AWP sampled a variety of weather regimes and aerosol/cloud distributions throughout both flight campaigns. Winds were successfully retrieved in 65-100% of all profile opportunities in cloud-free profiles and 45-95% in profiles when some cloud was present between the aircraft and surface. Winds were retrieved with 66 m to 132 m vertical bin spacing and typically with 1.5-2.0 km horizontal spacing (range depends on aircraft airspeed). AWP data agreed extremely well with dropsondes, demonstrating negligible bias and uncertainty of ~0.92 m/s (1.77 knots), while also demonstrating excellent backscatter sensitivity and vertical coverage of successful wind retrievals. The low uncertainty makes AWP a useful validation reference for GOES Atmospheric Motion Vector (AMV) products and NOAA numerical weather prediction (NWP) model output to satisfy objective 2) above. AMVs had a relatively wide range of agreement with AWP (1.47 – 4.20 m/s), depending on the spectral channel of imagery used to derive the AMVs. AMVs derived from cloud tracking were more precise than those derived from clear sky radiances from the three GOES-16/18 water vapor absorption channels. The GFS initial analysis produced winds with 1.94 m/s uncertainty which increased nearly linearly to 3.99 m/s at a 7-day (168 hour) forecast lead time. The HRRR model exhibited lower speed uncertainty with its initial analysis (~1.5 m/s) but higher uncertainty than GFS at an 18-hour lead time, the maximum HRRR forecast lead time for hourly HRRR runs.

Lidar system performance modeling was completed to simulate the expected performance and the frequency of successful wind retrieval as a function of altitude for a spaceborne AWP-like wind lidar concept called the Orbital Wind Profiler (OWP) to address project objective 3), leveraging decades of experience within the project team and existing performance modeling frameworks. OWP is expected to feature a 60 mJ and 400 Hz laser transceiver with a 2 line-of-sight (LOS) viewing perspective (equating to 200 Hz per LOS) to achieve wind vector observations, a dual 60 cm telescope architecture, and a 400 km orbit altitude. Modeling is based on a combination of 1) 2 µm wavelength aerosol backscatter distribution derived from a NASA Global Modeling and Assimilation Office (GMAO) GEOS-5 Nature Run (G5NR), 2) aerosols and clouds derived from an ECMWF T511 Nature Run, 3) a previous NASA-funded wind lidar performance parameterization, and 4) the Simpson Weather Associates Doppler Lidar Simulation Model (DLSM). Our simulations show median OWP aerosol backscatter sensitivity ranging between 10^{-5} and 10^{-6} km^{-1} sr^{-1}, which exceeded the median G5NR backscatter aggregated across the globe with lidar pulse integration durations ranging from 15 km (in the 0-2 km altitude layer), 40 km (2-5 km), and 75 km (5+ km). The DLSM indicated successful retrievals for 30-85% of all profiling opportunities throughout the troposphere and lower stratosphere (surface to 16 km altitude) at NOAA's Mid-Point (40 km) spatial resolution requirement, with the greatest frequency occurring within and near to the Planetary Boundary Layer (PBL, 0-2 km altitude) and lowest frequency in the lower stratosphere. Above 16 km, the rate of successful retrieval steadily decreased up to a 20 km altitude where aerosol backscatter diminished. The retrieval success rate increased (decreased) by about 20% when 75 km (15 km) pulse integrations are employed. This performance from OWP would be a significant improvement over Aeolus-1 Mie channel wind retrieval success rate. We expect a significant positive impact of OWP on global numerical weather prediction model performance, given the impact already demonstrated with Aeolus-1 Mie data.

1. Introduction

Measurements of 3-D winds, defined here as vertical profiles of horizontal wind fields, are necessary for understanding and improving prediction of a variety of processes such as sensible and latent heat fluxes, aerosol, dust, smoke, and pollution transport, cloud formation/evolution, and the development of mid-latitude and tropical cyclones, and severe thunderstorms. New wind profiling methods are especially needed for the planetary boundary layer (PBL), the turbulent layer adjacent to the Earth's surface where wind, temperature, and moisture observations are currently lacking or inadequate (Teixeira et al. 2021). Conventional 3-D wind profile observations from commercial aircraft, weather radars, microwave profilers, and radiosondes are sparse in space and time (Baker et al. 2014). Wind profiles derived from satellite infrared/microwave sounders (Santek et al. 2019; Zeng et al. 2024) and imager atmospheric motion vectors (AMVs) augment conventional wind observations and have had significant positive impact on numerical weather prediction (NWP) model performance (Eyre et al. 2022). Imager AMVs are only from single levels at the cloud or water vapor (WV) feature height, and sounder retrievals are envisioned to have relatively coarse vertical resolution (1.5-3 km, Zeng et al. 2024) and imprecision (6+ m/s, Ouyed et al. 2023; Santek et al. 2019). Stereoscopic imaging, where either a single satellite views a cloud from multiple angles, or two or more satellites view a cloud from different angles (e.g. GOES-East and -West), has been successfully used to derive cloud motions. The stereoscopic approach has the advantage of improving cloud top height assignment that has been known to be a leading source of error for AMVs derived from single-satellite image sequences like those from GOES (Carr et al. 2018, 2019, 2020, 2022). But, like other imager-based methods, stereo AMVs are limited to tracking cloud tops and will not provide wind information where clouds are absent, or above/below clouds.

The 2017 Decadal Survey (National Academies, 2018) notes that existing space-based wind measurements do not provide the detail and precision to resolve key processes, especially in the vertical dimension, and states a need for new orbital wind profilers in the 2017-2027 decadal timeframe. Wind measurements were cited as being needed to address 25 Earth Science and Earth Application Objectives in the Decadal Survey (National Academies, 2018, Table B.1 Consolidated Science and Applications Traceability Matrix). The need for 3-D winds is also documented, with similar requirements, in the NOAA Satellite Observing System Architecture study (NSOSA, NOAA NESDIS 2018). NOAA seeks 3-D wind data every 3-24 hours at 15-400 km horizontal and 0.5-4 km vertical resolution, with 2-10 m/s precision (Table 2 of NOAA NESDIS 2022, shown here as Table 1.1). The poorest performance (400 km, 24 hours, and 4 km vertical) is NOAA's minimum requirement, and most stringent is their maximum.

Doppler wind lidars (DWLs) have the unique ability to profile winds with high vertical resolution and precision. A DWL has been referred to as the "missing link in the Global Observing System" (Baker et al. 2014). *DWLs would strongly augment our global 3-D wind measurement constellation and complement imager AMV and LEO/GEO sounder wind profile observations.*

In recent decades, there has been an extensive array of Observing System Simulation Experiments (OSSEs), Observing System Experiments (OSEs), and other studies that have investigated the potential impact of space-based DWLs on numerical weather prediction (NWP) model performance, as well as benefits of a DWL to other space-based wind observations. The OSSEs and OSEs had been done to support space mission concepts such as the Global Wind Observing System (GWOS, Riishojgaard et al. 2012; Ma et al. 2015), Optical Autocovariance Wind Lidar (OAWL, Atlas et al. 2015), the Doppler Aerosol WiNd (DAWN) and Wind-Space Pathfinder (Wind-SP) lidars (Karpowicz and Prive 2024); a Japanese coherent-detection wind lidar concept (CDWL, Ishii et al. 2017, Baron et al. 2017; Okamoto et al. 2018), and the European Space Agency (ESA) Aeolus mission (Marseille et al. 2007, 2008). These studies universally agree that DWLs would significantly improve NWP model performance. A greater number of satellites carrying DWLs with varying overpass times, or a single DWL with multiple viewing perspectives (i.e. lines-of-sight (LOS)) were found to have an even greater impact than just a single satellite with a single LOS (Marseille et al. 2008; Ma et al. 2015). It was found that degree of positive NWP impact from a CDWL, which is solely dependent on signal from Mie cloud and aerosol backscatter, depends greatly on the backscatter sensitivity of the lidar and assumptions made about cloud porosity (i.e. model-simulated breaks in cloud cover) and a lidar's ability to penetrate through non-opaque cloud cover (Karpowicz and Prive, 2024).

Table 2. Trade ranges for 3D Wind Measurements (for type B studies)

Attribute	Minimum	Mid-Point	Maximum
Minimum Coverage Area	Close to global if possible, regional gaps acceptable	Global	Global
Update Rate[1]	24 hrs	6 hrs	3 hrs
Latency[2]	165 min	60 min	30 min
Horizontal Resolution (nadir)	400 km	40 km	15 km
Vertical Resolution	4 km	2 km	0.5 km
Uncertainty: Direction	± 15 Deg	± 10 Deg	± 5 Deg
Uncertainty: Speed	10 m/s	5 m/s	2 m/s or 10%
Vertical Extent	Mid-troposphere to just above tropopause	Surface to just above tropopause	Surface to Stratopause

[1]Update rate is the time interval between successive collections of data from the same geographical point on, or above, the surface of the earth.

[2]Data Latency is defined as the period from the time of observation of all requisite data by the satellite until the data product produced from those date is available to the user at the distribution system.

Table 1.1: NOAA NESDIS Minimum, Mid-Point, and Maximum 3-D Wind measurement requirements, outlined in Table 2 of NOAA NESDIS (2022).

Previously-simulated DWL impacts on NWP models have become reality with the Aeolus mission that flew in space from August 2018 to July 2023 (ESA 2023). For example, Rennie et al. (2021) found that Aeolus provided statistically significant improvement in short-range forecasts by the European Centre for Medium-range Weather Forecasts (ECMWF) global model. Longer forecast range verification showed positive impact that is strongest at the day two to three forecast range: ~2% improvement in root-mean-square error for vector wind and temperature in the tropical upper troposphere and lower stratosphere, and polar troposphere. Positive impact up to 9 days is found in the tropical lower stratosphere. Lower than expected Aeolus atmospheric signal detection led to solar background noise dominating Rayleigh wind error (Rennie et al. 2021), and reducing Mie channel sensitivity to only detect clouds and very thick aerosol plumes (e.g. Flament et al. 2021). Mie winds provided comparable or greater impact compared to Rayleigh later in the Aeolus mission due to better precision (3-4 m/s Mie vs 5-7 m/s Rayleigh, Rennie 2023). Other modeling centers also have found positive impact from assimilating Aeolus at regional (e.g. Feng and Pu 2023; Kiriakidis et al. 2023) to global scales (Garrett et al. 2022; Martin et al 2023). Aeolus-2, with a currently expected launch of 2030, is expected to provide higher resolution and precision which should provide in an even greater impact on NWP models (Heliere et al. 2023).

Space-based lidar data has been used to improve AMV and sounder wind observations. CALIPSO has been used to improve AMV representative-ness and height assignment which resulted in reduced AMV error (Folger and Weissmann 2014). Through an OSSE, Nguyen et al (2024) found wind profiling from an infrared (IR) sounder, which has high spatial coverage but low precision, can benefit significantly from coincident high-precision DWL data. These benefits can be harnessed through machine learning algorithms that reduce AMV bias and quantify AMV uncertainty/quality.

Given DWL's strong potential for improving global wind measurement and weather prediction, development of DWL technologies and instruments for ground, airborne, and space operation has been ongoing for several decades. There are two methods for measuring lidar backscatter signals and Doppler shifts from aerosol motions, direct-detection and coherent- (or "heterodyne-") detection. Direct-detection measures the intensity of backscatter signal

and employs an interferometer for Doppler shift discrimination. Coherent-detection involves mixing (or "heterodyning") backscattered signal with a local oscillator. The resulting radio frequency signal is processed using a Fast Fourier Transform (FFT) that reveals aerosol backscatter intensity and the Doppler shift required for wind measurement. The ESA Aeolus mission carried a direct-detection DWL called ALADIN and demonstrated that space-based DWL wind profiling is possible (Straume-Lindner et al. 2021). It measured wind speed profiles from molecular and cloud motions along a single line-of-sight (LOS) with a 355 nm UV laser. Lidar theory and experience with many ground and airborne DWLs demonstrate that coherent-detection (or "heterodyne") DWLs (CDWLs), which typically operate in near-IR wavelengths from 1.5 – 2 μm wavelengths, yield higher spatial/vertical resolution and precision wind data (Henderson et al. 2005; Lux et al. 2022). Direct-detection precision is impacted by the square root of signal return intensity, while CDWL precision is insensitive to intensity (Henderson et al. 2005). Direct-detection favors high pulse energy and strong signal return, requiring a large telescope (Weiler et al. 2021). CDWL signal return modulates the backscatter sensitivity and vertical coverage of successful wind profiles, but does not impact wind measurement precision. If backscatter above the instrument noise level is detected by a CDWL, it will measure winds with near-constant precision, *even with a single lidar pulse*, providing the potential for extremely-high spatial resolution wind measurements. Signal integration (i.e. averaging) across many CDWL pulses is used to reduce the instrument noise level in the wind retrieval process, improving sensitivity to weak backscatter conditions (Section 3). Based on experiences from several German DLR flight campaigns with a 2 μm coherent-detection DWL, Witchas et al. (2022) stated that "a 2-μm DWL is suitable as a reference instrument due to the low systematic and random errors that come along with the heterodyne-detection measurement principle of the system." A "reference instrument" refers to one with excellent precision and data quality such that it can be used to validate other wind measurements.

NASA Langley Research Center (LaRC) and industry partners have been developing CDWL technology intended for airborne and space-borne operation for over two decades (Singh et al. 2015). A LaRC team successfully invented the higher electrical efficiency Ho,Tm:LuLiF solid state CDWL laser and used it to achieve a 2 μm laser pulse energy up to 1100 mJ in 2006 (Yu 2006). In parallel with the laser advancement, a 250-mJ, 10 Hz laser was developed for the Doppler Aerosol WiNd (DAWN) airborne CDWL system (Kavaya et al. 2014). After an amplifier was damaged within DAWN during the 2010 NASA Genesis and Rapid Intensification Processes (GRIP) campaign, pulse energy was reduced to 100 mJ but beam quality improved which helped to offset the impact of the reduced pulse energy on lidar system performance. DAWN used an asymmetric silicon wedge scanner that directed the transmitted laser beam 30° off nadir. The wedge was rotated in azimuth by a programmable motor producing a conical step-stare scan. From 2010 through 2022, DAWN flew in eight NASA airborne science campaigns. These campaigns included Arctic region planetary boundary layer wind measurements (Duvivier et al. 2017; Greco et al. 2020a), hurricane and convection research (Kavaya et al. 2014; Greco et al. 2020b; Hristova-Veleva et al. 2021; Sakaeda et al. 2024; Feng et al. 2025), Saharan dust transport measurements (Nowottnick et al. 2024), and underflights and validation of the space-borne ESA Aeolus wind lidar (Bedka et al. 2021). DAWN yielded precision as high as 1.2 m/s (2.7 mph) during the 2019 NASA Aeolus Cal/Val campaign (Bedka et al. 2021). DAWN was fielded on NASA's DC-8 and UC-12B aircraft, but both are now retired. DAWN was too large and heavy to field in the new generation of smaller aircraft such as NASA's Gulfstream-III and -V, which necessitated development of a next-generation airborne DWL.

Building on their extensive experience with DWL technology and DAWN, NASA LaRC, Beyond Photonics LLC, and Simpson Weather Associates were provided funding by the NASA Earth Science Technology Office (ESTO) to develop a next-generation DWL transceiver called the Wind-Space Pathfinder (Wind-SP). The four goals of the Wind-SP program were to:

- Assess the feasibility, using the LaRC Integrated Design and Collaboration Center, of a conceptual space mission design focusing on the International Space Station JEM EF platform to obtain atmospheric aerosol and wind profile observations, and additionally validating atmospheric and lidar performance models for future wind lidar mission design optimization
- Develop and demonstrate key coherent DWL subsystems and component technologies towards space readiness that have the highest risk for space
- Demonstrate an operational ground-based wind-profiling lidar incorporating the advanced subsystem

technologies

- Develop a follow-on roadmap to achieve Technology Readiness Level (TRL) 6 for all DWL components

The Wind Space Pathfinder (Wind-SP) project began on April 1, 2017, and transceiver and other required electronics development were completed in April 2022, with a 20-month delay due to COVID-19. Many technologies needed for a space CDWL were developed and demonstrated. These technologies include the following, which will be described in further detail in this report: improved transmitters with high pulse energy and pulse repetition rate for long range wind measurements (Yu et al. 2022; Henderson et al. 2022); auto-alignment sensors and actuators for long-term maintenance of optimal CDWL performance; electronic (i.e. non-mechanical) beam path selection enabling two viewing angles allowing vector wind measurements; compact highly-stable and tunable reference lasers allowing for high-precision measurement of velocity at long ranges (> 400 km) while mitigating the impact of platform velocity. (Section 2.10 and Henderson et al. 2022). An Engineering Design Studio session at NASA Langley found that our team's design for a CDWL aboard the International Space Station Japanese Experiment Module-Exposed Facility (JEM-EF) module was feasible. Lessons learned from the Wind-SP program have led to further miniaturization and improved efficiency of the lidar transmitter, making it very suitable for space-based operation (Diamond et al. 2024; Henderson et al. 2025).

During Wind-SP transceiver development, a parallel project began to design and fabricate components required for Wind-SP transceiver integration onto a structure for airborne operation. This next-generation NASA airborne DWL instrument is called the Aerosol Wind Profiler (AWP, Bedka et al. 2024). AWP is comprised of a transceiver, a structure housing beam routing optics to direct the lidar pulses downward toward the aircraft window, two beam-expanding telescopes mounted in parallel for both off-nadir and nadir measurements, an enclosure for the telescopes, and a rotating beam-steering prism mechanism for off-nadir vertical profiling of horizontal wind vectors. AWP was flown on an engineering test flight mission aboard the NASA LaRC Gulfstream-III (G-3) in January 2023 and the DC-8 in October 2023 while piggybacking on the NASA ecoDemonstrator mission (Bedka et al. 2024). After these missions, the telescopes were found to be poorly aligned by the industry vendor, resulting in significant signal loss leading to reduced aerosol backscatter sensitivity and reduced vertical coverage of successful wind retrievals. They were rebuilt in 2024 to achieve reduced wavefront error and vastly improved performance.

NASA LaRC was awarded funding under the 2022 "Measuring the Atmospheric Wind profile (3-D Winds): Call for Studies and Field Measurement Campaigns for NOAA/NESDIS" Broad Agency Announcement (BAA, NOAA NESDIS 2022) to demonstrate how data from a coherent-detection DWL like AWP could serve NOAA's weather analysis and forecasting needs. This award was managed by the NOAA NESDIS Joint Venture program that is designed to work with the private sector, academia and other federal agencies to explore the feasibility and capability of emerging technologies spacecraft and other mission-specific tools to meet NOAA's mission requirements.

Our project seeks to demonstrate:

1) *AWP wind and aerosol backscatter observations resulting from varied aerosol, cloud, and weather conditions over and offshore of the U.S.*
2) *The strengths/weaknesses of AWP and how it compares with dropsondes, GOES-16/18 atmospheric motion vectors (AMVs), and NWP model prediction*
3) *What might data from an AWP-like sensor look like if it were collected from space?*

Additionally, the project seeks to demonstrate impact of AWP data when assimilated into NOAA NWP models. This activity is outside of the expertise of the AWP team, and is left to NWP model experts within the NOAA Data Evaluation, Exploitation, and Value Assessment (DEEVA) team to address in the months following the end of the NASA component of this project. Therefore we will not report on this activity in this document.

In Fall 2024, AWP was flown aboard the LaRC Gulfstream-III (G-3) to complete this NOAA 3-D Wind Demonstration project. The first phase of the flights from 18 September to 16 October was based in Hampton, VA, and the second phase from 27 October – 15 November was based in Santa Maria, CA and Moffet Field, CA as part of the NASA Westcoast & Heartland Hyperspectral Microwave Sensor Intensive Experiment (WH^2yMSIE) – Active

Passive PBL profiling Experiment (APEX) mission. Nearly 74 hours of AWP data were delivered to NOAA in February 2025. This combined with 51 hours of reduced quality AWP data from the October 2023 ecoDemonstrator mission greatly exceeded the 60 hours of data initially proposed for this project.

This report provides a technical description of the AWP instrument, and describes AWP data and analyses compiled throughout the Fall 2024 G-3 flight campaigns. Section 2 describes the AWP instrument, Section 3 describes wind retrieval methods, Section 4 describes airborne operations, and Section 5 describes the airborne datasets, validation with Airborne Vertical Atmospheric Profiling System (AVAPS) dropsondes (NCAR, 2025), comparisons with GOES 16+18 AMVs, and NOAA NCEP GFS and HRRR model analyses/forecasts. Section 6 describes performance modeling for a space-based CDWL instrument concept called the Orbital Wind Profiler (OWP). Section 7 summarizes the project outcomes and a path to space for OWP CDWL technology. A report providing extensive detail on how this technology could be implemented in space and technology maturation needs required for space-based operation will be provided as a separate addendum to this report.

2. The Aerosol Wind Profiler Airborne Lidar System

2.1. Pulsed Coherent Wind Lidar Transceiver

The transceiver of a CDWL is comprised of an optical bench, pulsed transmit laser, small optical and electro-optical elements of the transmitter and receiver, and high-bandwidth heterodyne signal detectors (see Sections 2.5 and 2.7). Several continuous wave (CW) lasers generate the required CDWL references: the local oscillator (LO) reference which is heterodyned with the atmospheric backscatter return signal, and the master oscillator (MO) laser(s) which generate the injection seeding reference for the transmit laser (See Section 2.6). A simplified block diagram of the AWP lidar system implemented for aircraft and conceived for space-based operation is provided in Figure 2.1.1. The only differences between aircraft and space configurations are the telescope size, large beam orientation, and elimination of the beam steering mechanism. The injection-seeding laser beam for the AWP pulsed laser is derived from the MO which sets the frequency of the outgoing laser pulses. Also, there are auxiliary detectors such as energy monitors, the MO-LO frequency offset feedback loop high-bandwidth detector, and the heterodyne detector monitoring the outgoing pulse to LO frequency difference. The gathering of these components on one optical bench originated from the need for precise alignment maintenance. Key components are located in auxiliary modules and are fiber-coupled to the transceiver, greatly reducing the heat transferred into the optical bench by the powered components and permitting efficient module arrangement.

The AWP transceiver is called the High-Power Module (HPM), and houses the high-power transmit laser as well as the receiver optical subsystem. Four other modules connected to the HPM are the Local Electronics Module (LEM, directly attached to the HPM), the Laser Controller Module (LCM), the Low Power Module (LPM) and the Thulium (Tm) fiber pump laser. These modules will be described in the Sections below. Many attributes and specifications of AWP are summarized in Table 2.1.1.

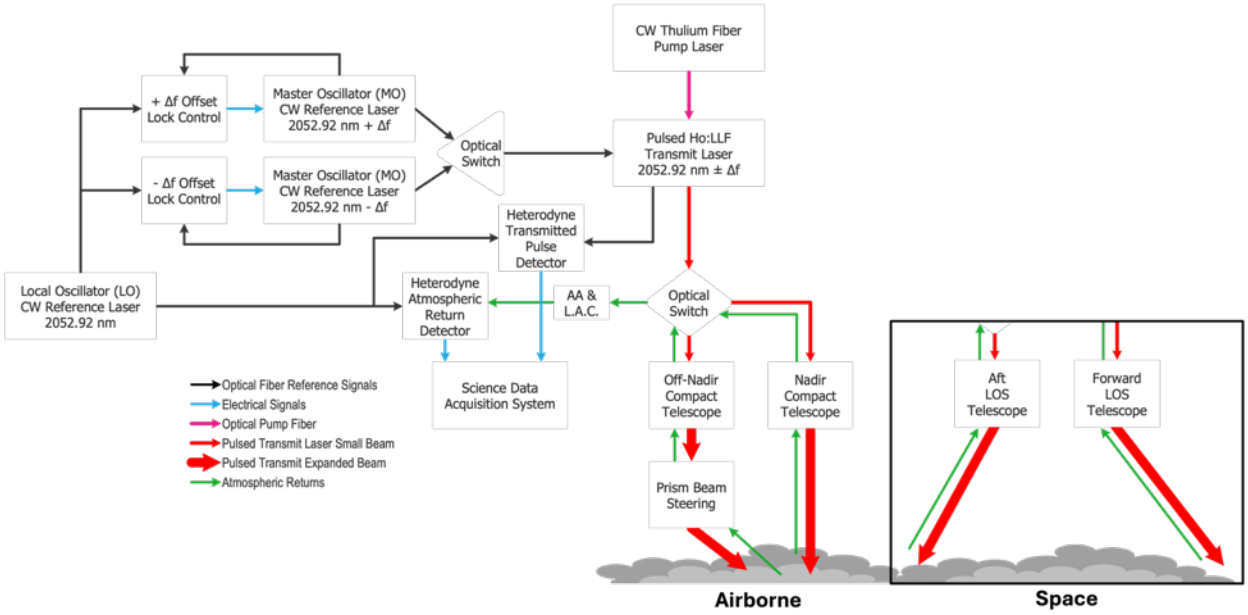

Figure 2.1.1: A simplified block diagram of the AWP lidar system described for aircraft (left) and space-based operation (inset, lower-right). For airborne operation with the off-nadir beam direction pointed forward, only one MO CW laser is required. For space-based operation where a forward and aft telescope are required, both MO CW lasers would be used.

Category	Specification
Laser Crystal	Ho:LuLiF
Wavelength	2052.92 nm
Pump Geometry	End-pumped Master Oscillator – Power Amplifier (MOPA)
Pump Source	Thulium fiber laser, 1940 nm
Pump Power	55 W to achieve 40 mJ
Pulse Energy	~40 mJ during 2024 Flights, Capable of 60 mJ
Pulse Rate	200 Hz
Average Power	8 W
Pulse Duration FWHM	~250 ns
Beam Quality M^2	1.07
Laser Cavity	3.6 m folded cavity
AWP Dimensions	0.8 x 0.6 x 0.4 m
Instrument Mass	110 kg
Telescope Design	f/8, four mirror folded, off-axis Cassegrain design, ø15 cm primary aperture, 20x expansion ratio
Telescope Dimensions	0.34 x 0.36 x 0.19 m
Digitization Rate	500 MHz
Data Storage	mySQL Database

Table 2.1.1: A summary of attributes and specifications of the AWP Doppler wind lidar system.

2.2. High-Power Module

Figure 2.2.1 shows the High-Power Module (HPM) both with its cover off (left) and on (right). With the cover off, the Carbon Fiber Composite (CFC) bench populated with the pulsed transmit laser and the receiver optical path can be seen. The white tubing routed around the CFC bench are coolant lines carrying a water-glycol mixture that maintains

a constant temperature for the laser and amplifier crystal which is circulated by an external chiller unit. The enclosure is ~25 x 16 x 10.5 inches (64 x 41 x 27 cm) high. A functional diagram of the HPM is provided in Figure 2.2.2. An electro-optical switch routes the beam between the two beam paths, to be described in greater detail in Section 2.3. The two beam paths can either exit the enclosure through the side or through the bottom. The bottom ports are used for the AWP airborne instrument configuration. Two beam paths originated from the Wind-SP Earth-orbiting concept to probe an air mass from two directions using one transceiver with two telescopes to measure horizontal vector wind profiles. The Earth-orbiting concept required many other technologies to be developed and demonstrated that have not been necessary for aircraft flight. They are discussed in Sections below.

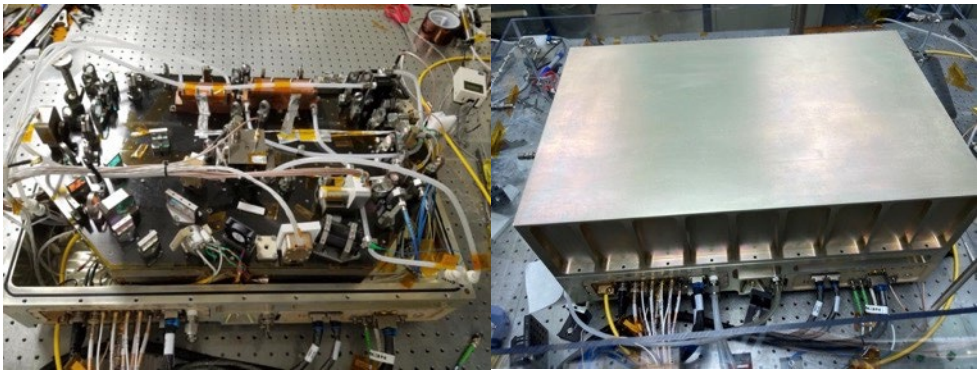

Figure 2.2.1: (left) Populated AWP Carbon Fiber Composite bench. (right) The High Power Module (HPM) with enclosure cover on. Photo source is unknown.

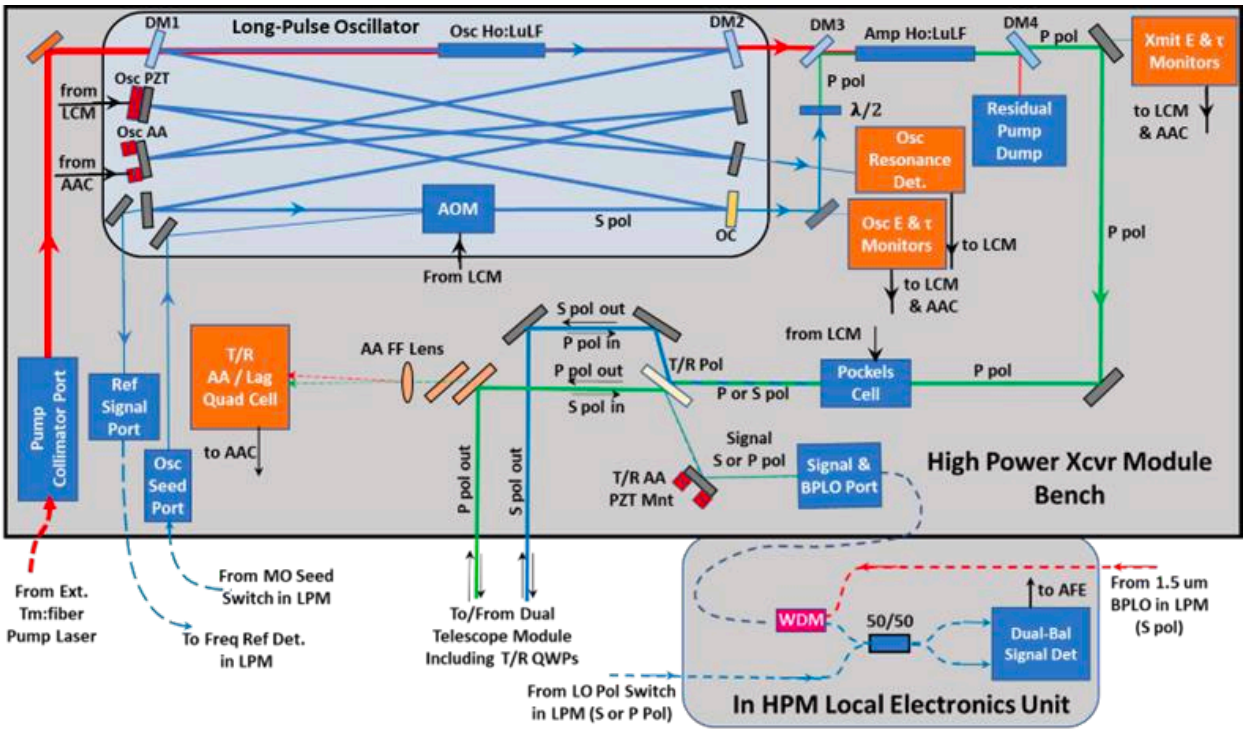

Figure 2.2.2: Simplified functional diagram of the AWP High-Power Module (HPM). Adapted from Henderson et al. (CLRC, 2022).

2.3. Transmit Pulsed Laser

The pulsed transmit laser is the heart of any lidar system. The AWP transmit laser was developed at LaRC from 2017 to 2022 within the Wind-SP program (Yu et al. 2022; Henderson et al. 2022). The Master Oscillator Power Amplifier (MOPA) architecture laser uses Ho:LuLiF crystal material and is end-pumped by a fiber-coupled Thulium (Tm) fiber pump laser at 1940 nm. The separation of the pump from the main transmit laser significantly eases thermal management of both pump and transmit lasers, and greatly improves alignment stability since thermal gradients are reduced.

The required wind velocity measurement accuracy requires a pulse duration of greater than ~180 ns, leading to a long oscillator cavity length of 3.6 m. For compactness, the cavity is folded into an 8-mirror bowtie geometry (see Figure 2.2.2, upper-left). A +27-MHz intra-cavity Acousto-Optic Modulator (AOM) is used as a Q-switch to fire the laser. To establish single-mode lasing at the specific wavelength required, the transmit laser is seeded with light from a Master Oscillator (MO) CW reference laser, which is injected into the cavity through the AOM. The pulsed laser is mounted on a CFC optical bench, where additional small beam receiver and routing optics and electro-optical beam path switching components are also located. The pump laser fiber coupler is mounted on the lower side of the CFC bench, as are beam shaping optics and routing mirrors. Pump laser light is routed to bench top side to end pump the oscillator and amplifier crystals.

The application for space requires switching the beam path between two directions to permit calculation of a horizontal wind vector. The beam path switch employs polarization of light to implement the switch via a Pockels Cell. We use traditional laser polarization designations P and S to label the two paths. These are defined only on the optical bench by the relationship of the electric field oscillation direction to the bench surface, parallel or perpendicular. (German for perpendicular is senkrecht, German for parallel is parallel; the usual use of P and S is whether the electric field oscillation is parallel or perpendicular to the plane containing the incident and reflected rays from an optical surface). The laser oscillator oscillates along the S polarization direction. It is turned to P polarization by a half wave plate. The amplifier crystal C-axis is aligned along the P polarization direction. There are a couple of advantages to setting the amplifier in this direction. The laser beam from the amplifier becomes P polarized. If the Pockels Cell is not turned on, the laser beam remains at P polarization and will transmit through the Thin Film Polarizer (TFP, denoted as “T/R Pol” in Figure 2.2.2). On the other hand, if the Pockels Cell is turned on, it changes the laser beam into S polarization, and will be reflected by the TFP. Thus, the S and P laser beam will go through different optical routes. It is directed to different beam expanders (telescopes) accordingly. The quarter wave plates (QWP) that comprise another part of the T/R switch are placed immediately before the corresponding telescopes. One beam path transmits right circular polarization and receives aerosol or cloud backscatter that is left circularly polarized. The natural reversal of the handedness occurs due to the backscatter geometry and direction reversal. The other beam path then transmits left circular and receives right circular. The received opposite handedness allows routing the backscattered light to the receiver while preventing the transmit pulse from routing to the detector and causing possible loss of signal.

Three SWIFT (Super-WIde Frequency-Tunable) solid-state lasers developed by Beyond Photonics (BP, Henderson and Hale 2017), generate the CDWL reference frequencies. All are located in the external LPM (Section 2.6). One SWIFT laser is used as local oscillator (LO) which is set at 2052.92 nm (optical frequency 1.46032 x 10^{14} Hz or 4871.11 wavenumbers). The LO frequency is selected to be in an atmospheric transmission window around the 2-µm wavelength. The other two SWIFT lasers are used as master oscillators (MO1 and MO2) for injection seeding. Both MO lasers are locked to the LO with an adjustable frequency offset. The offset frequency can be set from 150 MHz to 4 GHz for ground, airborne, or space-based applications. MO offsets are selected so that the resulting returned signal frequency corresponding to zero wind speed is centered in the receiver bandwidth, thus removing the effect of platform motion on the returned Doppler-shifted signals. By default, the optical frequency of MO1 is above the LO frequency when it is locked, and the frequency of MO2 is below the LO when it is locked. They can be reversed if needed. The locked MO1 and MO2 outputs are fed into an optical switch which selects the MO1 and MO2 alternatively to provide the desired seed laser frequency offset.

The seed beam is introduced into the laser cavity through the AO Q-switch. There are some advantages when

seeding through the Q-switch, primarily removal of the bulky optical isolators used to protect the seed laser source from the pulsed laser feedback. Therefore, there is no concern for optical damage of the seed lasers in this approach. The seeding electronics circuit and software are designed and manufactured by Beyond Photonics (BP), and employs a ramp and fire technique. The ramp and fire technique changes cavity length by moving a mirror with a PZT actuator in a triangular waveform. When resonance is detected on the up-ramp, the position is noted and the Q-Switch is triggered at that resonance point on the down ramp, firing the transmit laser. The seeding is stable in both time and frequency domain. The jitter is estimated to be less than ~50 ns in time and less than 1 MHz in frequency. The performance is far better than the DAWN lidar system which exhibits up to 6 MHz in frequency jitter.

The AWP transceiver is built on a Carbon Fiber Composite (CFC) optical bench. The laser was first built on a laboratory optical table during its development period. The performance with injection seeding was demonstrated and characterized thoroughly. It met or exceeded all the laser requirement specifications. During more than one year of development of this demonstration system, it never had any optical mirror damage issues. The laser mirrors did not damage even at ≥75 mJ pulse energy. When the transceiver optics were installed onto the CFC bench and the pulsed laser turned on, several mirrors within the laser cavity became damaged from the laser light. An investigation of the mirror reflective coatings was done, and it was determined that the coatings could handle the fluence generated by the pulsed laser. In March 2021, the NASA LaRC contamination experts were consulted to identify possible contamination sources. They performed systematic study and analysis to identify the source. The methods they used including Scanning Electron Microscopy/Energy Dispersive X-ray Spectroscopy (SEM/EDS); Raman Spectroscopy Characterization of Samples; Cascade Testing for outgassing per ASTM E2900; and Optically Stimulated Electron Emission (OSEE) characterization of Samples. Signs of surface contamination were clearly observed and characterized with Scanning Electron Microscopy / Wavelength Dispersive Spectrometer (SEM/WDS). High amounts of polyacrylonitrile (PAN), a carbon-fiber precursor material, contamination was discovered on the damaged optical mirror surfaces. This led to consideration of the CFC optical bench as a possible contamination source. It was experimentally determined that optical damage due to this contamination source would not occur if pulse energy was kept below ~40 mJ. During the Fall 2024 campaigns, the AWP laser was run at a reduced capacity, generating ~40 mJ per pulse on average to mitigate the potential for optics damage. The laser is ultimately capable of 60+ mJ that has been baselined for space-based operation (See Section 6). Pulse energy was modulated by AWP instrument operators by manual adjustment of pump laser power being injected into the laser cavity. A copy of the AWP transceiver currently being built at LaRC uses an Invar metal optical bench instead of CFC so that it can operate with 60 mJ pulse energy. A new, compact laser transmitter being developed as a space-prototype for the Orbital Wind Profiler mission concept, based on lessons learned from the Wind-SP program, also uses an Invar optical bench (Diamond et al. 2024; Henderson et al. 2025).

2.4. Thulium Fiber Pump Laser

The energy source for the AWP transmit laser is generated by an external Thulium-fiber laser operating at 1938 nm. The pump laser output is routed to the AWP transmit laser through an optical fiber umbilical. For development and laboratory work, as well as the airborne AWP instrument, the pump laser used is a commercially available, randomly polarized, 100 W Tm-fiber laser from IPG Photonics (Figure 2.4.1, right).

A TRL-5, space-qualifiable, conductively cooled pump laser was delivered by Fibertek for the Wind-SP program (Figure 2.4.1, left). Generating 100 W of linearly polarized, 1938.6 nm laser light, this pump laser has a demonstrated electrical to optical efficiency > 22%, with a beam quality of < 1.1. Linearly polarized light results in improved (compared to the IPG) pumping of the Tm:LuLiF gain medium. Laser head dimensions 11 x 14 x 4.5 inches (27.5 x 35 x 11.25 cm) and mass is 30 lbs (13.6 kg). Further description is provided by Engin et al. (2020).

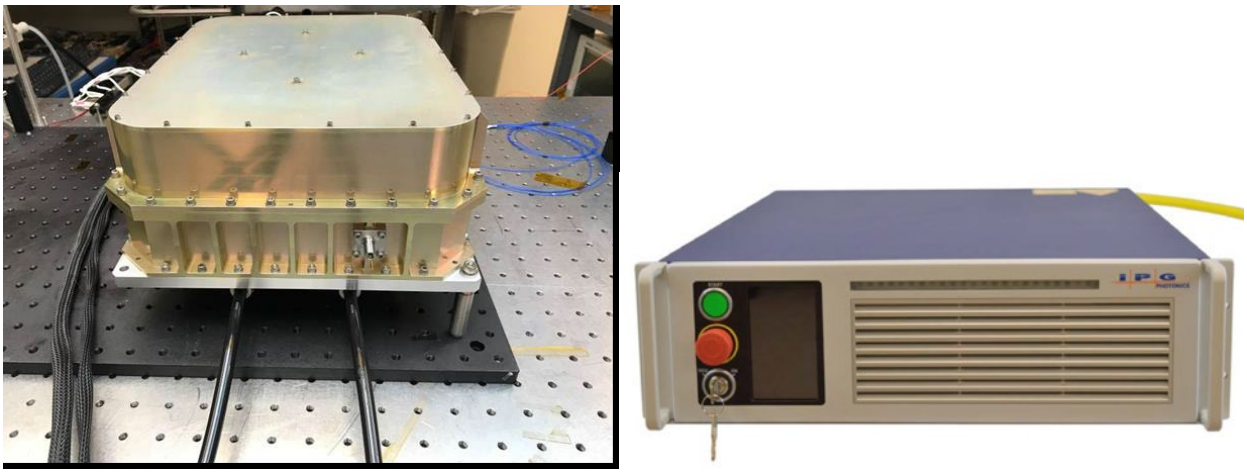

Figure 2.4.1: (left) Fibertek space-qualifiable Tm fiber pump laser intended for space-based operation, described by Engin et al. (2020). Photo source is unknown. (right) IPG Photonics 100 W Tm fiber pump laser implemented with AWP.

2.5. Local Electronics Module (LEM)

The main signal detector for the atmospheric return is a dual-balanced heterodyne detector module. This detector, other fiber-coupled components, and some electronics are packaged in the LEM enclosure that is attached to the HPM enclosure as shown in Figure 2.5.1. The atmospheric signal detector is housed here to increase signal throughput by avoiding additional, lossy fiber-to-fiber mating. Also contained in this module are the signal fiber optic network, beam path switch Pockels cell driver, and the transceiver health and monitoring electronics. The Pockels cell driver outputs fast, high-voltage pulses which can only be effectively delivered over short transmission lines. Multiple sensors within the HPM provide health and monitoring information, and are digitized in the LEM to reduce system wiring and to improve measurement quality.

The Doppler shift from aerosol backscatter signals is on the order of 0 - 0.5 picometers (pm), and needs to be measured to an accuracy on the order of femtometers (fm). The return signal strength is typically on the order of a few picowatts (pW). Direct detection of these extremely small wavelength changes in extremely weak return signals is possible, but very challenging and inevitably leads to complex detection schemes and associated electronics. High pulse repetition rates and return signal averaging improves the SNR, but with more than one pulse in flight (that is, making the round trip from the spacecraft/aircraft to the ground and back) at any given time, pulse confusion occurs, blending the aerosol return signals, and lowering SNR.

Heterodyne detection is a well-established technique for measuring the extremely small and weak Doppler shift signals from aerosol/cloud motions. A reference signal is mixed with the return signal, generating an easily detectable intermediate frequency (IF). The local oscillator (LO) generates the master reference signal, and a programmable, feedback controlled, offset locking circuit precisely sets the master oscillator (MO) continuous-wave (CW) laser frequency at a specified offset from the LO. The offset is calculated to compensate for the spacecraft/aircraft platform velocity induced Doppler shift plus sufficient offset such that zero frequency is in the center of the receiver electronic bandwidth.

There are two key elements in the AWP CDWL heterodyne receiver: a 50/50 fiber optic coupler/splitter (“fiber coupler” hereafter) and a dual-balanced receiver. The atmospheric return signal arrives at the instrument optical aperture, is collected by the telescope, and is directed to the receiver collimator input aperture. The receiver collimator injects the received signal into one input leg of the fiber coupler, and a portion of the LO signal is injected into the second input leg of the fiber coupler. Heterodyning between the LO and atmospheric signals occurs *optically* within the fiber coupler, and 50% of the resulting IF signal is present on each of the fiber coupler output legs. The 2053 nm laser wavelength corresponds to a carrier frequency of ~146 THz. Optical heterodyning down-converts these THz input signals into a 25 MHz to 250 MHz IF signal, which is easily detected and digitized at 500 mega-

samples per second (MSps). The offset frequency is set such that zero wind speed occurs at the mid-point of the receiver passband, or ~ 137 MHz. This zero point is calibrated against a ground return, presumably not moving thus having zero wind speed. With careful selection of lidar parameters, a 1 MHz Doppler shift corresponds to 1 m/s wind speed, resulting in a detectable wind speed range of ± 110 m/s from the current AWP instrument. Wind speeds exceeding 110 m/s are known to occur in extremely strong jet streams, and could be measured with a wider bandwidth receiver and ≥1 giga-sample per second (GSps) digitization rate. Each output leg of the fiber coupler is connected to a room-temperature, extended-range InGaAs detector on the balanced receiver. Such InGaAs detectors have been previously qualified for space-based operation (Joshi and Datta 2018). Optical amplification of the received signal is achieved by increasing the LO power being injected into the fiber coupler. With sufficient LO power injection, LO shot noise dominates all other noise sources, such as detector dark current and background light. The dual-balanced receiver inherently cancels excess LO intensity noise, allowing for quantum shot noise limited detection. Further details about heterodyne detection can be found at RP Photonics (2025).

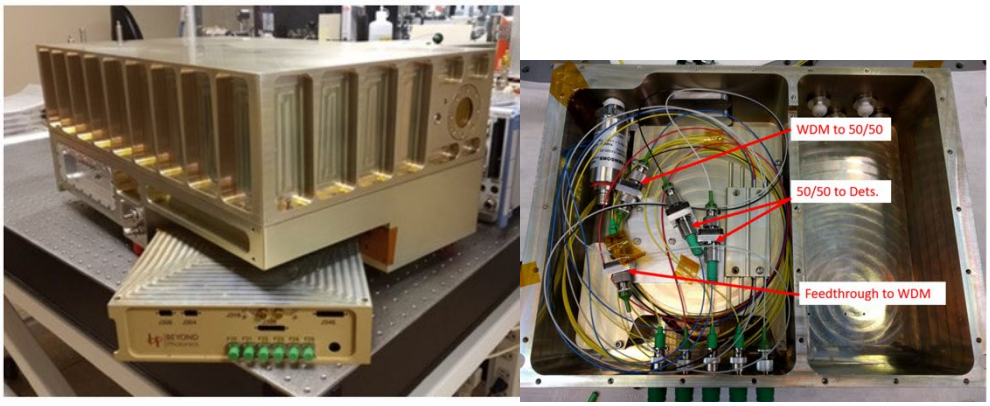

Figure 2.5.1: (left) Local Electronics Module mounting inside HPM (partially removed from HPM), and (right) top view. Photos taken by Kristopher Bedka (NASA LaRC).

2.6. Low-Power Module (LPM)

There are three CW lasers, a SWIFT LO laser and the two GHz-tunable and controllable SWIFT MO lasers, designed and manufactured at Beyond Photonics, LLC, that are separately packaged in a rack-mountable LPM that is 16 x 13.6 x 3.1 inches (40.6 x 34.5 x 7.9 cm). The LPM with its top removed is shown in Figure 2.6.1. The LPM also contains an optical fiber network, fiber switches for MO selection, the 1550 nm CW reference laser used for auto-alignment. Also located within the LPM are a heterodyne reference receiver used to monitor the frequency of each transmitted laser pulse, and the two MO offset locking circuits with wide bandwidth receivers providing a heterodyned feedback control signal. The LPM connects to the HPM with fibers and can therefore be conveniently connected while being situated in an external equipment rack.

For a space mission, the time of flight for light to travel from a satellite orbiting at 400 km (457 km slant path range at 30° off-nadir angle) to the surface and back is < 3 milliseconds (ms). The RMS frequency variation of the LO over 3 ms is < 50 kHz which translates into only a 5.1 cm/s RMS velocity error. This is more than sufficient for atmospheric wind measurement applications. Since we precisely measure the transmitted wavelength on a per-pulse basis using the outgoing pulse frequency monitor detector, which compensates for differences between shots, any RMS fluctuation of the frequency of the two MO lasers is not very important. Even so, we note that the RMS fluctuation in the frequency of these two SWIFT MO lasers is below 100 kHz over 3 ms. So that all Doppler-shifted transmitted frequencies stay within high-transmission atmospheric windows, the LO is specified with no more than 5 GHz (0.07 nm) frequency drift from 2052.92 nm over its lifetime.

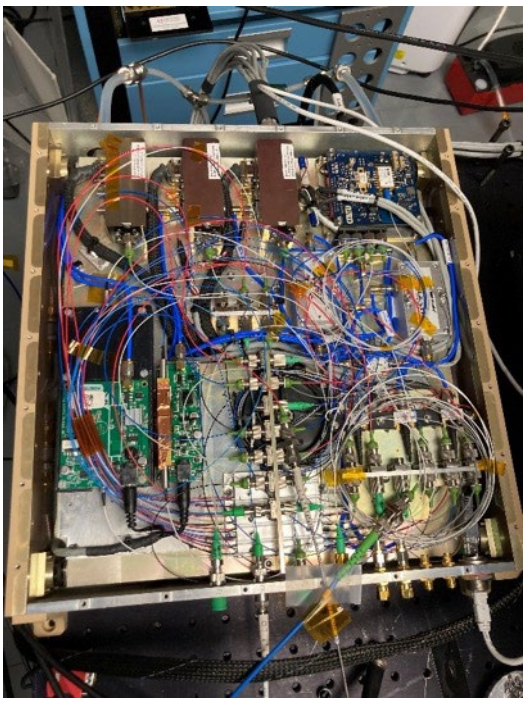

Figure 2.6.1: The AWP Low Power Module (LPM) with cover removed. The SWIFT LO and MO units are the brown rectangles at the top of the module. Photo source is unknown.

2.7. Optical Detectors

There are four heterodyne optical detectors and six intensity detectors in the AWP transceiver. The six intensity detectors are all in the HPM. Their functions are 1) oscillator cavity resonance detector as part of the injection-seeding ramp and fire subsystem, 2) the oscillator output energy monitor, 3) the oscillator temporal profile monitor, 4) the amplifier output energy monitor, 5) the amplifier temporal profile monitor, and 6) an extended-wavelength InGaAs quad cell detector as part of the auto alignment subsystem that maintains the alignment of the receiver axis to the transmitter axis. The functions of the four heterodyne detectors are 1) the dual-balanced atmospheric return signal detector in the LEM that mixes the backscattered light with the LO, 2) the outgoing pulse frequency monitor in the LPM that mixes a fraction of the transmitted pulse with the LO, and 3-4) dual heterodyne detectors in the LPM that are part of the two MO to LO frequency offset controller subsystems for the two MO lasers.

2.8. Beam Expanding Telescopes

Two nominally identical beam expanders (telescopes) are installed in AWP, one per beam path. The telescopes expand the beam from a 7.5 mm to 150 mm diameter for sampling the atmosphere, and then condense the backscatter return signal back to 7.5 mm. This small beam is further condensed and collimated into a fiber-optic cable and the dual balanced receiver described above. The telescopes are a compact, four-mirror folded, off-axis, f/8 Cassegrain design, and each occupies a volume of approximately 34 cm x 36 cm x 19 cm. The primary (M1) and both intermediate (M2, M3) mirrors have a protected gold coating. A dielectric coating is used on the quaternary mirror (M4) for improved laser damage threshold.

To minimize misalignment due to thermal changes, the majority of the telescope is aluminum (frame, plus M1 and M2). To obtain a polishable optical surface, M1 and M2 are nickel-plated, polished, and the optical surface is protected gold. M3 is a fused silica element with protected gold coating, and M4 is a calcium-fluoride (CaF) element, with a dielectric reflective coating. As initially delivered by the vendor, the telescopes were poorly aligned, achieving at best $\lambda/3$ (RMS) @ 2053 nm wavefront error that did not meet requirements (See Section 4 for further discussion). Wavefront error is a key indicator of optical system performance. Minimizing telescope wavefront aberrations is

essential for achieving optimal image quality, resolution, and overall system efficiency. After realignment at LaRC, these same telescopes achieved a transmitted wavefront error of better than λ/20 (RMS) at 2053 nm, meeting requirements.

Two key issues drive the CDWL preference for the off-axis reflective telescope configuration:

- The transmitted laser pulse is a Gaussian profile. The central obscuration of an on-axis telescope blocks the energy peak and can result in significant energy loss. While annular beam shaping can reduce energy loss due to the obscuration, this beam shaping adds unnecessary complexity and there may be adverse effects on lidar system efficiency.
- Diffraction off the edges of the secondary mirror and the associated support structure negatively impact both the transmitted and received beams, again adversely impacting lidar system efficiency.

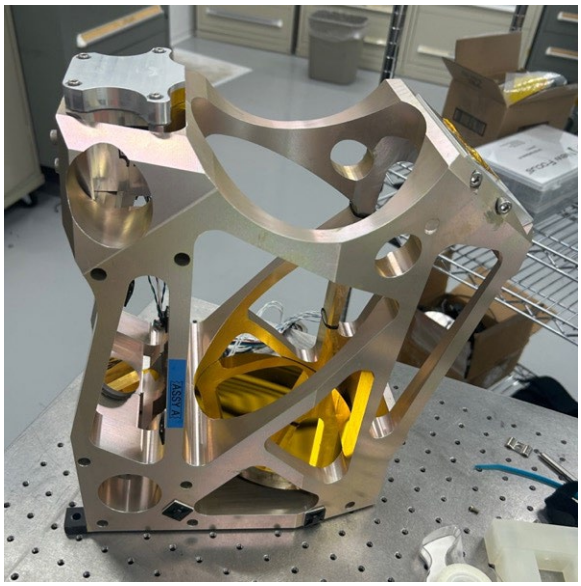

Figure 2.8.1: An AWP beam expanding telescope, photographed while sitting up-side down in a LaRC laboratory. The 15 cm diameter primary mirror with gold coloring is located at the bottom of the telescope, and the expanded beam would leave the AWP instrument and be transmitted into the atmosphere through the circular opening at the top. Photo taken by Kristopher Bedka (NASA LaRC).

2.9. Silicon Prism Scanner

AWP's azimuthal beam steering for the off-nadir path is accomplished by rotation of a symmetric silicon beam steering prism. The basic mode of operation for this assembly is start-slew-stop-sample. The custom rotation stage was designed to complete a 90° start-slew-stop motion sequence in less than one second, and has been demonstrated at ~350 ms. A brushless DC servo motor is coupled to the rotor through a 5:1 reduction belt drive, and three large-bore bearings support the prism and the rotor components. Silicon was selected for the prism material because of its advantageous index of refraction n=3.4484 at 2.05 µm. The surfaces of the silicon prism have an 11.9° separation angle, resulting in a 30° beam deflection angle (Figure 2.9.1-left). Mounting the prism at an angle to the incident transmitted beam both eliminates back-reflections of the high-power laser pulse and maximizes beam quality by reducing the elliptical distortion typical of a wedge beam director, such as that used with the NASA Doppler Aerosol WiNd (DAWN) instrument. The prism has an anti-reflective coating on both surfaces (Figure 2.9.1-right), minimizing optical surface losses and balancing coating-induced stresses on the optical element.

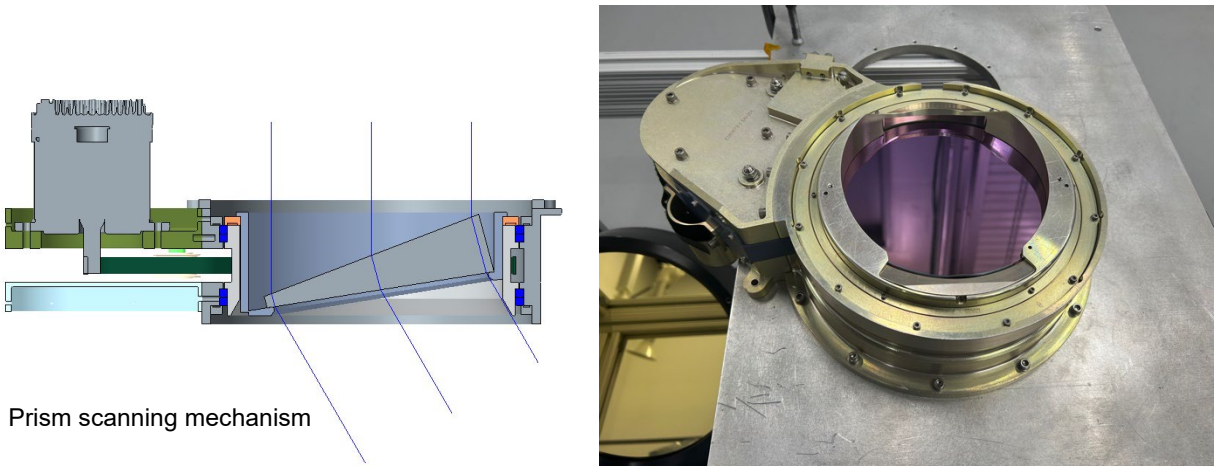

Figure 2.9.1: (left) A schematic representation of the AWP rotating symmetric silicon beam steering prism mechanism. (right) A photo of the AWP beam steering prism mechanism from its underside. The AWP lidar beam would be directed 30° off-nadir and upward from the perspective of this photo. Photo taken by Kristopher Bedka (NASA LaRC).

2.10. New Technologies in AWP Required for Space Operation

The development of the AWP transceiver was initially funded with a goal of advancing the CDWL technologies for a future Earth-orbiting mission. However, this goal involved much more than just hardening existing technologies. The space mission concept was in a very different environment than an aircraft and required additional capabilities and matching technologies to succeed. Several of these space-required technologies were successfully developed and are utilized in the application of the transceiver to aircraft flights. Table 2.10.1 provided a summary of these technologies and their applications.

New Technology	Space Application
Solid-state dual LOS beam path switch utilizing polarization	Select fore or aft LOS to have two perspectives into an air volume for vector wind profiling
Solid-state LO linear polarization direction rotator	Ensures LO linear polarization aligns with backscattered light dominant polarization
Dual tunable MO lasers with feedback to set LO offset from 150 MHz to 3 GHz	Compensate for spacecraft motion Doppler shift of ±3 GHz (fore/aft LOS). Eliminates need for very wide bandwidth dual balanced heterodyne receiver
Solid-state MO laser switch to select cavity seeding beam	Ensure correct MO laser is used for seeding beam depending on fore or aft LOS
Laser oscillator cavity auto-alignment subsystem	To maintain oscillator cavity alignment for maximum pulse energy
Transmit to receiver axes auto-alignment subsystem	To maintain transmit-receiver axes alignment for maximum photon efficiency

Table 2.10.1: New CDWL technologies demonstrated within the Wind-SP program and AWP instrument

3. Data Acquisition and Wind Retrieval Methods

The following text discusses AWP airborne data acquisition and wind retrieval methods. Section 6 will further elaborate on spaceborne data acquisition and wind retrieval, along with a short summary of coherent Doppler wind lidar signal detection theory.

AWP operated with two LOS during the Fall 2024 flights, oriented at a +/- 45° azimuth from the aircraft nose, with an adjustable number of pulses per LOS depending on the science goals of each flight. Figure 3.1 provides an illustration of the AWP scan pattern for the following discussion. While the scanner moves between the LOS's, the

polarization of the light is flipped via a Pockels Cell (Section 2.3), and the beam is directed to the nadir telescope typically for a 1 second period. In its most common mode of operation during the Fall 2024 campaigns, AWP generated a sequence of pulses at one LOS (e.g. 'LOS 1') for a 3 sec period, then briefly switched to nadir, then generated a 3 sec pulse sequence at the other LOS (e.g. 'LOS 2'). Then the scanner remained at the LOS 2 and pulsed again for 3 sec before going back to nadir and then returning to LOS 1. Half of the pulse sequence from LOS 1 (3 sec) could be paired with LOS 2 to derive a wind vector. Alternatively, the entire sequence from LOS 1 (6 sec) from adjacent scans could be paired with the entire 6-sec sequence from LOS 2 to integrate more pulses together and improve backscatter sensitivity. When data from an LOS is re-used for adjacent wind vector retrievals, the vector wind profile is assigned to the coordinate where the azimuth switches from LOS 1 to LOS 2. When the 1 sec for nadir profiling is accounted, wind vector profiles are spaced 7 sec apart, equating to 1.6 km spacing, assuming a 225 m/s airspeed. Note that when the aircraft is flying at 12 km above the surface, the intersection between the two LOS lidar beams and land/ocean surface are 10 km apart. In areas with sharp wind gradients, where LOS 1 samples one side of the gradient, and LOS 2 samples the other, there can be some disagreement and error in the wind vector profile that is unavoidable, but also very rare in reality.

After a pulse is generated and exits the aircraft, backscattered light is detected and converted to electrical signals that are digitized with an analog to digital converter (ADC) operating at a 500 megasamples per second (MSps). 65528 8-bit data samples are stored per pulse in a mySQL database. The sample count and digitization rate correspond to a slant path range of ~19.6 km or a vertical range of ~17 km. This is sufficient to completely profile the atmosphere from an aircraft flying at 13 km to sea level. In addition, it provides a large number of samples beneath the surface to derive a noise floor, required for aerosol backscatter signal peak detection described below. Examples of 8-bit digitized raw signal counts for one particular pulse generated at 1935 UTC on 15 November 2024 are shown in Figure 3.2-left. Some samples prior to the laser pulse emission are initially recorded. Then, once the pulse is emitted, light reflection from the aircraft window and other optics temporarily saturates the detector, which causes a ~200-meter blind spot and gap between the aircraft altitude and the first valid wind retrieval bin. As shown by Figure 3.3, there are many aerosol layers between the aircraft and ground at this time, which are indiscernible in the raw signal data. Backscatter from a broken stratus cloud at 1 km altitude appears as a narrow area of slightly higher signal return. The backscatter from the land surface is extremely strong. A significant fraction of laser light at 2-µm wavelength is absorbed by water, and due to the 30° incident angle of the AWP pulse, there would be an extremely small and typically undetectable surface return if this data were collected over ocean.

The wind retrieval method for AWP is largely based on Kavaya et al. (2014), which describes methods applied to DAWN data from a previous NASA flight campaign. The range resolution of a wind retrieval is modulated by a combination of the laser pulse duration and the number of data samples used in the wind retrieval calculation. Both the transmitted laser pulse and the backscattered light travel at approximately the vacuum speed of light c=299,792,458 ms^{-1}. Following Kavaya et al. (2014), the AWP pulse has an estimated duration of 250 ns (t_l), which corresponds to a 37.5 (32.5) m slant-path (vertical) bin distance. As will be described below, AWP wind retrievals are derived from either 256 or 512 data samples. 256 samples at 500 MSps digitization equates to 76.8 meter slant path range for round trip travel at the speed of light. This becomes 66.5 meters when projected into the vertical, or 132 meters for 512 samples. In practice, the vertical spacing between retrieval bins can be set to any user-defined interval, 33 meters for example, but this would require half the samples to be re-used in each bin. AWP wind products are generated with 66 meter spacing such that independent packets of samples are used in each bin.

We briefly summarize Kavaya et al. (2014) for subsequent processing steps here. Based on the aircraft attitude and heading, the laser pointing vector at each of the two azimuths is translated from an aircraft-relative to a north-east-down coordinate system. AWP records two channels of data: 1) samples from the transmitted laser pulse heterodyned with the local oscillator (LO) CW reference to enable computation of the outgoing laser pulse reference frequency, and 2) samples from light backscattered by the atmosphere that are also heterodyned with the LO (Figure 3.2-right). A Fast Fourier Transform (FFT) analysis is performed on the reference frequency channel data, and the atmospheric signal return channel data for each pulse and each range gate of that pulse using either 256 or 512 data samples, zero padded to achieve a 1024 or 2048 sample size. The result of the FFT analysis is a power spectrum (also referred to as a periodogram) for each range gate. Use of a greater number of samples in the FFT analysis improves

sensitivity to weak aerosol backscatter conditions, but coarsens the vertical resolution of the resulting wind retrieval. The periodograms from all pulses at an LOS are aligned with respect to reference frequency from each pulse and then averaged across all pulses for each of the two LOS. Averaging minimizes the random noise while the signal from true atmospheric backscatter remains prominent.

We then search for a signal peak within the periodogram. Selection of the correct peak provides very accurate wind velocities, while selection of a noise peak in the spectrum results in a random wind velocity number within the processing search bandwidth. For this reason, the most important CDWL performance metric is the probability of selecting the correct peak. The frequency of the peak is the key piece of information used to derive aerosol or cloud motion (i.e. the wind). A description of this process as applied to airborne data is described here. Further theoretical discussion on peak discussion and computation of SNR is provided in Section 6. A signal peak is identified by comparing the amplitude of a particular signal return maximum within the periodogram to the standard deviation of the instrument noise floor. The instrument noise floor is derived by averaging periodograms from data samples from below the ground/ocean surface, where we know the signal return is entirely noise. The variance of the noise floor is derived, and if a signal peak amplitude is at least 2.75 standard deviations (SD) greater than noise floor, it is considered a valid aerosol backscatter signal. Our experience indicates that lowering this SNR threshold to 2 SD can result in a greater number of good peak detections, but noisy/errant detections also increase significantly, so 2.75 SD was a good compromise to err on the side of delivering the highest quality data. The aircraft airspeed projected onto the two azimuths imparts a frequency shift that is subtracted from the peak frequency of the averaged periodograms. The difference between the reference frequency and the aircraft-motion corrected signal peak frequency is used to derive the LOS wind speed. This process is repeated for all vertical range bins above the surface altitude, derived from the intersection of each LOS with the NOAA 30 arc-second ETOPO Global Relief Model (NOAA NCEI, 2022). The vector wind speed and direction are then derived from the dual LOS wind speed profiles, with knowledge of the LOS orientation in the north-east-down coordinate system. Two SNR profiles are recorded per vector wind profile, but only the higher of the two SNRs for a particular altitude bin is recorded in the AWP NetCDF data product file.

Periodograms at 4 altitude bins (0.5, 1, 3, and 9 km) derived from integrating an increasing number of lidar pulses (50, 300, 600, and 3000), for the same time featured in Figures 3.2 and 3.3, are shown in Figure 3.4a-d. The noise floor derived from below-ground samples is shown in green. Both the standard deviation and mean of the noise floor is greatest when 50 pulses (or “shots”) are integrated. This steadily decreases with increasing pulse integration. The variance of the signal return (blue line) also decreases with increasing integration. Even with just 50 shots, prominent signal peaks are evident at 0.5 and 1.0 km altitude. A discernable peak at 3 km becomes apparent with 600 shots, half of the number of shots typically collected per LOS from each scan during most AWP flights during the Fall 2024 campaigns. A peak from extremely thin aerosol at 9 km altitude became apparent with ~2000 shots and remained prominent with 3000 shots.

A visualization of the impact of increasing integration on the Signal to Noise Ratio (SNR) and wind speed curtain is provided in Figure 5.2.4.3 later in this report. It is evident that SNR within aerosol plumes becomes increasingly evident relative to the background noise, and the wind curtain becomes more covered with successful retrievals, with increasing integration. Integration using 512 sample FFT data with 3000 pulses further improves SNR and vertical coverage beyond that from 256 FFT and 3000 pulses. *This highlights the utility of adaptive integration with heterodyne Doppler wind lidar signals to detect wind and aerosol at a variety of spatial scales.* For example, numerical weather prediction centers such as NOAA NCEP may seek wind data at relatively coarse spatial scales, but with as much vertical coverage of wind data as possible, which would necessitate longer signal integration and over deeper vertical layers. Other users such as the planetary boundary layer (PBL), tropical cyclone, and severe weather forecasting or research communities may desire wind retrievals over shorter spatial scales that emphasize the PBL where aerosol concentrations are typically greater, permitting shorter and shallower integration to achieve a successful wind retrieval. In the released AWP data products, if sufficient signal for wind retrieval was detected with 256 sample / 66 m processing, then this data was recorded at a particular altitude bin. If signal was insufficient at the highest resolution, we attempt retrieval with 512 sample / 132 m processing.

Quality-controlled (QC), weighted-average “smoothed” winds were also produced through a two-step

correction and smoothing process designed to mitigate the impact of aircraft attitude changes and measurement noise on the wind curtains. AWP wind retrievals require a stable observation platform to derive a wind vector. To address this, we removed large changes in heading or aircraft attitude (roll and pitch) over short time periods to mitigate errant wind measurements. During the QC process, we removed AWP data with |aircraft roll| > 3° or altitude changes between consecutive profiles > 0.5 km. This initial QC step ensures that unreliable measurements are excluded from further analysis. Following the QC, cubic spline interpolation was independently applied to the u- and v- component winds to fill data gaps resulting from these removals. Interpolation was performed across these unstable flight periods, provided at least one valid, finite AWP wind measurement was within ±75 seconds before and after the flagged event. 75 seconds corresponds to a ~17 km distance at aircraft cruise speed. This interpolation step ensures continuity in the dataset by reconstructing wind values across short periods of potentially compromised aircraft stability. Following interpolation, an arithmetic weighted mean smoothing was independently applied to u- and v- component winds to reduce noise and further improve data quality. Here, the smoothing kernel was defined to include all measurements within ± 75 seconds of the target measurement, as well as those within two vertical bins in altitude, specifically focusing on regions where the roll or altitude thresholds had been exceeded. Weights for the smoothing kernel were assigned based on the temporal and vertical (altitude) distance from the target measurement, with measurements farther away in time and space contributing less influence on the final smoothed value than the central value in the kernel. After this targeted smoothing step of unstable flight regions, the same weighted mean smoothing kernel was applied across an entire flight, extending the smoothing beyond just the high gradient roll/altitude regions to ensure consistency and minimize residual noise throughout the component wind fields. This process has the net effect of encapsulating spatial wind variability into the smoothed product, while also filling in data gaps associated with unstable aircraft attitude.

The only notable issue the AWP team experienced while in the field was unreliable performance of an Inertial Navigation System (INS) / Global Positioning System (GPS) unit mounted directly within the AWP instrument. The intent of this unit is to provide time-synchronized aircraft attitude, altitude, airspeed, and geographic position for each of the 200 Hz AWP lidar pulses, information critical for wind retrieval. The AWP INS/GPS was recording errant aircraft heading drifts at random times during flights, which negatively impacted real-time, onboard wind retrieval. Other data such as pitch, roll, and airspeed were accurately recorded. These heading drifts were difficult to diagnose for the first several flights when they were encountered, causing some instrument downtime on 26 September, and the 3 and 16 October flights while instrument operators tried to diagnose the issue. The Gulfstream-3 aircraft also records INS/GPS data at 10 Hz from another unit located in the aircraft. Extensive time was spent after the campaigns comparing the Gulfstream-3 INS/GPS with the AWP unit data, and correcting some biases found in the Gulfstream-3 data. After bias correction, a combination of AWP and Gulfstream-3 (time interpolated to 200 Hz) data were used in the wind retrieval. But the time interpolation does incorporate small uncertainty (~0.2 m/s) into the wind retrievals that is very difficult to eliminate.

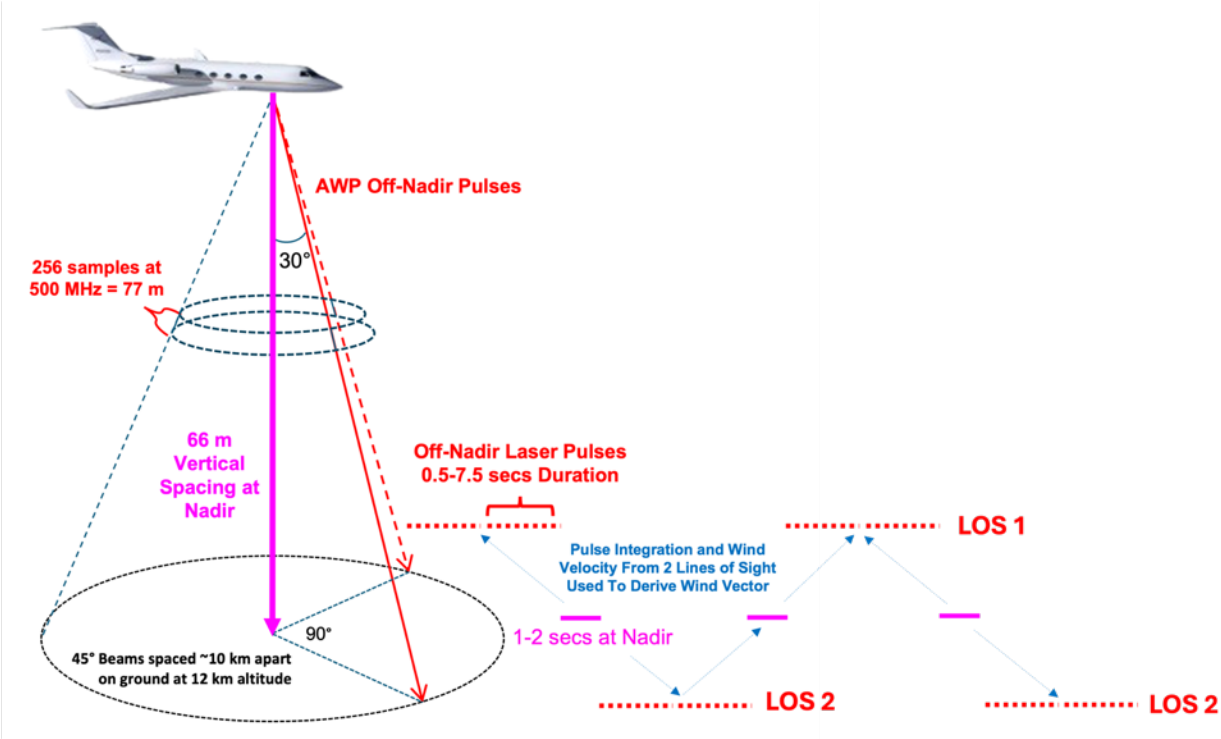

Figure 3.1: AWP concept of operations for airborne wind vector profiling.

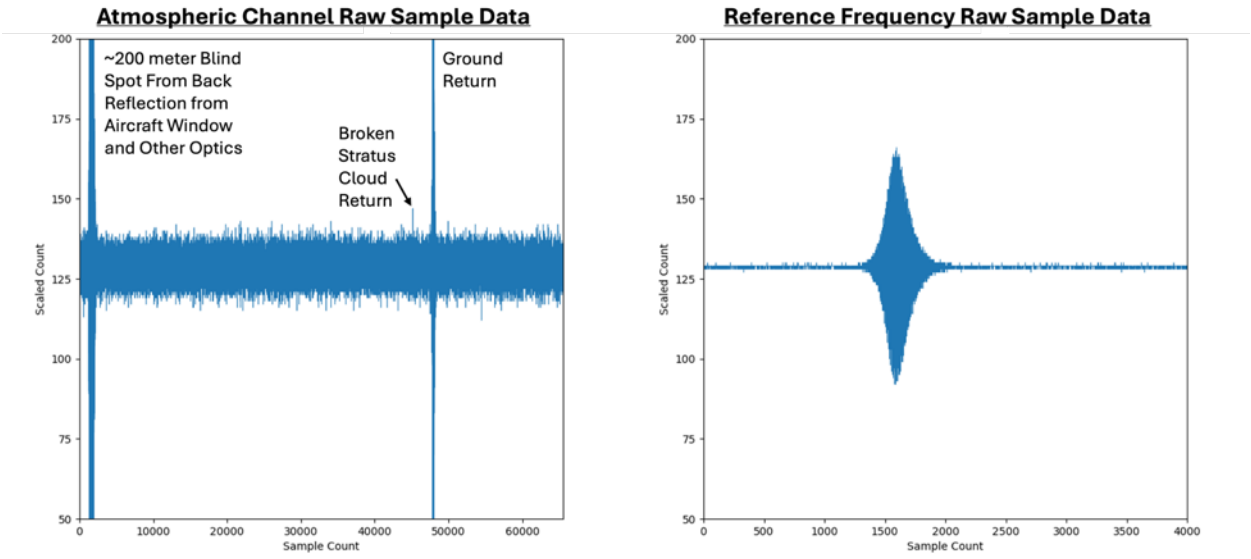

Figure 3.2: Digitized raw signal return from one AWP pulse from the atmospheric channel (left) and the reference frequency channel (right), corresponding to 1935 UTC on 15 November 2024 shown in Figure 3.3.

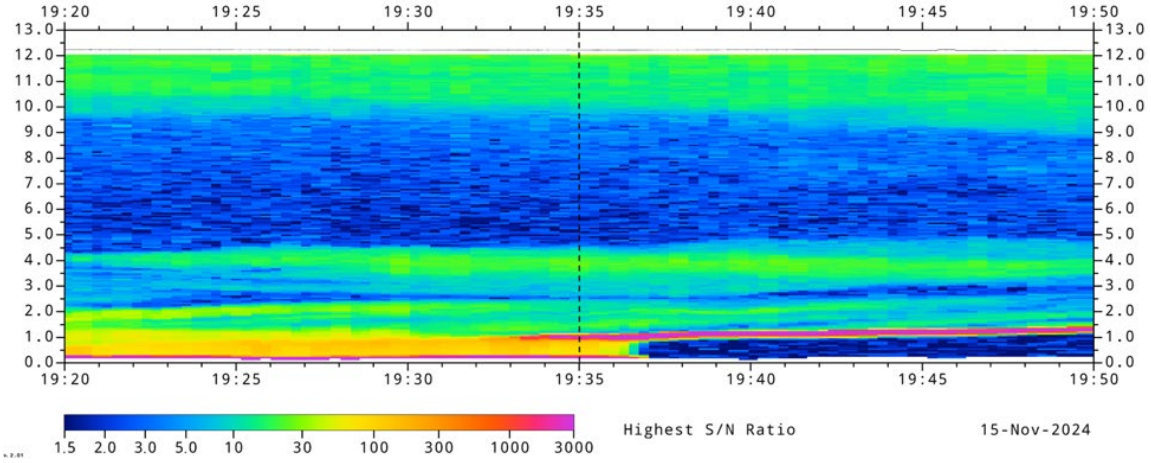

Figure 3.3: AWP signal to noise ratio curtain from 1920-1950 UTC on 15 November 2024, derived from integrating 3000 AWP pulses. The dashed line at 1935 UTC indicates the time period of AWP signals shown in Figures 3.2 and 3.4.

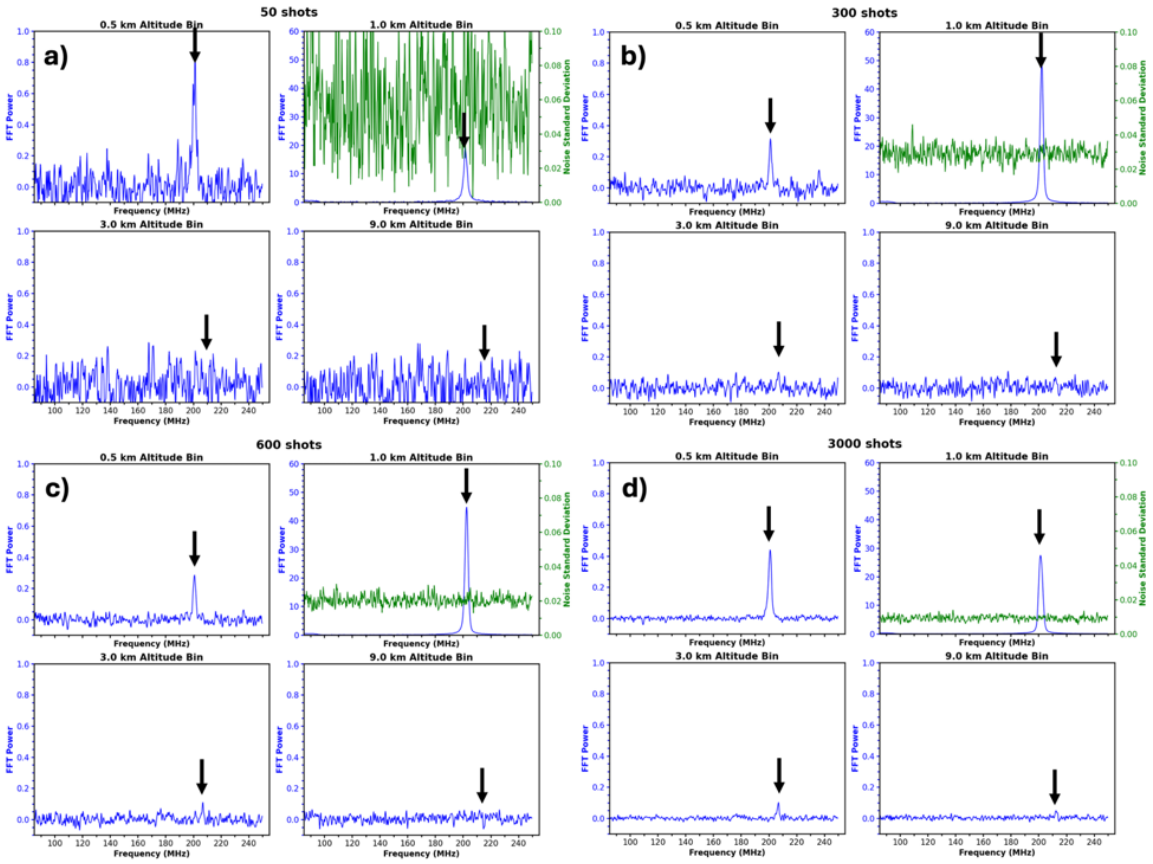

Figure 3.4: Examples of FFT periodogram spectra for 4 altitude bins, 0.5 (upper-left), 1.0 (upper-right), 3.0 (lower-left), and 9.0 km (lower-right) with increasing numbers of lidar pulses (or shots) used in the integration, a) 50 shots, b) 300 shots, c) 600 shots, and 1500 shots). Data are taken from one profile at 1935 UTC on 15 November 2024, identified in Figure 3.3 above. The signal noise floor is plotted in the upper right panel in green, while the detected signal is shown in blue. The frequency position of peaks evident with 3000 pulse integration are shown with black arrows. Note that the y-axis in the upper-right of panels a-d is 60 times greater than the other 3 panels due to the presence of a thick stratus cloud at 1 km altitude, seen in the SNR curtain of Figure 3.3.

4. Project History and Description of Airborne Activities

NASA LaRC initially received funding for this project in December 2022. The project kickoff meeting with NOAA was in February 2023. The LaRC proposal responding to the BAA announcement described flying AWP for two periods based on aircraft availability at the time of the proposal submission in July 2022. The first was to occur in May 2023, and the second was to occur in Feb-April 2024, both on the NASA LaRC Gulfstream-3 aircraft. In March 2023, NASA reprioritized the Gulfstream-3 for other NASA missions, a land surface vegetation mapping mission in Gabon in May 2023, and the Asia-AQ mission in winter-spring 2024. To collect an initial AWP dataset for delivery to NOAA, NASA funded rapid design, analysis, and fabrication of components that would allow AWP to integrate onto the NASA DC-8, to piggyback on the NASA ecoDemonstrator mission that occurred in October-November 2023. AWP had never flown on the DC-8 prior to this. NASA funding was provided to NASA LaRC in May 2023, and all components required for integration were successfully designed, fabricated and shipped to NASA Armstrong in Palmdale, CA in August 2023. AWP was successfully integrated onto the DC-8 in late September 2023. AWP collected data for ~51 hours across all DC-8 flights from 4 October – 1 November during ecoDemonstrator.

The focus of the ecoDemonstrator mission was generating and analyzing data to assess sustainable aviation fuel's capacity to benefit the environment (NASA, 2023). To achieve the mission objectives, the DC-8 rapidly transitioned from flying within contrails generated by a Boeing 737 aircraft flying directly in front of the DC-8, to flying in the environment outside the contrail. AWP measurements require a stable observation platform with very minimal heading and aircraft attitude (pitch and roll) changes throughout the 1.5-15 sec period that AWP is collecting data per LOS to derive a wind vector (time range is dependent on environmental conditions and science objectives). The DC-8 pilots were flying in and out of the contrails via manual control, which caused the aircraft heading/attitude to be quite unstable. This resulted in very poor quality AWP measurements, often featuring 1+ m/s velocity variation between profiles which appear as "stripes" in the wind vector profiles (see Section 5.1, Figure 5.1.1 for example). This required that the AWP data be aggressively spatially smoothed to mitigate the striping issue. In addition, due to the persistent flight within contrails and cirrus clouds, the AWP laser light was often being attenuated upon exiting the aircraft. This is not representative of what would be occurring during most airborne missions, and from space. Despite these significant issues, AWP demonstrated that backscatter signal from thin to moderately opaque clouds could be still be detected by a poorly-performing DWL over a broad depth (4+ km, Section 5.1) in which winds can vary substantially from the base to the top of the cloud return. We expect that a space-based implementation of the NASA DWL would have detected all cloud signal detected by AWP during ecoDemonstrator and much more signal from aerosol in clear sky conditions. 51 hours of data from ecoDemonstrator was delivered to the NOAA DEEVA team in April 2024 for their initial analysis and assimilation experiments.

Analysis of the AWP and High Altitude Lidar Observatory (HALO, developed by a team led by Amin Nehrir (NASA LaRC)) data from EcoDemonstrator indicated that instrument sensitivity to aerosol backscatter was below expected performance, even when some attenuation due to flight through cirrus was factored into the analysis. Further investigation revealed that the AWP beam expanding telescopes were poorly aligned by the industry vendor who assembled them. Using a Zygo interferometer, NASA LaRC estimated telescope alignment with ~1/3rd of a wave RMS wavefront error. The primary issues were astigmatism and beam divergence which resulted in up to 95% signal loss relative to a telescope with excellent alignment (≥ 1/20th of a wave RMS wavefront error). Such a significant signal loss reduces sensitivity to aerosol and greatly reduces the vertical coverage of successful wind retrievals, making the data we collected during EcoDemonstrator unrepresentative of how an AWP-like system would perform in space. Both AWP telescopes were rebuilt from January-July 2024, and measurements using the Zygo interferometer from the rebuilt telescopes indicated better than ~1/20th of a wave RMS wavefront error at a 2 µm wavelength, the baselined specification for a space-based wind lidar telescope.

AWP was integrated onto the LaRC Gulfstream-3 from 5-17 September 2024. AWP was positioned on the forward port on the G-3, which was a new installation compared to January 2023 AWP Engineering Test Flights where AWP was positioned on the aft port. The HALO instrument was positioned on the aft port during the Fall 2024 AWP flights. A photo of the AWP instrument, and a photo of AWP and HALO integration aboard the G-3 is provided by Figure 4.1. HALO features a four-wavelength differential absorption lidar (DIAL) transmitting near 935 nm for water

vapor (Caroll et al. 2022), and a 1064 nm backscatter and 532 nm high-spectral-resolution lidar (HSRL, Hair et al. 2008) for aerosol and cloud profiling. AWP collected data for 99.6 hours during the NOAA 3-D Wind Demo and the WH^{2}yMSIE/APEX missions (Table 5.2.1). As will be described in the following section, some flights were executed at flight altitudes beneath 10 km, and were often focused on process studies which required repeating tracks over very limited geographic areas (Figure 5.2.1-right). Data from these flights were not delivered to the NOAA DEEVA team as they were not considered to be worthwhile for their analysis. Excluding these process study-oriented flights, nearly 74 hours of AWP data were delivered to NOAA in March 2025. AWP and HALO data were also delivered to the NASA LaRC WH^{2}yMSIE/APEX data archive and are available to the public at: https://www-air.larc.nasa.gov/cgi-bin/ArcView/whymsie?G3=1

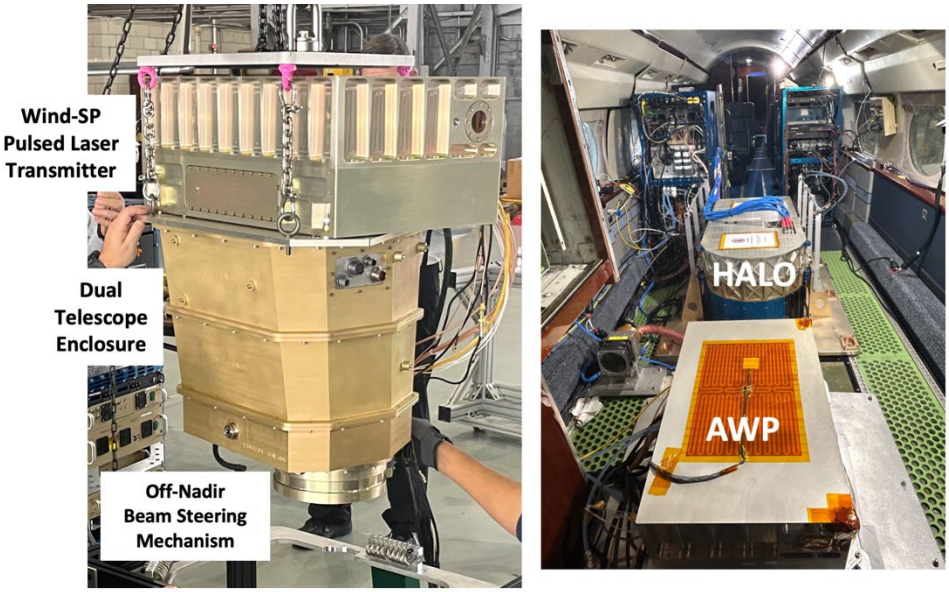

Figure 4.1: (left) A photo of the AWP instrument prior to Gulfstream-3 integration. (right) A photo of AWP, HALO, and their equipment racks integrated for flight aboard the Gulfstream-3. Photos taken by Kristopher Bedka (NASA LaRC).

5. AWP Airborne Data and Validation

5.1 16 October 2023 ecoDemonstrator Flight Example

As noted in Section 4, near constant NASA DC-8 aircraft attitude changes coupled with poor AWP telescope alignment resulted in degraded quality AWP wind measurements. Figure 5.1.1 shows an AWP SNR and wind speed curtain, in addition to the corresponding HALO 532 nm aerosol backscatter curtain for an ecoDemonstrator flight on 16 October 2023. Variability in the pattern of the black aircraft altitude line atop the data curtain indicates high-frequency altitude variations that were coupled with roll and pitch variations. AWP and HALO detections of clouds between flight level and 8 km altitude agree quite well. Signal return from clouds is detected over a 4 km deep layer for some clouds, where wind speed increased by over 15 m/s from the base of the cloud return to the cloud top. An aerosol layer detected by HALO from the land surface to ~2 km altitude (cyan shading) is completely absent from the AWP curtain, despite AWP being able to detect the land surface as evidenced by enhanced AWP SNR along the ground. As will be shown for the 13 and 15 November 2024 WH^{2}yMSIE/APEX flights in Section 5.2, it was extremely rare for AWP to miss aerosol layers detected by HALO. AWP retrievals were limited to times where the DC-8 was flying straight and level, which often required that over half the lidar pulses per LOS when the aircraft was changing attitude erratically be excluded from the retrieval. This coupled with the poor telescope alignment greatly reduced backscatter sensitivity. In addition, a close examination of the AWP wind speed curtain shows notable discontinuities, or “stripes” from profile to profile, caused by DC-8 attitude changes that could not be mitigated even

with exclusion of a large fraction of AWP pulses where the aircraft had especially large attitude variations. The striping was overcome to some extent by aggressive spatial smoothing, but the poor backscatter sensitivity could not be overcome. Nevertheless, delivery of this data to the NOAA DEEVA team enabled initial data assimilation experiments which paved the way for work with the Fall 2024 AWP data. We will focus on description of the Fall 2024 flight data for the remainder of this report.

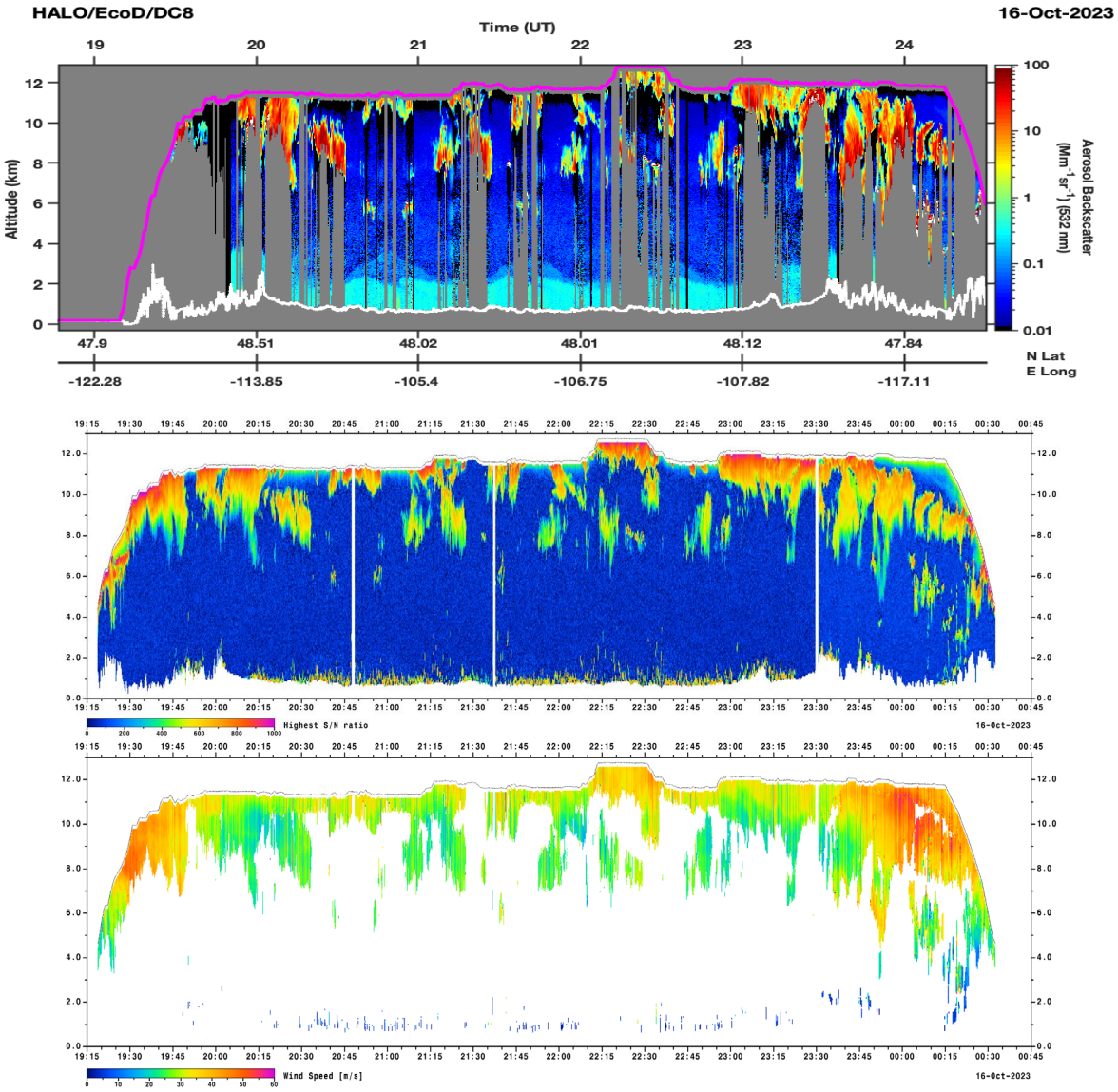

Figure 5.1.1: (top) HALO 532 nm aerosol backscatter curtain for an ecoDemonstrator DC-8 flight on 16 October 2023. AWP SNR (middle) and wind speed (bottom) curtains over the same timeframe as the HALO data.

5.2 Fall 2024 Airborne Data Collection Overview

A list of flights from the NOAA 3-D Wind Demo and WH^{2}yMSIE/APEX campaigns is shown in Table 5.2.1. Maps of G-3 flight tracks across the two campaigns are shown in Figure 5.2.1. Those most relevant to this NOAA project are highlighted in blue in Table 5.2.1, which had flight altitudes exceeding 10 km, and many long, straight flight segments that emulate an orbital satellite observation track. Other flights listed in black text were mostly at lower altitude (7-9 km) and/or were focused on process studies, emphasizing PBL and cloud measurements, several of which were in coordination with the Naval Research Laboratory Twin Otter aircraft. An exception to this was 14 November where

the G-3 was sampling over a very limited area with 8.5-10 km flight altitude. Two sondes were dropped on this day, so data was delivered for NOAA to allow further evaluation of AWP data quality.

NOAA 3-D Wind Demo flight days were chosen based on weather conditions within the ~6-hour maximum endurance of the G-3, as well as aircraft and instrument operator availability. There were no flight operations on weekends or holidays. We sought to sample a variety of weather conditions, including high and low wind speeds, jet streams, cyclones (low pressure regions) and anti-cyclones (high pressure), oceanic and continental atmospheres, and varying cloud cover patterns. Our flight plans were based solely on the synoptic-scale weather conditions depicted by a variety of operational numerical weather prediction model forecasts displayed on various web pages. We had no expectation of what the aerosol conditions would be on a given flight day. We did not base our flight planning on any particular model data source that predicted aerosol typing or concentration (i.e. "optical depth") profiles (e.g. the NASA GMAO GEOS-5 model, see Figure 5.2.1.5 for example). Thus, the collected data were not biased in any way toward more aerosol-rich environments that could yield more favorable AWP wind profile data and skew perception of AWP performance.

WH^{2}yMSIE/APEX flight days were based on a variety of factors including ER-2 aircraft availability and weather conditions at Edwards Air Force Base, availability of the G-3 and Twin Otter, and/or regional weather conditions within reach of the G-3 and ER-2. Days with ER-2 underflights were mostly absent of high cloud cover to allow IR and microwave sounders aboard the ER-2 to collect the best possible data, as well as to avoid clouds at the G-3 flight altitude that would attenuate the AWP+HALO lidar beams. When clouds were encountered at flight level, the G-3 pilots were directed to fly slightly beneath cloud base, which typically required an altitude adjustment of up to 3000 feet.

Flight Date	Sampling Objective	Number of AVAPS Dropsondes Released	AWP Dwell Time Per LOS (seconds)	Duration of AWP Operation (hours)
20240918	Instrument Engineering Check Flight	1	2-3	2.8
20240920	**Airmass transitions across the Southeast U.S. and Atlantic Ocean**	**4**	**6**	**5.0**
20240924	**Upper tropospheric trough over Nebraska that served as a steering mechanism for Hurricane Helene, and a severe thunderstorm environment over Kentucky and western Virginia**		**6**	**5.0**
20240926	**Hurricane Helene environment and steering flow. Two flights, with a refuel in Stennis, Mississippi**	**3**	**6**	**7.6**
20241001	**Transition from a mid-latitude to subtropical airmass over the Atlantic**	**6**	**6**	**4.2**
20241003	**Wildfire smoke plume over New York and Ontario, polar jet stream over Quebec**	**5**	**6**	**3.8**
20241008	**Airmasses over the southeastern Virginia and Northeast U.S. metropolitan areas, overflight of the NOAA Wind Forecast Improvement Project – 3 (WFIP-3) domain**	**5**	**1.5-6**	**5.0**
20241015	**Jet stream and upper-tropospheric trough over the Northeast U.S.**	**6**	**6**	**4.9**
20241016	**High pressure system in the Midwest and Southeast U.S.**		**6**	**4.9**
20241027	**Transit flight from Hampton, VA to Santa Maria, CA**		**6**	**5.3**
20241030	**Cloud type transitions over the Pacific west of Baja California, with ER-2 aircraft and ESA EarthCare satellite underflights**	**10**	**6**	**4.1**
20241031	Monitoring PBL evolution over Arizona, with a refuel in Phoenix. Flight segments devoted to ER-2 underflight		1.5-6	6.1

20241104	**Oceanic airmass monitoring, overflight of San Francisco, the Sierra Nevada, and the Nevada Railroad Valley region, with ER-2 aircraft and ESA Arctic Weather Satellite underflights**	**10**	**6**	**4.6**
20241107	**Oceanic airmass monitoring, Ventura County, CA Mountain Fire smoke plume sampling, with ER-2 underflight**	**14**	**1-6**	**5.2**
20241108	Central CA coast wind, water vapor, and aerosol evolution within the PBL, coordination with the Navy Twin Otter		1-4	5.1
20241109	Central CA coast wind, water vapor, cloud, and aerosol evolution within the PBL, coordination with the Navy Twin Otter		0.75-4	5.5
20241112	Central CA coast wind, water vapor, cloud, and aerosol evolution within the PBL		1-4	5.4
20241113	**Pre- and post-frontal airmass monitoring over the Pacific west of California, with ER-2 and ESA EarthCare underflight**	**7**	**3-15**	**5.6**
20241114	**Central CA coast wind, water vapor, cloud, and aerosol evolution within the PBL, coordination with the Navy Twin Otter**	**2**	**0.75-4**	**5.4**
20241115	**Transit flight from Moffet Field, CA to Hampton, VA**		**15**	**4.1**

Table 5.2.1: A list of G-3 flight dates, AWP observation periods, flight sampling objectives, dropsonde counts, and AWP dwell time per LOS. Flight dates delivered to NOAA that were most relevant for AWP evaluation are highlighted in blue.

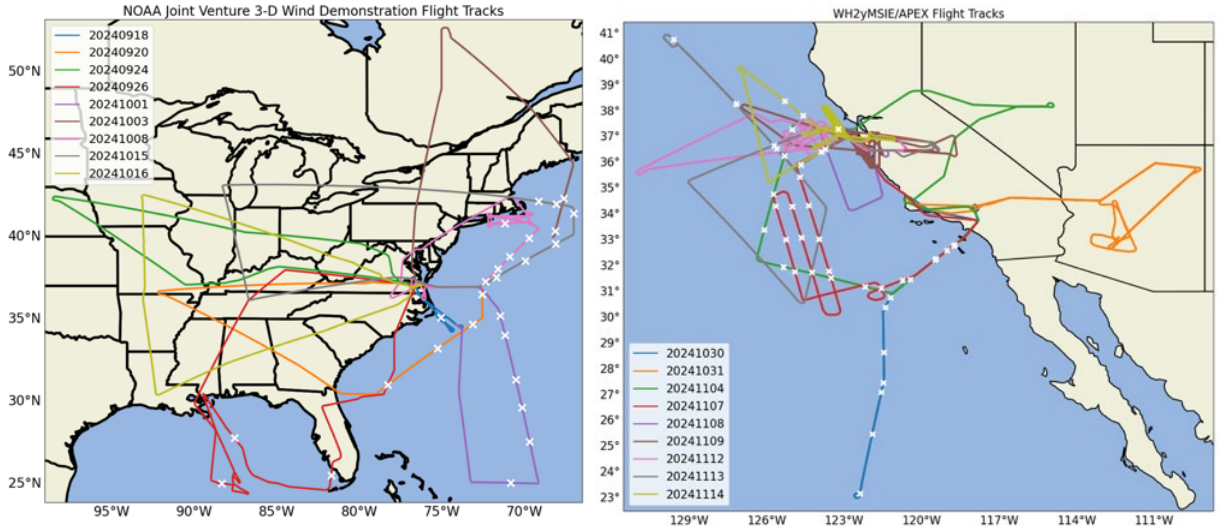

Figure 5.2.1: NASA Gulfstream-III flight tracks for the NOAA 3-D Wind Demo (left), and the WH²yMSIE/APEX (right) campaigns. Dropsonde locations are shown with white X symbols. Cross-country transit flights to/from WH²yMSIE/APEX are omitted from the right panel.

5.2.1. 15 October 2024 Flight

We highlight data from several of the flights listed above to demonstrate AWP performance in a variety of wind, cloud, and aerosol regimes. The first flight we feature was on 15 October 2024, and focused on sampling an upper-tropospheric trough positioned over the northeast U.S. and southern Canada (Figure 5.2.1.1). This day featured one of the first infiltrations of cool Canadian air during Fall 2024, which triggered the formation of widespread cumulus cloud cover and lake effect rain bands over Lake Huron and Michigan due to the presence of cold air over the still moderately warm land and lake surfaces. The flight began by heading east from Hampton, VA and northeast up to

the coast of Massachusetts, along a southwesterly oriented jet stream depicted evident in the 250 hPa GFS wind forecast (Figure 5.2.1.1). Six dropsondes were released over the Atlantic Ocean. The flight progressed westward through a trough axis and near to Milwaukee, WI. Jet stream wind flow depicted by the GFS was quite weak in the trough, and wind flow was from the north in the lower troposphere (Figure 5.2.1.1). The flight then headed southeast-ward through the base of the trough down to the Nashville, TN area. The flight then headed eastward toward Hampton, VA within the same jet stream sampled over the Atlantic at the beginning of the flight. AWP collected vector wind profiles every 7 seconds during the flight, equating to ~1.5-2.0 km spacing between profiles (depending on aircraft airspeed). HALO did not operate during this flight.

The AWP SNR curtain shows very complex aerosol layering throughout the flight (Figure 5.2.1.2). The two westerly and south-westerly segments (warm color shading in wind direction curtain) of the jet stream regions are clearly evident in the AWP data, with speeds exceeding ~50 m/s extending down to 6 km altitude. While the aircraft was sampling the jet streams, aerosol backscatter was comparatively weaker than the lower wind speed region within the trough. Wind direction within the trough ranged from northerly to easterly (cool color shading), in agreement with the GFS model forecast. The 12 UTC National Weather Service sounding from Detroit, Michigan showed that the tropopause was near 8 km (not shown). There is a clear gradient in AWP SNR around 8 km, with notably higher SNR (30-50 times the instrument noise level, green/yellow shading) above 8 km within the stratosphere, indicating significant aerosol loading. Analysis of NOAA HYSPLIT model back-trajectories, initialized at a 10 km altitude from Detroit near the time of the G-3 overpass, indicated that this airmass was transported from the southeastern Alaska region 120 hours prior and into the northeast U.S (not shown). Horizontally-oriented, wave-like wind velocity structures are evident in the AWP wind speed data, but not in the aerosols depicted by the SNR curtain (Figure 5.2.1.3). The physical process to explain the presence of these waves is unclear. But the fact that we see them in AWP data shows the value of high resolution and precise wind data for revealing complex and detailed atmospheric dynamics processes.

HYSPLIT suggests that aerosol at 5 km altitude originated from British Columbia and the north Pacific up to 168 hours prior to the AWP observation, with many trajectories descending to altitudes beneath 4 km (Figure 5.2.1.4-left). The NASA Fire Information for Resource Management System (FIRMS), which compiles fire detections from the NASA MODIS, VIIRS, and Landsat Imagers, showed many wildfires on 10 October along the trajectories (Figure 5.2.1.4-right). This suggests that aerosol in the mid-troposphere may have been from long-range transport of aged wildfire smoke. Fires are quite frequent in the western U.S., Canada, and Siberia during the warm season, and in Central America during winter/spring, and their smoke would be a significant contributor of signal for a Doppler wind lidar to retrieve winds. The presence of enhanced aerosol loading observed by AWP over the long east to west flight segment from offshore of Massachusetts and across the Great Lakes region was not well captured by the NASA GEOS-5 total aerosol thickness product (Figure 5.2.1.5), which depicted very low optical thickness along this segment.

As noted above, cloud cover was abundant during this flight, especially cumulus in the lower atmosphere seen in the GOES image (Figure 5.2.1.2-upper right). Mid-level cloud cover attenuated the lidar beams in a couple instances during the first third of the flight, and late in the flight during the segment from Nashville to Virginia. SNR in these opaque clouds was 300-3000 times greater than the noise level. AWP's fine spacing between vector wind profiles was able to penetrate through holes in the cumulus in many instances. Where there was clear sky throughout the atmospheric column at 1720 UTC, AWP vector winds agreed extremely well with the corresponding AVAPS dropsonde profile (Figure 5.2.1.2-lower right).

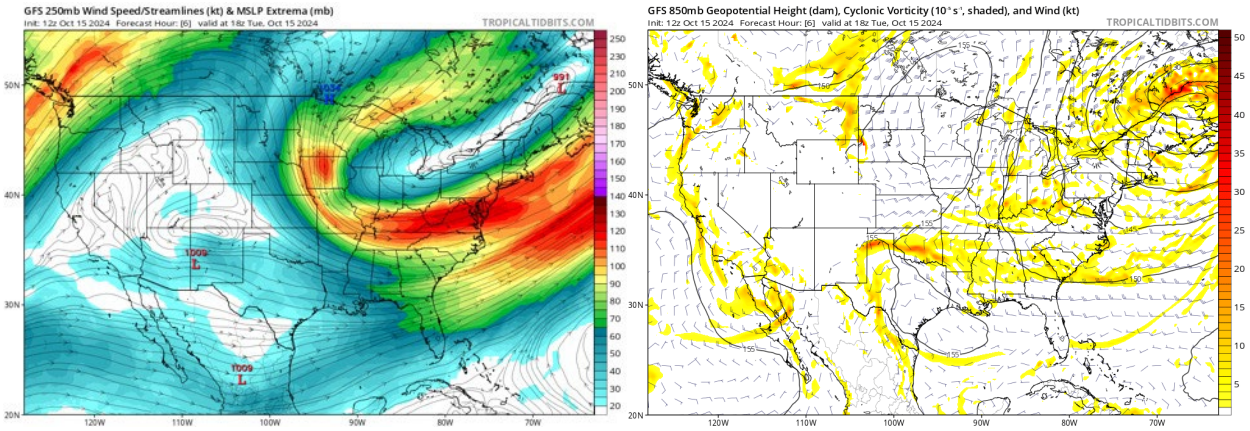

Figure 5.2.1.1: (left) NOAA GFS model six-hour forecasts of the 250 hPa wind speed and streamlines from the 12 UTC run on 15 October 2024. (right) 850 hPa wind barbs, geopotential height, and cyclonic vorticity. Graphics were acquired from the Tropical Tidbits website and used here with permission from the website developer (see "Terms of Use" at the bottom of https://www.tropicaltidbits.com/analysis/models/).

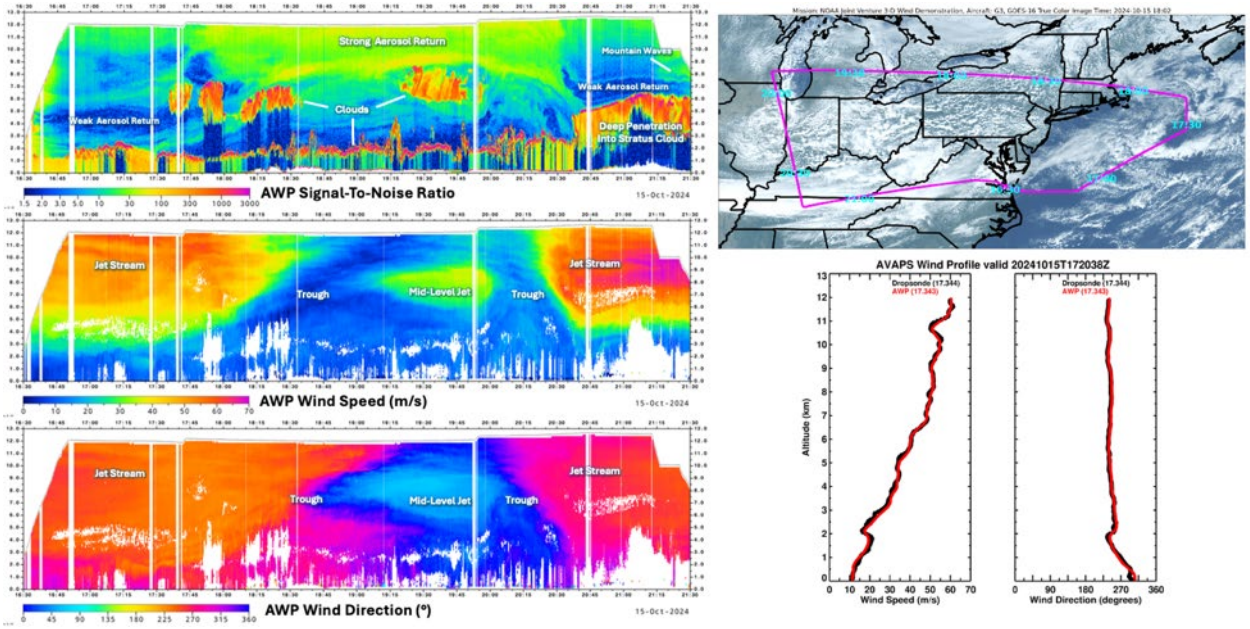

Figure 5.2.1.2: (left) AWP signal to noise ratio (SNR), wind speed and wind direction profiles on 15 October 2024 over the flight track shown in the upper-right panel. (lower-right) A comparison of the spatially-averaged AWP data profile and AVAPS dropsonde at 1720 UTC. The AWP spatial averaging/smoothing process is described in Section 3. White columns in the AWP data curtains indicate aircraft turns where AWP wind vector retrievals are not possible.

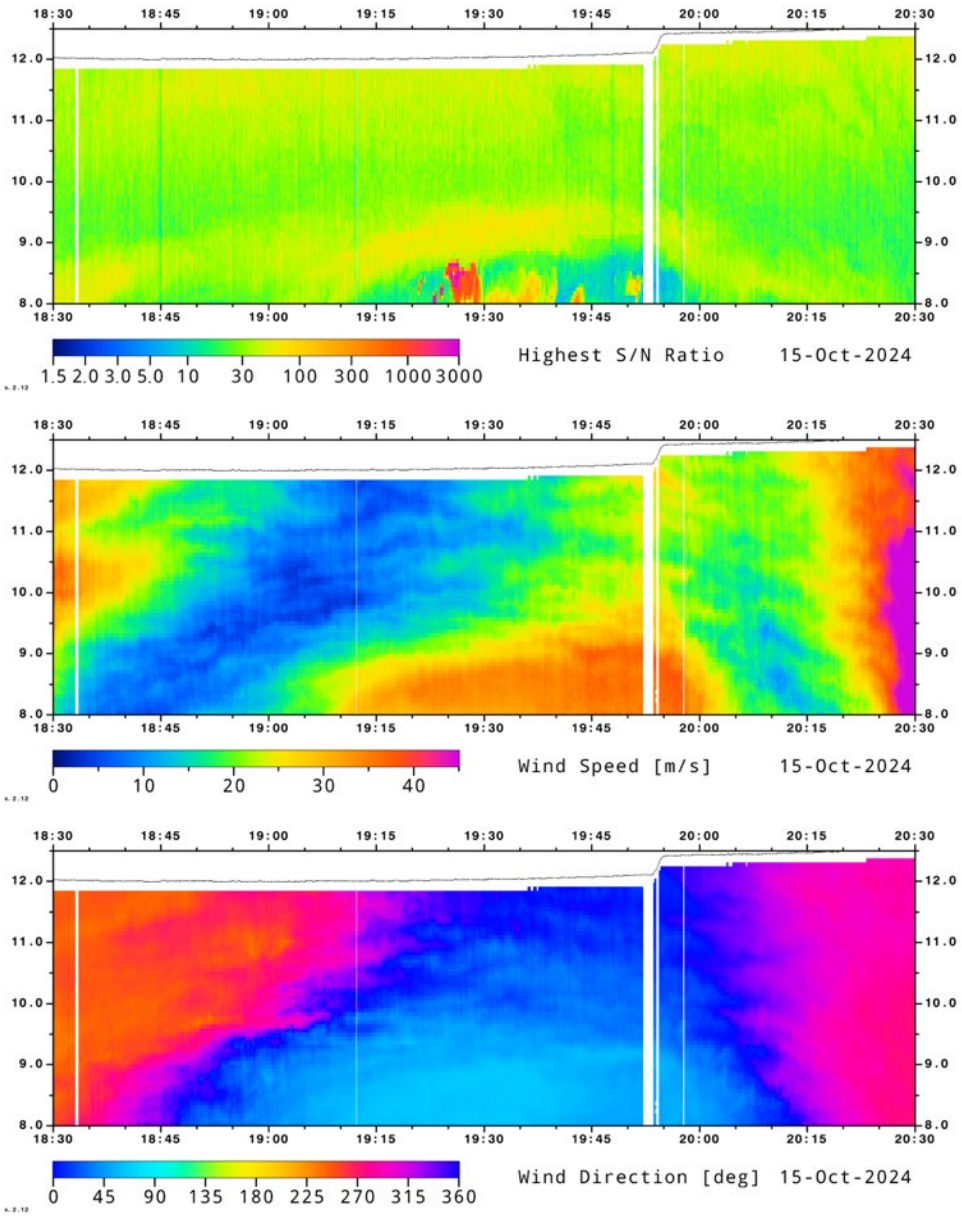

Figure 5.2.1.3: AWP SNR, wind speed, and wind direction curtains above an 8 km altitude, focused on the flight segment within the mid-latitude cyclone trough axis and stratosphere discussed in the text. The wind speed color bar range is compressed relative to Figure 5.2.1.2 to emphasize horizontally oriented wave features.

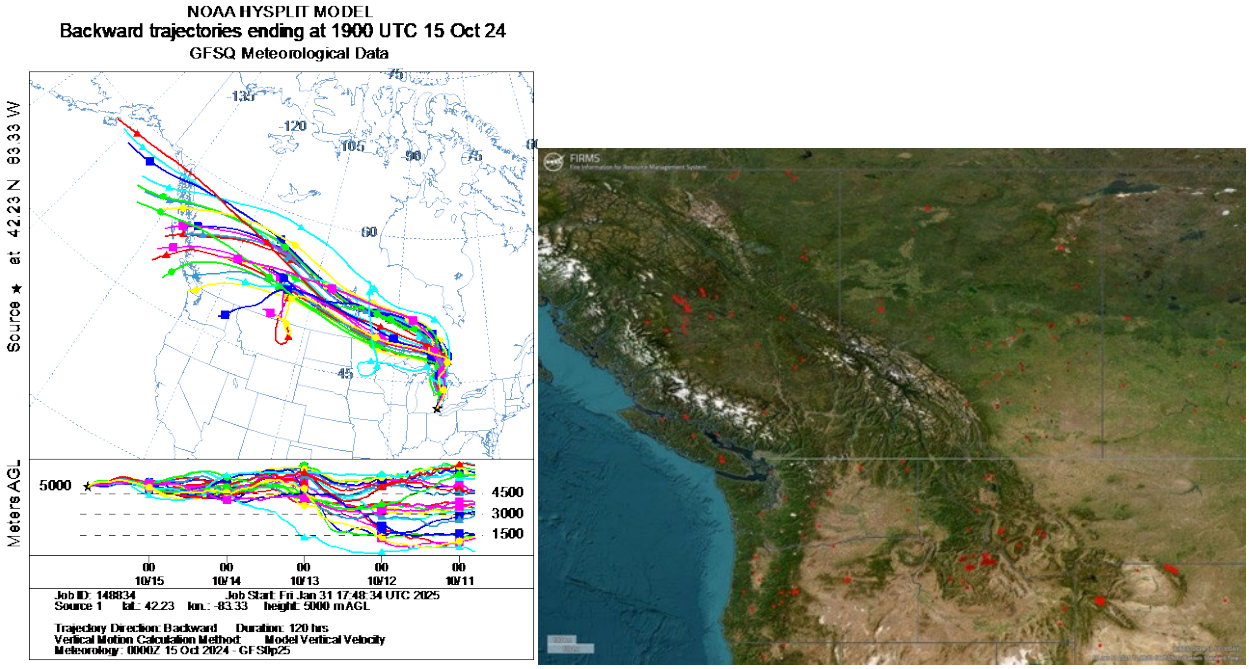

Figure 5.2.1.4: An ensemble of NOAA HYSPLIT back-trajectories initialized from Detroit, MI at a 5 km altitude, where AWP saw aerosol layers during flight, at 19 UTC on 15 October 2024. Back-trajectories were run to a period 120 hours prior to the initialization time. 0.25° GFS model output was used as the meteorology for this run. (right) Depictions of wildfire locations detected by MODIS, VIIRS (red), and Landsat (maroon) on 10 October displayed within the NASA FIRMS tool, showing that the trajectories overpassed many fires that could be responsible for the aerosol detected by AWP.

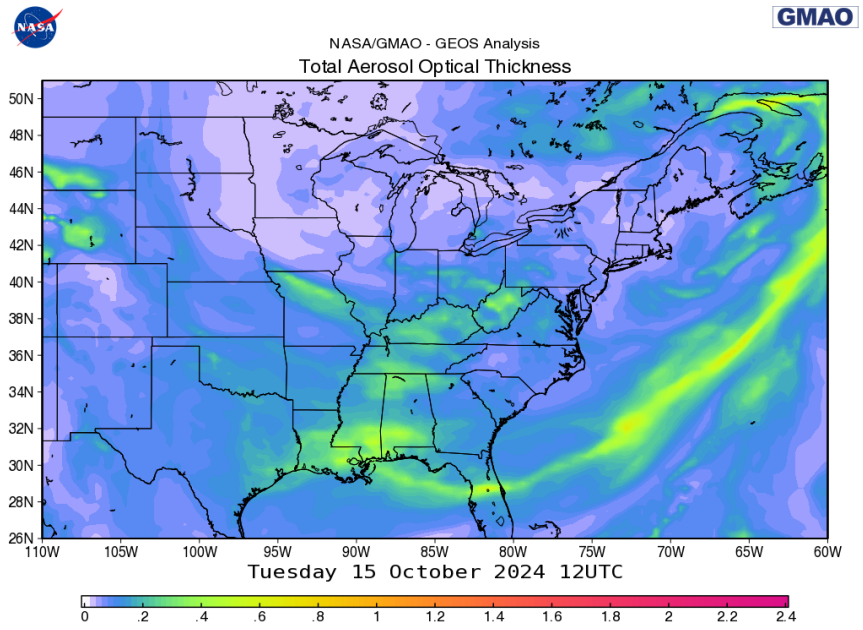

Figure 5.2.1.5: NASA GMAO GEOS-5 model forecast of total column aerosol optical thickness, valid at 12 UTC on 15 October 2024.

5.2.2. 13 November 2024 Flight

A flight on 13 November intended to collect observations to the north and south of a cold front over the Pacific, where differing airmasses and wind conditions were present. A cold front was just offshore of the San Francisco Bay region and northern California, where winds at surface shifted from a southerly direction on the south and east side of the front to west-northwesterly to the northwest of the front. A 250 hPa jet stream overlaid the front with winds exceeding 135 kts (70 m/s) according to the GFS model (Figure 5.2.2.1). AWP collected vector wind profiles every 7 seconds from 1855-2243 UTC (~1.6 km spacing), and then every 16 seconds during the rest of the flight (~ 4 km spacing). The G-3 aligned with the ER-2 to collect coordinated measurements for several hours during the flight in support of the WH^{2}yMSIE/APEX campaign. The flight departed from Moffet Field, CA and headed eastward over the Central Valley of California at an ~8.5 km flight altitude (Figure 5.2.2.2-upper right). AWP data curtains show an aerosol-rich airmass over the Central California region (Figure 5.2.2.2-left). Complex wind direction patterns were evident below 2 km altitude in this area. The flight then headed westward and overpassed multi-layered cloud conditions along the decaying cold front. AWP was able to penetrate through the upper-cloud layer into aerosols and clouds below. The flight headed northwest into a cooler, post-frontal airmass. Signal return was quite strong beneath a 3 km altitude, which could have been due in part to strong winds up to 20 m/s in this layer that enhanced sea spray. From 3-6 km, aerosol layers sloped upward until the aircraft made a turn back to the southeast along the same track. Cumulus clouds became more abundant and deeper in the northwest end of the flight track. In the upper portion of the curtain, a shallow layer of winds exceeding 65 m/s sloped downward to about an 8 km altitude. Investigation of GFS model data revealed that this shallow high wind layer resided around the tropopause level, thus the aircraft was well into the stratosphere from ~2015-2145 UTC. Higher aerosol backscatter was present in the stratosphere than in the upper troposphere, similar to the 15 October flight discussed above. A dropsonde released at 2029 UTC showed excellent agreement with AWP (Figure 5.2.2.2-lower right). The aerosol and wind patterns closely mirrored each other from 2000-2200 UTC because the aircraft flew on the same track.

After crossing the cold frontal cloud band, aerosol backscatter reduced, indicative of a change in airmass and aerosol transport pathways. The aircraft headed southwest along an ESA EarthCare satellite track coinciding with an opaque stratocumulus deck, and then turned back to the northwest. The stratocumulus deck altitude and depth of the higher backscatter return in the PBL was notably lower than the post-frontal airmass, indicative of a change in thermodynamic conditions in the pre-frontal region. HYSPLIT back-trajectory analysis from a parcel initialized within a very thin aerosol plume at 3 km at 23 UTC suggests that this airmass resided over the open Pacific Ocean 5 days prior (Figure 5.2.2.3-left), and near Japan 10 days prior. The very long-duration transport from Asia could be a source of the thin aerosol detected by AWP, but the 10 day transport and dispersion of the aerosol also explains the generally clean air in the pre-frontal airmass.

During the turn to the northwest at 2243 UTC, AWP changed operation mode to collect data with 15 sec intervals (3000 pulses) per LOS to explore how additional signal integration affects SNR and wind retrieval vertical coverage. The SNR curtain shows an increase in SNR after the increase in integration duration. This is to be expected because increasing integration (averaging) of FFT spectra reduces the amplitude of random noise signals while preserving the frequency and amplitude of the true signal peak from aerosol backscatter and the wind, as was discussed in Section 3. A thick layer of aerosol appeared to the north of the cold front that was notably different than that seen earlier in the flight to the east in comparable proximity to the north edge of the frontal cloud band. HYSPLIT analysis from parcels initialized within the thick aerosol plume at 6 km at 2330 UTC suggests that this airmass was rapidly transported across the Pacific from the northeastern China and Japan region 5 days prior (Figure 5.2.2.3-right). This further reinforces how long-range aerosol transport can provide strong backscatter return for wind lidar retrieval. The strong jet stream measured earlier in the flight re-emerged shortly before final descent and landing. Thoughout the flight, AWP SNR patterns show excellent agreement with HALO 532 nm aerosol backscatter (Figure 5.2.2.4), and reveal the presence of aerosol layers that are near to or beyond the backscatter threshold used for HALO aerosol detection.

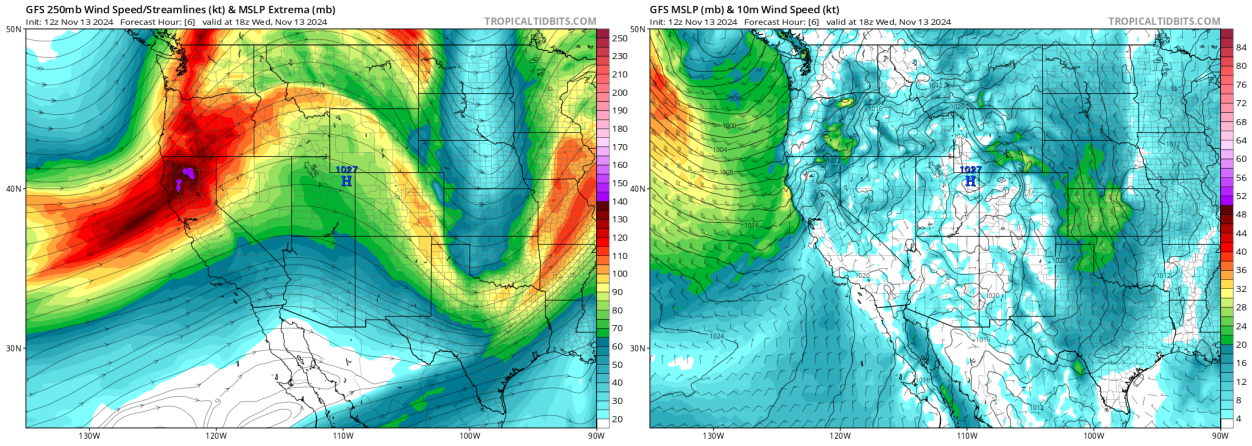

Figure 5.2.2.1: (left) NOAA GFS model six-hour forecasts of the 250 hPa wind speed and streamlines from the 12 UTC run on 24 September 2024. (right) 850 hPa wind barbs, geopotential height, and cyclonic vorticity. Graphics were acquired from the Tropical Tidbits website.

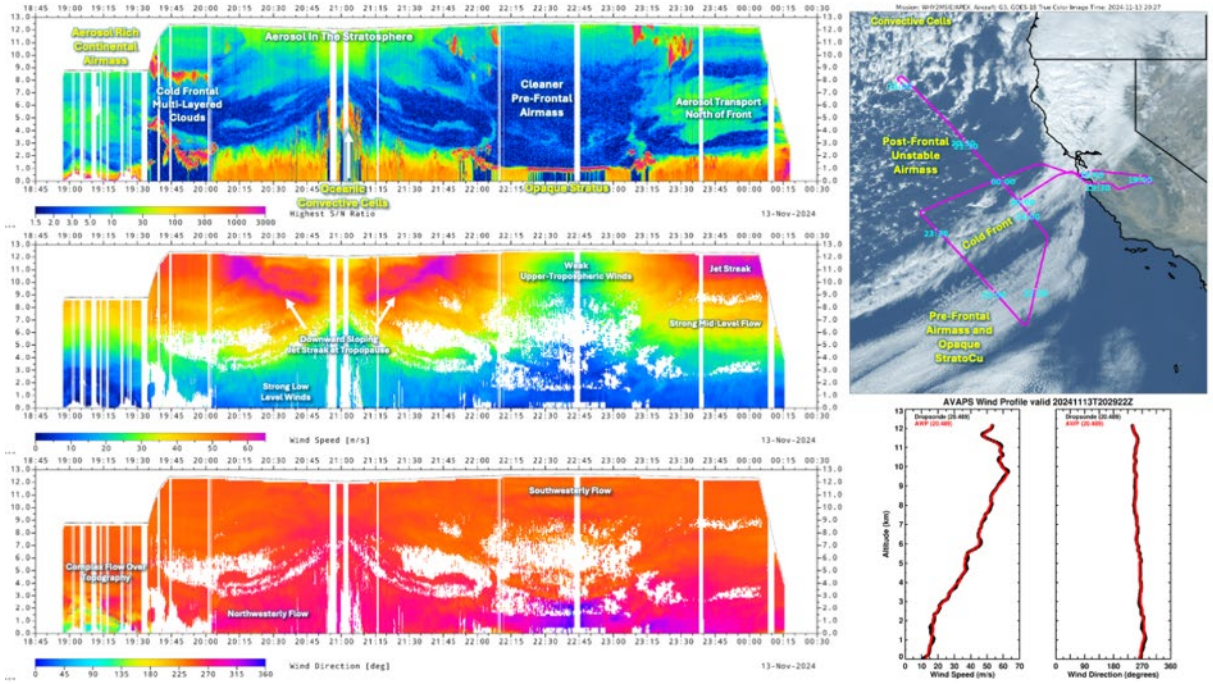

Figure 5.2.2.2: (left) AWP signal to noise ratio (SNR), wind speed and wind direction profiles on 13 November 2024 over the flight track shown in the upper-right panel. (lower-right) A comparison of the spatially-averaged AWP data profile and AVAPS dropsonde at 2029 UTC. The AWP spatial averaging/smoothing process is described in Section 3. White columns in the AWP data curtains indicate aircraft turns where AWP wind vector retrievals are not possible.

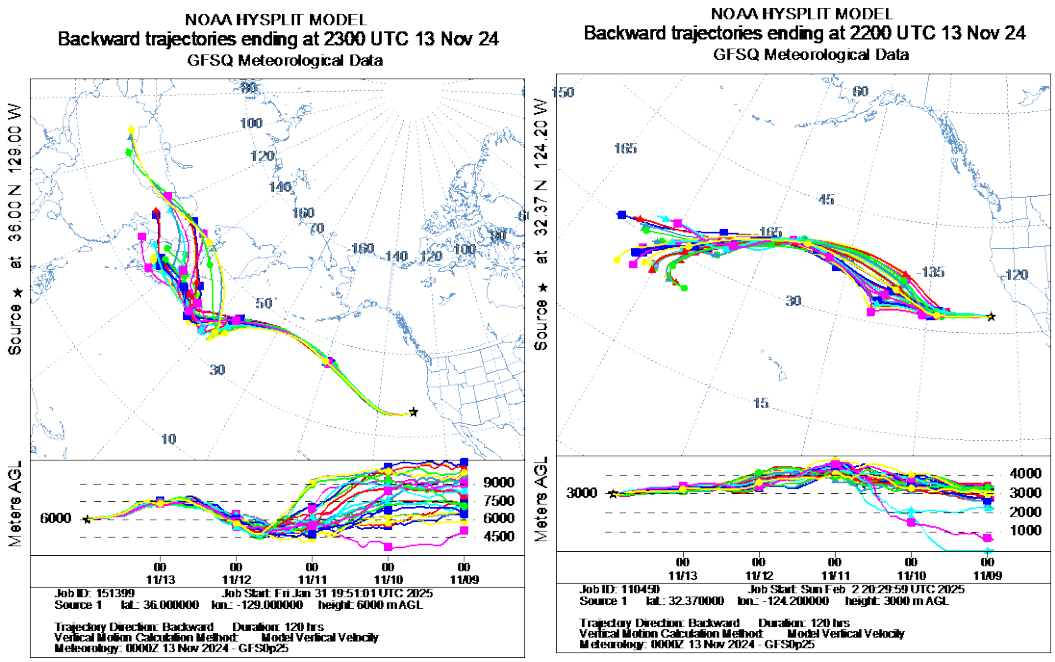

Figure 5.2.2.3: (left) An ensemble of NOAA HYSPLIT back-trajectories initialized from the time and location of a thick aerosol plume at 6 km altitude and 23 UTC on 13 November 2024. (right), HYSPLIT trajectories initialized from a thin aerosol layer in the pre-frontal airmass at 3 km altitude and 22 UTC. Back-trajectories were run to a period 120 hours prior to the initialization time. 0.25° GFS model output was used as the meteorology for this run.

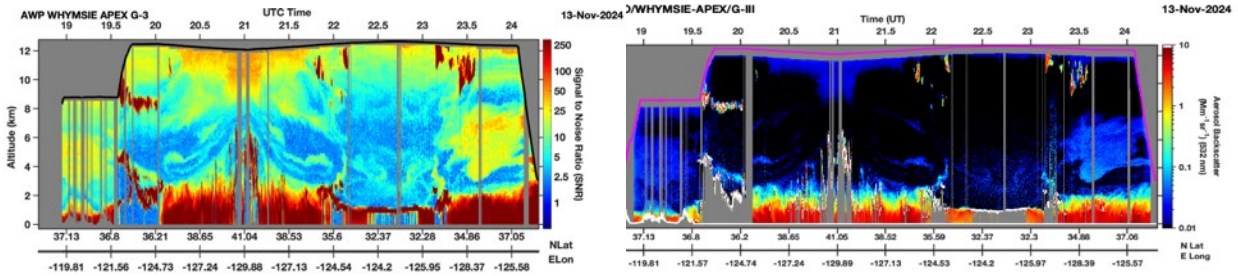

Figure 5.2.2.4: (left) AWP SNR and (right) HALO 532 nm aerosol backscatter for the 13 November 2024 flight. Data prior to 22.75 (2245, vertical grey bar) UTC is based on 1200 AWP pulse integration. 3000 AWP pulses are integrated after 22.75 UTC.

5.2.3. 24 September 2024 Flight

The purpose of this flight was to sample a lower-troposphere low pressure system centered over Illinois (Figure 5.2.3.1-right), and a jet streak and upper-tropospheric trough that extended into Nebraska (Figure 5.2.3.1-left). The upper-tropospheric trough was forecast to deepen and become a cutoff low over Louisiana the following day. This low and the southerly flow on its east side served as the primary steering mechanism to direct Hurricane Helene to landfall on the Florida Gulf Coast. The low and the tropical airmass from the hurricane combined to generate flooding rainfall over the southern Appalachians in the following days. AWP observed with its nominal 1.6 km spacing between profiles.

The G-3 took off shortly before 1520 UTC. There was abundant cloud cover along flight track during the first half of the flight. AWP sampled cirrus outflow from deep convection over Appalachia from 1540 to 1610 UTC. The lidar pulses penetrated up 3 km deep within the cloud. AWP was able to penetrate a more deeply into this cloud than HALO (Figure 5.2.3.2). AWP had excellent agreement with HALO in their depiction of aerosol and cloud layering

throughout the flight. Convection and cirrus clouds were intermittently sampled through 1730 UTC. Aerosol layers were present above cloud top, especially near 11 km where a thick aerosol layer was present (orange shading in SNR curtain) at tropopause level. In the lower-troposphere, southwesterly flow was found ahead of the surface low at 1640 UTC and northwesterly flow was found behind the low at ~1710 UTC, as was depicted by the GFS 850 hPa forecast (Figure 5.2.3.1-right).

As the aircraft crossed the upper-level trough axis, a period of calm winds was found from 7 km up to flight level from 1720-1735 UTC. Immediately after crossing the trough axis, the wind direction above 5 km altitude turned to northerly and winds accelerated to near 60 m/s. The aircraft then turned to the southeast to transect the trough axis and sample another jet streak over Kentucky. From 1825-1850 UTC, another layer of cirrus was sampled, where AWP detected cloud through a 5.5 km layer before the laser light became fully attenuated. The layer of thick aerosol was present again above cirrus cloud top at the tropopause. Over Kentucky, the NOAA Storm Prediction Center had issued a Slight Risk for severe thunderstorms. This was associated with a jet streak overlying an unstable airmass with some vertical wind shear. AWP detected the jet streak beginning at 1900 UTC which continued to persist until final aircraft descent near 1955 UTC. Wave patterns and complex aerosol layering were evident in this severe storm airmass from 1855-1930 UTC. The aircraft had to fly northeastward over Kentucky to avoid a line of strong storms that reached flight level. The vertical wind shear in the lower-troposphere was most evident in the wind speed curtain, where winds increased to over 30 m/s at 4 km at 1925 UTC.

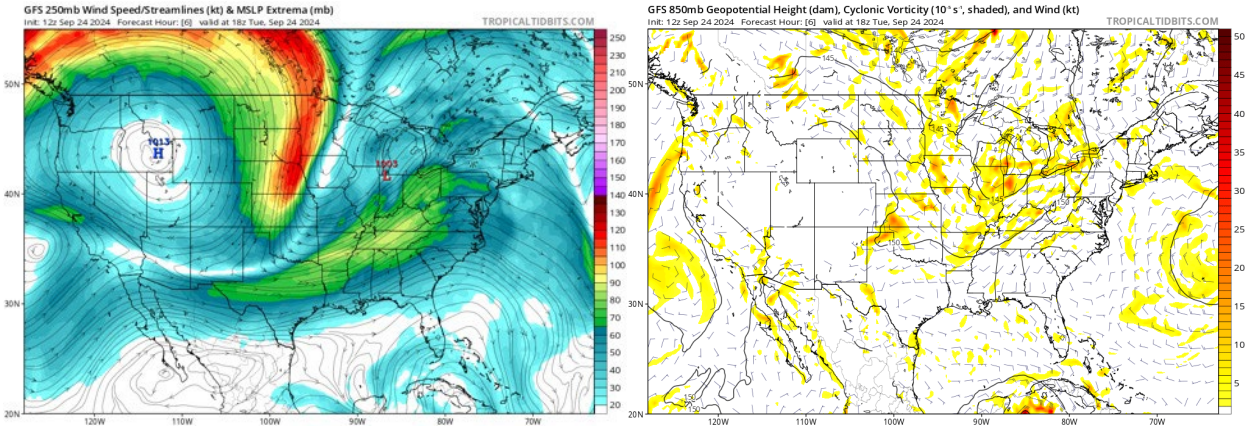

Figure 5.2.3.1: (left) NOAA GFS model six-hour forecasts of the 250 hPa wind speed and streamlines from the 12 UTC run on 24 September 2024. (right) 850 hPa wind barbs, geopotential height, and cyclonic vorticity. Graphics were acquired from the Tropical Tidbits website.

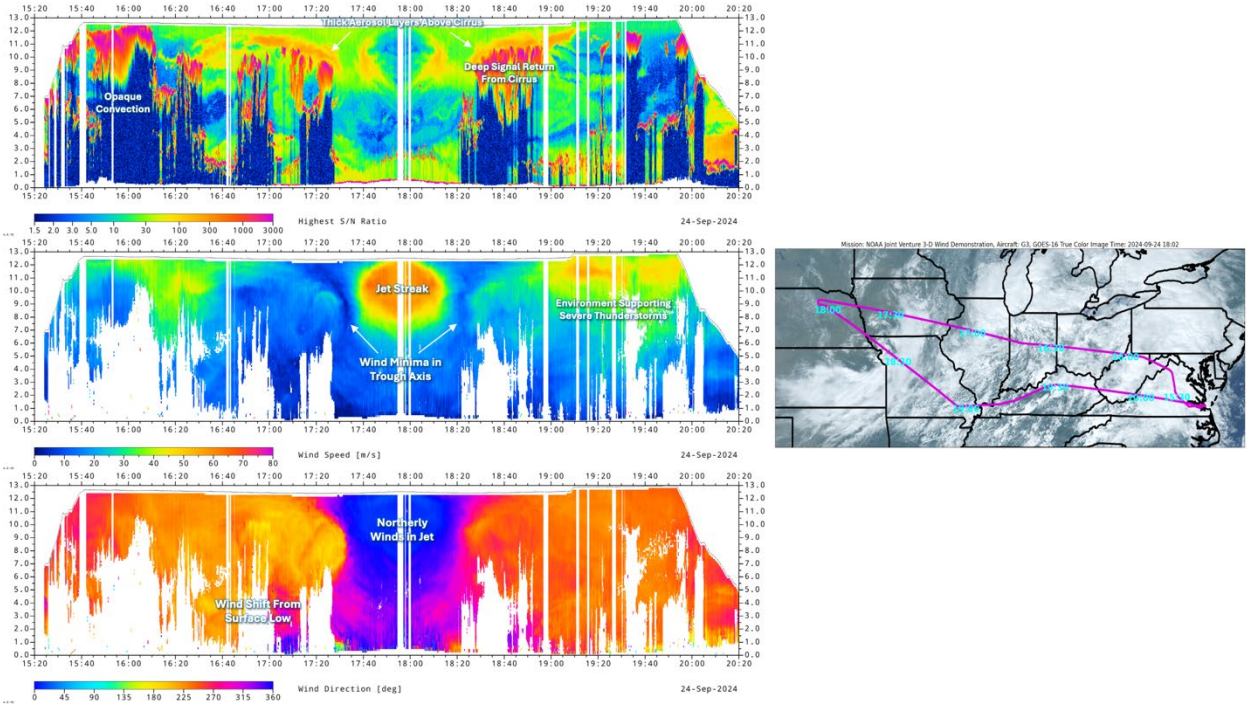

Figure 5.2.3.2: (left) AWP signal to noise ratio (SNR), wind speed and wind direction profiles on 24 September 2024 over the flight track shown in the right panel. White columns in the AWP data curtains indicate aircraft turns where AWP wind vector retrievals are not possible. No dropsondes were released during this flight.

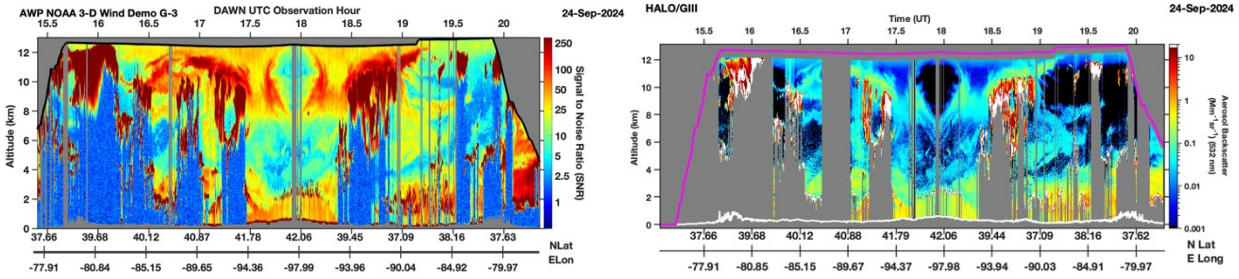

Figure 5.2.3.3: (left) AWP SNR derived from 1200 pulse and 256 data sample retrieval and (right) HALO 532 nm aerosol backscatter for the 24 September 2024 flight.

5.2.4. 15 November 2024 Flight

This flight was a transit from Moffett Field, CA to Hampton, VA to complete the WH^{2}yMSIE/APEX campaign. AWP dwelled continuously for 15 secs at each LOS throughout the flight, identical to what was done at the end of the 13 November flight. The purpose of this scan strategy was to investigate the relationship between signal integration duration and aerosol backscatter sensitivity. 15 second duration combined with a 7.8 km/sec estimated orbit speed corresponding to a 400 km orbit altitude corresponds to a 117 km ground track distance, which is a close to a 1° latitudinal distance (111 km). Within this long duration dwell per LOS, we can incrementally increase the number of pulses used in the integration to demonstrate how backscatter and wind profile retrieval behaves as a function of integration duration. An example of the integration analysis was previously discussed in Section 3.

A plot of the AWP flight track overlaid atop a GOES-16 image, and AWP SNR and wind speed curtains calculated with varying number of AWP pulses used in the retrieval, is shown in Figure 5.2.4.3. A wind direction curtain corresponding to retrieval using 15 sec integration is shown in Figure 5.2.4.2. Early in the flight, the aircraft transected the base of a trough in California and Nevada that extended throughout the troposphere (Figure 5.2.4.1). The low to mid-levels of the profile in this trough region were quite cloudy, depicted by the AWP SNR curtain. A southwesterly jet stream was located on the east side of the trough across Utah and western Colorado. Wind speeds

exceeding 50 m/s were measured by AWP down to a 6 km altitude. An anomalously thick aerosol plume was present at a ~9 km altitude from 1730-1750 UTC over western Utah. HYSPLIT back trajectory analysis initialized at the location and time of plume observation showed extremely rapid transport of the plume airmass from Japan 3 days prior and all the way to northern Iran 5 days prior (Figure 5.2.4.4-left). The source of this plume is unclear, but it was detectable with fewer than 50 AWP pulses and serves as a valuable tracer for wind retrieval. A patch of thick cirrus was present in eastern Colorado from 1815-1830 UTC, likely generated by strong wind flow over the front range of the Rockies. Prior to this cirrus, aerosol backscatter was quite prominent (green to yellow shading) with complex layered structures, likely caused by mountain wave circulations. After 1830 UTC, the airmass changed quite notably, especially in the mid-troposphere where aerosol backscatter decreased significantly. This coincided with the presence of a broad high-pressure ridge centered over Iowa. The presence of a high pressure region is especially evident in the AWP wind direction curtain below 2 km between 1910 and 1925 UTC, where there were abrupt shifts in wind direction coincident with the position of the ridge axis depicted by GFS (Figure 5.2.4.1). The ridge axis appears to tilt with height in the lowest 2 km of the profile, as evidenced by the temporal mis-alignment of the wind direction shifts between 1915 and 1930 UTC. A low-level jet was present across western Nebraska at 2 km where wind speed exceeded 25 m/s. Aerosol backscatter within the PBL and in the upper troposphere was detectable by AWP. Toward the end of the flight, a thick stratus deck was present across Indiana, Ohio, and West Virginia. Layered aerosol structures were present above the stratus up to 6 km altitude. Prior to final descent, a jet streak on the west side of a trough and coastal low pressure system with wind speeds exceeding 45 m/s was briefly sampled from 2000 to 2015 UTC. The aircraft then descended into Virginia for landing at NASA LaRC. Like the 13 November flight, AWP SNR patterns show excellent agreement with HALO 532 nm aerosol backscatter (Figure 5.2.4.5), and reveal the presence of aerosol layers that are near to or beyond the backscatter threshold used for HALO aerosol detection.

As discussed in Section 3 above, increasing the duration of temporal signal integration and including additional lidar samples (e.g. 256 vs 512 data samples in FFT calculations) into the wind retrieval processing has significant impact on the ability to detect signal peaks associated with aerosol backscatter. When just 50 out of the 3000 possible pulses per LOS are used, winds from clouds. and from aerosol within or slightly above the PBL were routinely detected (Figure 5.2.4.3). 50 pulses at 200 Hz pulse rate would have equated to 56 m spacing between profiles from the G-3, and 2 km spacing from space. The enhanced aerosol return in the mid to upper levels of the curtain, as well as within the PBL, was sufficiently strong for a successful wind retrieval at this extremely high spatial resolution. Note that there are a greater number of white stripes in the wind retrieval for 50 shot integration compared to longer integrations. This is caused by the aircraft having attitude variations over very short time intervals that were too large to get a stable wind retrieval. As the number of pulses used in the retrieval increased from 50 up to 3000, SNR increased significantly, as evidenced by increasingly warm color shading in the SNR curtain. The instrument background noise level is apparent in the dark blue shading beneath the opaque cloud in the 1815-1830 UTC timeframe. When 3000 pulses are used, the color shading in what appeared to be an entirely clean mid-tropospheric airmass after 1830 UTC with shorter integration has a brighter hue than the pure noise beneath the thick cloud. This indicates the presence of very diffuse aerosol in this region. The wind speed curtains show that, as a result of the increasing backscatter sensitivity with increasing shot count, the vertical coverage of successful wind retrieval increases significantly. We can also see that, when the pulse count remains constant at 3000, vertical coverage of successful wind retrieval further increases when 512 samples are used in the retrieval compared with the 256 sample run. Around 5 km altitude over eastern Nebraska at 1900 UTC, aerosol backscatter was insufficient for a wind retrieval even after 3000 pulses. A HYSPLIT back trajectory run (Figure 5.2.4.4-right) suggested that this airmass originated from the central Pacific near Hawaii 5 days prior and propagated over the southwest U.S. prior to being observed by AWP. The airmass swirled over the Pacific 5-8 days prior and ascended above a 7 km altitude where there were no known aerosol sources, which would explain the clean airmass.

The results shown in Figure 5.2.4.3 validates the concept and modeling results that has been discussed within the CDWL community for many years, namely that increasing signal integration improves sensitivity to weak aerosol backscatter conditions and increases the frequency of successful wind retrieval (Frehlich 1996). Increasing duration of signal integration does have a tradeoff in that spacing between wind profiles also increases, which reduces the ability to resolve fine scale wind and aerosol features.

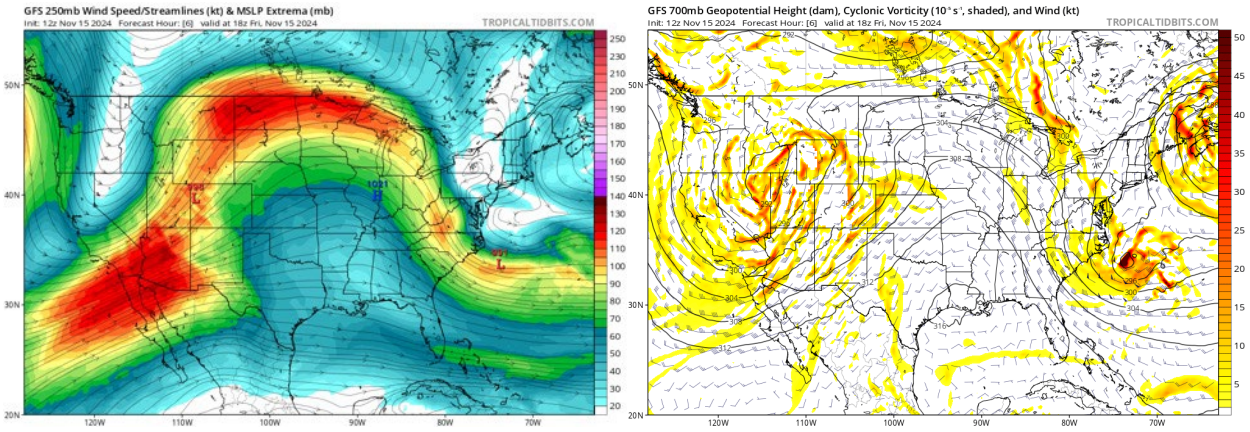

Figure 5.2.4.1: (left) NOAA GFS model six-hour forecasts of the 250 hPa wind speed and streamlines from the 12 UTC run on 15 November 2024. (right) 700 hPa wind barbs, geopotential height, and cyclonic vorticity. Graphics were acquired from the Tropical Tidbits website.

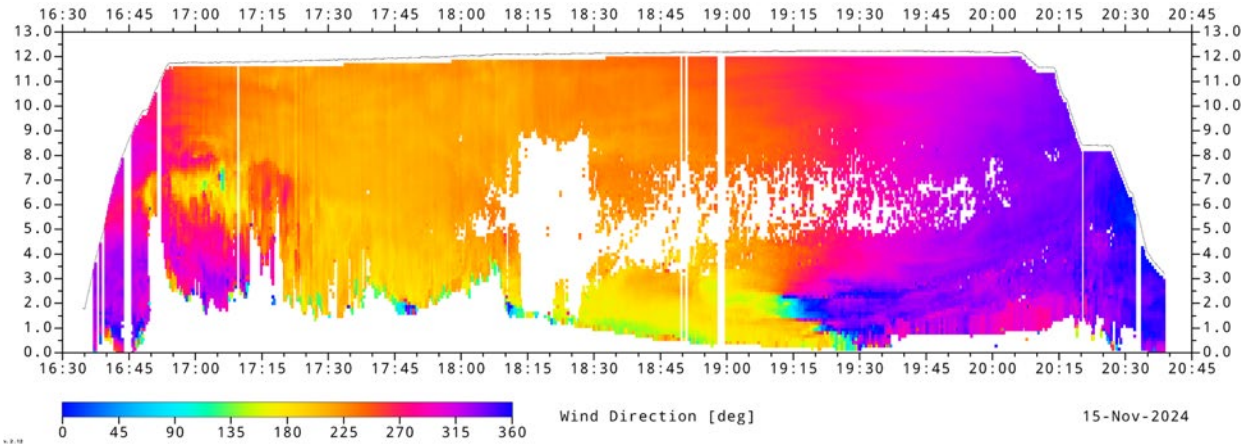

Figure 5.2.4.2: AWP wind direction curtain from the 15 November 2024 transit flight from Moffet Field, CA to Hampton, VA, derived from 3000 pulse integration with 512 data samples used for FFT calculations in each vertical bin.

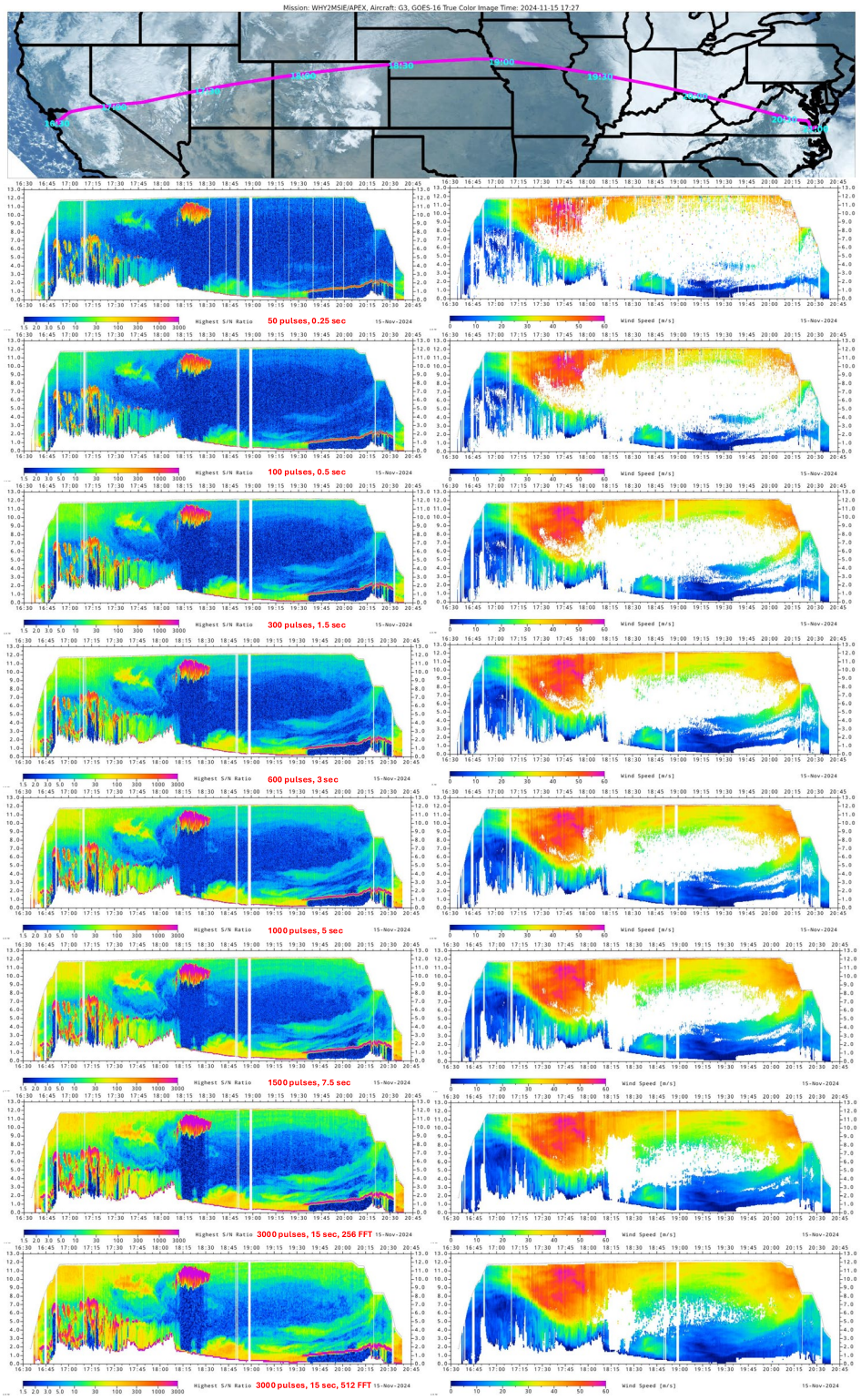

Figure 5.2.4.3: (left) AWP SNR and wind speed curtains on 13 November 2024 along the flight track overlaid on a GOES true color RGB composite shown in the top panel. AWP data in this figure were derived from progressively increasing pulse counts ranging from 50 to 3000 pulses, using 256 data samples (66 meter vertical spacing). The bottom two panels show a comparison between 3000 pulse data based on 256 vs 512 sample FFT processing.

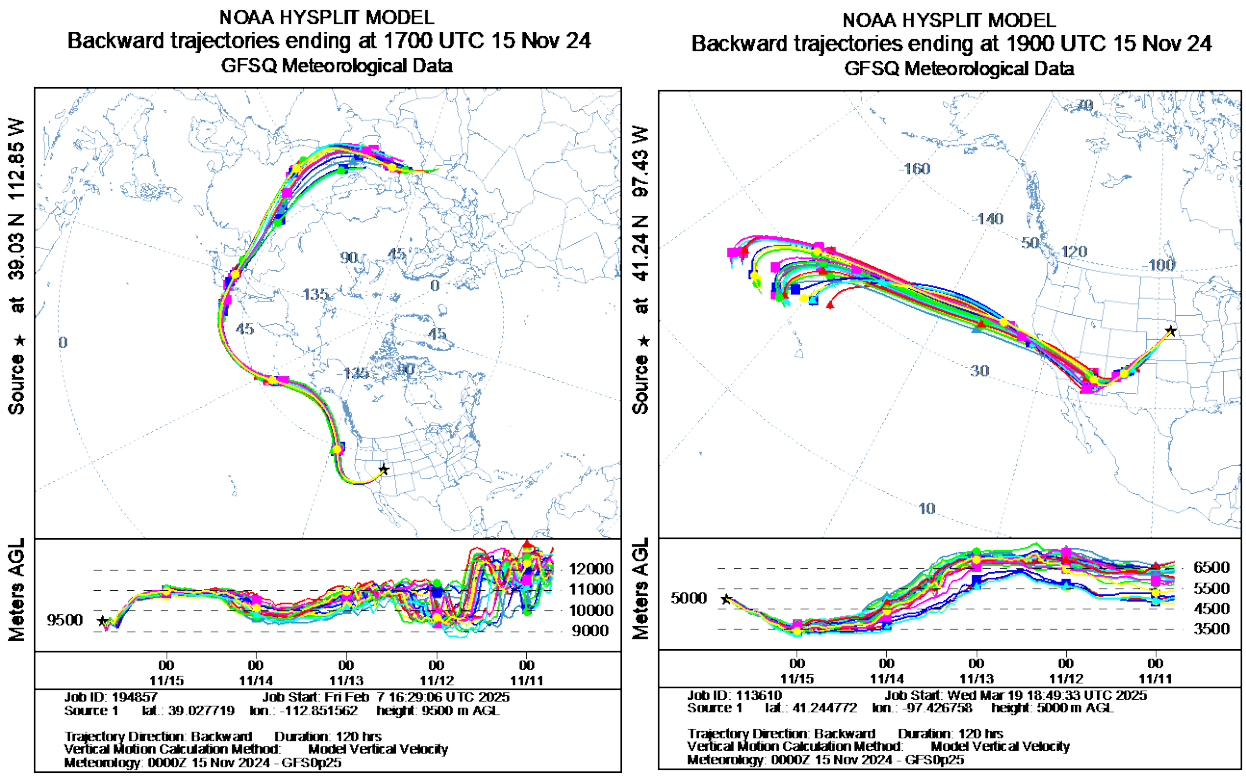

Figure 5.2.4.4: An ensemble of NOAA HYSPLIT back-trajectories initialized from the time and location of a (left) thick aerosol plume over Utah at 9.5 km altitude and 17 UTC and (right) extremely clean atmosphere over Nebraska at 5 km and 19 UTC on 15 November 2024.

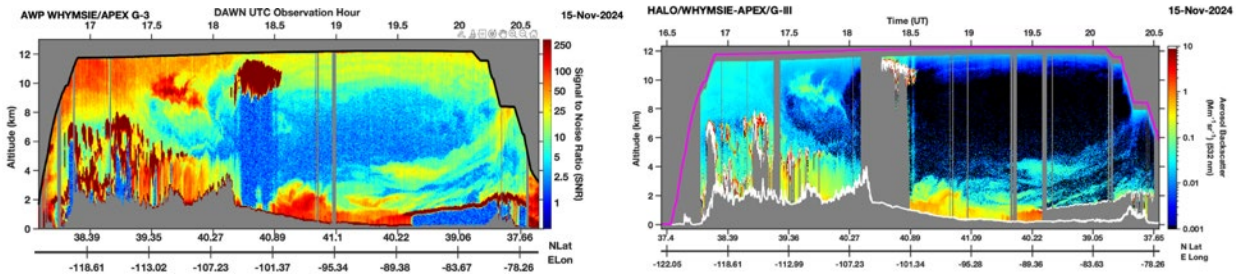

Figure 5.2.4.5: (left) AWP SNR derived from 3000 pulse and 256 data sample retrieval and (right) HALO 532 nm aerosol backscatter for the 15 November 2024 flight.

5.2.5. Additional AWP Flight Data Delivered to NOAA

In addition to the four flights featured in Sections 5.2.1 to 5.2.4, AWP curtain plots throughout NOAA 3-D Wind Demo and WH^{2}yMSIE/APEX flights delivered to NOAA in this project are shown in Figures 5.2.5.1 and 5.2.5.2. These plots illustrate the wide variety of aerosol backscatter, wind speed, and wind direction conditions sampled by the flights. Most flights feature coverage of successful wind retrievals that exceed 75% of the atmospheric column between the aircraft and surface, in regions where the lidar signals were not obstructed by thick cloud. The highest wind speeds were measured in Quebec, Canada on 3 October, where 80+ m/s speed was present in a strong east-west oriented polar jet stream. A thick wildfire plume was also observed on 3 October between 2 and 5 km altitude from 1420-1500 UTC. Hurricane-force winds near 40 m/s were measured over Florida on the eastern side of Hurricane Helene during 26 September Flight 2. On October 8, the G-3 descended down to a 7.5 km altitude to overfly a wind turbine installation within the NOAA-DOE Wind Forecast Improvement Project – 3 domain (WFIP-3) in order to minimize

spacing between the 2 LOS near the ocean surface, as well as to collected detailed PBL measurements over the Hampton Roads Virginia region at end of flight. The 14 November flight was a cloud-process study oriented flight with repeated tracks over a limited domain offshore of central CA. This explains the repetition of wind and SNR patterns evident after 1745 UTC on this day. On some flights such as 26 September Flight 1 and 27 October, clouds provided sufficient signal for wind retrieval over a 5-6 km deep layer. Clouds in general typically provided SNR 400 times greater than the instrument noise floor, and would be easily detectable from space. Wind speed varied by up to ~30 m/s throughout the cloud depth, highlighting the utility of cloud cover for heterodyne lidar wind profiling. SNR regularly exceeds 100 in the PBL, but decreases to levels between 2 and 100 in the free troposphere above the PBL where aerosol concentrations are reduced. Gaps in the profile usually occurred in the 4-8 km altitude layer where the atmosphere typically had the lowest aerosol concentration. Three flights, 1 and 30 October, and 7 November, featured environments with weak aerosol backscatter. It is important to note that after 2215 UTC on 7 November, AWP sampled at 2 sec per LOS instead of 6 sec like earlier in the flight, in order to capture higher detail in a wildfire smoke plume to be encountered at 2300 UTC from the Ventura County California “Mountain Fire”. As was previously discussed with Figure 5.2.4.3, duration of pulse integration per LOS has significant impact on the vertical coverage of successful wind retrievals. Nevertheless, “clean” aerosol-free layers present the greatest challenge to a 2 µm heterodyne wind lidar which are dependent on Mie scattering for wind signal. HYSPLIT modeling of clean mid-tropospheric airmasses over the Pacific indicated that they typically spend several days lingering in the central Pacific where there are no aerosol sources. Aerosol rich airmasses were rapidly transported from Asia or originated over the U.S. Sufficient signal for wind retrieval in clean airmasses can sometimes be extracted with longer pulse integration duration or deeper vertical integration (i.e. increased number of raw data samples) at the expense of wind profile spatial/vertical resolution (Section 5.2.4).

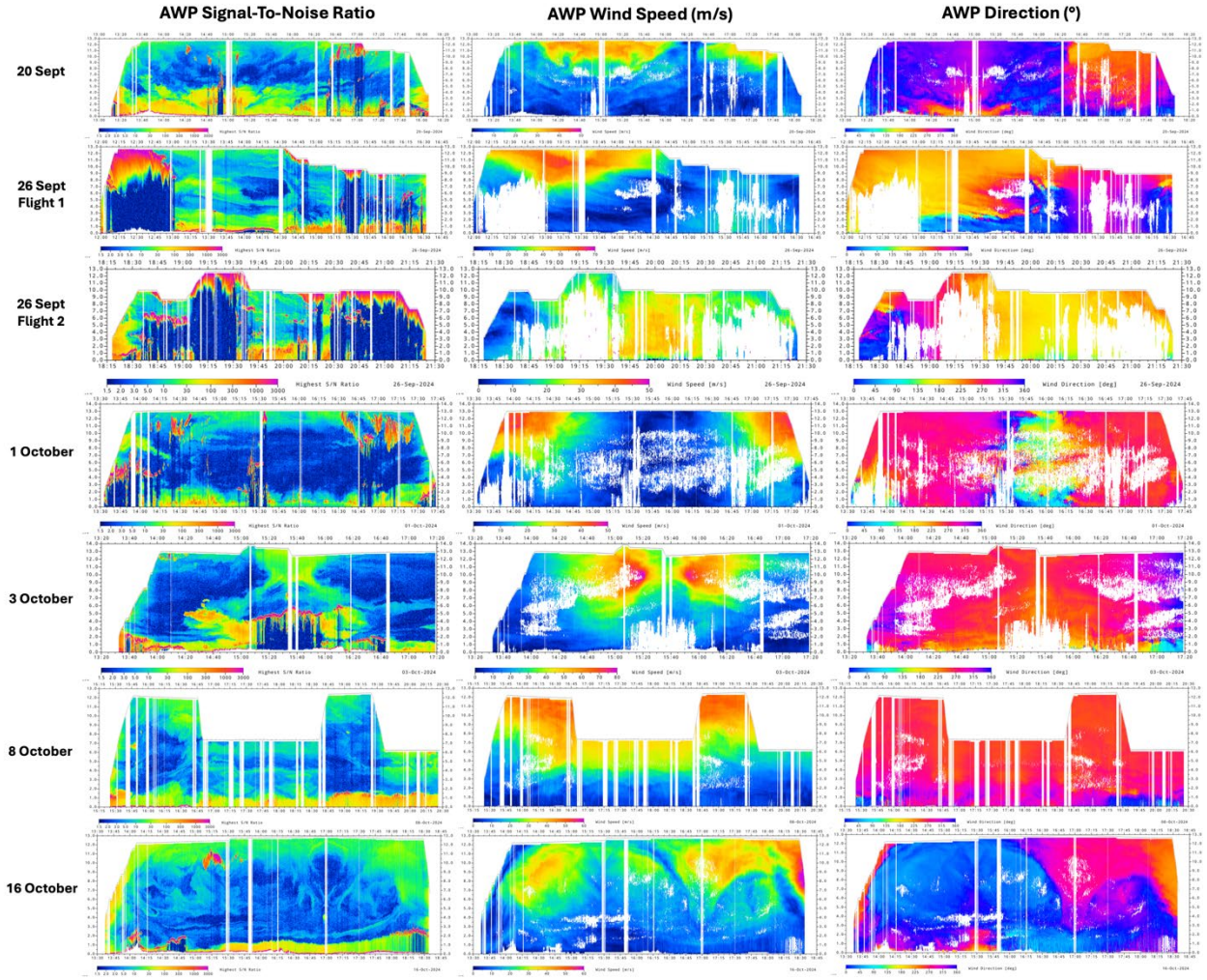

Figure 5.2.5.1: AWP SNR (left column), Wind Speed (middle), and Wind Direction (right) curtains of data from NOAA 3-D Wind Demonstration flights based from Hampton, VA that was delivered to NOAA for this project. Note that the color range for wind speed is not constant from flight to flight, and is adjusted per flight to emphasize details in the wind patterns.

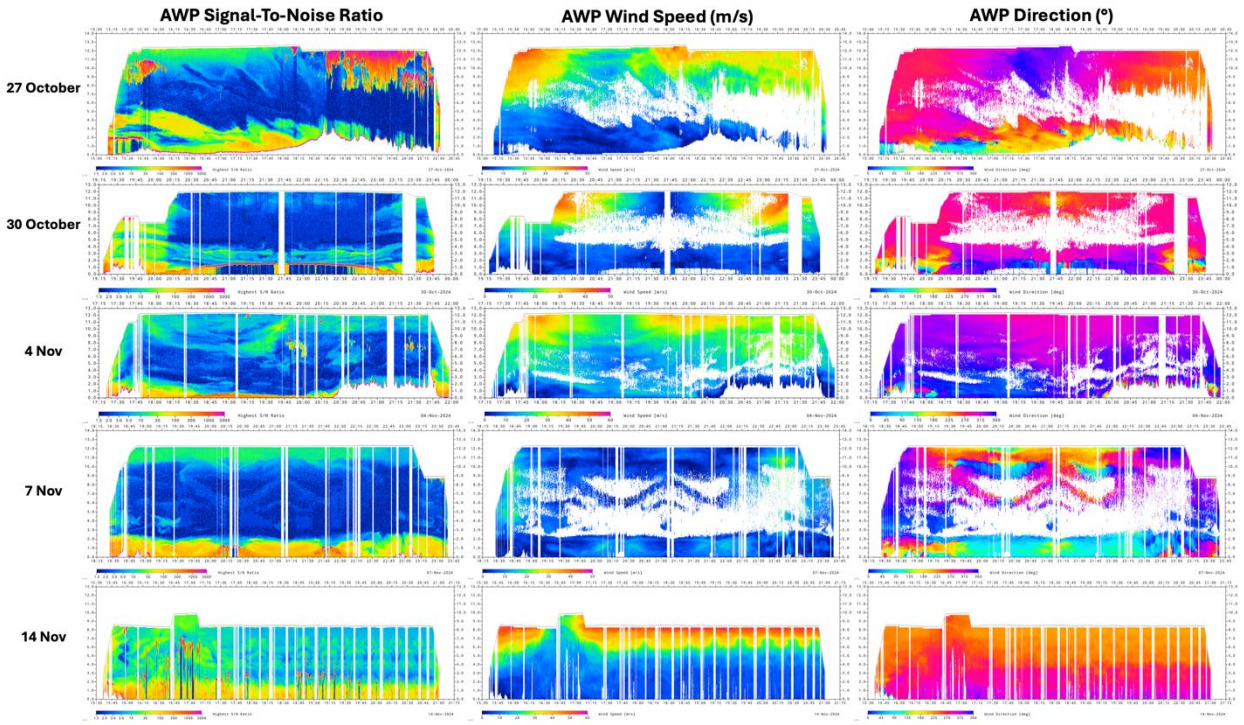

Figure 5.2.5.2: AWP SNR (left column), Wind Speed (middle), and Wind Direction (right) curtains of data from WH²yMSIE/APEX flights based from Santa Maria or Moffett Field, CA that was delivered to NOAA for this project. Note that the color range for wind speed is not constant from flight to flight, and is set per flight to emphasize details in the wind patterns.

5.3. Vertical Coverage of Successful AWP Wind Retrievals

AWP data was analyzed to quantify the frequency of successful wind retrieval as a function of altitude, using high altitude flight segments (≥ 11.5 km) compiled across all the Fall 2024 flights. The success rate is separated by whether or not the profile contained a cloud, which was defined as any altitude bin with an SNR exceeding 425. SNR was found to reach this level only in cloudy conditions. In cloud-free conditions, AWP detected sufficient signal for wind retrieval 65-100% of the time (green curve, Figure 5.3.1). The layer from 4-8 km altitude typically had the weakest signal return, leading to a 65-75% success rate. Signal return was especially prominent within and near to the PBL where success rate was ~95%. Several of the flight examples shown above indicate that AWP lidar pulses often could penetrate through clouds and profile the airmass below them. The 24 September flight showed that sufficient signal for wind retrieval was provided by clouds over an atmospheric depth extending 5 km beneath the cloud top. But in some instances, clouds such as stratus overcast are simply too opaque and the laser energy cannot penetrate them. Winds were successfully retrieved 45-95% of the time when clouds were encountered at some level between the aircraft and surface (red curve, Figure 5.3.1). Winds were detected in the lowest km of the profile for 55-70% of occurrences. *Such a high success rate in cloudy conditions demonstrates the utility of heterodyne Doppler wind lidars for profiling in complex conditions that other technologies such as IR sounders would not have been able to measure.*

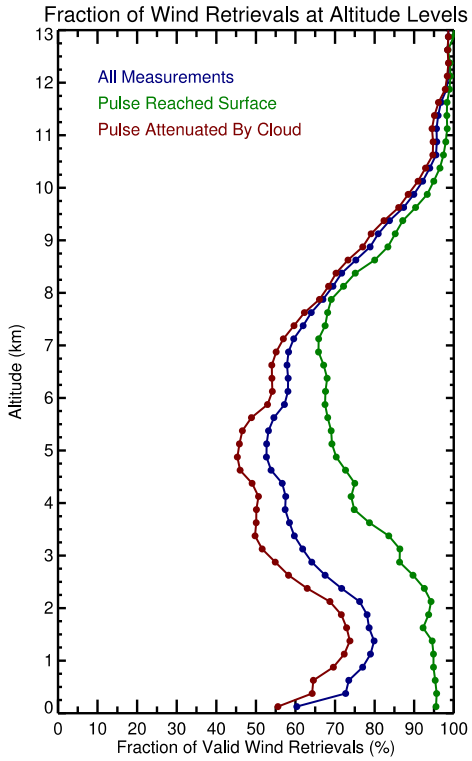

Figure 5.3.1: The fraction of successful wind retrieval, derived from data from all flight segments above a 11.5 km altitude, a lower limit for the typical Gulfstream-III cruise altitude experienced during the Fall 2024 flight campaigns. The success rate is separated by whether or not the profile contained a cloud and reached the surface. A cloud was defined as an SNR exceeding 425. Analysis indicated that AWP SNR does not reach this level in cloud free conditions. The lidar pulse reached the surface if there was an SNR above the AWP noise level in the vertical bin immediately above the surface, defined by the ETOPO dataset.

5.4. AWP Validation With AVAPS

A total of 73 AVAPS dropsondes (referred to as "sondes" hereafter) were released during the NOAA 3-D Wind Demo and WH^{2}yMSIE/APEX. AVAPS sondes were selectively released to capture features such as atmospheric wind, water vapor, and temperature gradients, localized wind speed or water vapor maxima/minima, and gaps in clouds to provide an opportunity for comparison of lidar data with as full as possible coverage and variety of conditions between the aircraft and the surface. Both AWP and AVAPS data require pre-processing steps prior to comparison. AVAPS data is quality-controlled with a human supervised automated algorithm from a software package called ASPEN (Martin and Suhr 2021). ASPEN is the standard software used across the community for AVAPS quality control (QC). As noted above, AWP provides data products with 66 meter spacing in the vertical dimension, whereas AVAPS collect data with 2 Hz frequency and 5-8 meter spacing between vertical levels. AVAPS data are vertically averaged to approximate the AWP spacing. AVAPS sondes fall to the ocean surface with a parachute, making them especially susceptible to wind drift during their ~13 min descent, based on a sonde release from 13 km altitude. If winds were perpendicular to the aircraft track, a sonde could be carried > 20 km across track in strong wind conditions. This could incorporate notable spatial variability to the validation if not accounted for in some way. AWP data are weighted-averaged over a 150-second time window which would encompass a ~34 km spatial distance assuming a nominal 225 m/s ground speed. The profile at the center of the time window is weighted highest, and the weighting drops off to zero at the end of the window, as was described in Section 3. This has the net effect of encapsulating spatial wind variability into the smoothed product, while also filling in data gaps associated with aircraft turns. All co-located AWP and AVAPS data are then directly compared. There were no AWP outliers excluded from the

analysis.

Examples of comparisons between AWP, sondes, and NOAA Global Forecast System (GFS, magenta) and High Resolution Rapid Refresh (HRRR, green) model initial analysis profiles, and GOES AMVs (when co-located with the aircraft track) are shown in Figure 5.4.1. The close agreement between the AWP (red) and sonde (black) curves, in addition to those shown in Figures 5.2.1.2 and 5.2.2.2 above, continue to demonstrate the high vertical detail and precision offered by AWP. These profiles capture a wide variety of wind speed and direction conditions and vertical wind shear layers representative of conditions that could be present throughout the world. The GFS and HRRR model also agree well with the sonde and AWP data, with the exception of a couple layers with outliers depicted by HRRR within Hurricane Helene (Figure 5.4.1a) and over the Atlantic east of the Carolinas (Figure 5.4.1b). Comparisons between AWP, GFS, and HRRR will be further discussed in the following Section 5.5.

Co-locations between AWP and sonde vector wind speed, and u- and v-component speed from all flights are compiled in Figure 5.4.2. AWP had minimal bias (.05 m/s), a correlation of 0.9963 with sonde, and uncertainty (or random error) of just 0.92 m/s. U- and V-component winds showed similarly excellent agreement. These statistics are the best of all validation with sonde derived from any previous DAWN or AWP flight campaign (e.g. Bedka et al. 2021). There is greater uncertainty at the slower wind speed end of the spectrum. The primary reasoning for this is noted above; the sonde drifts as it descends, and by the time it reaches the planetary boundary layer, it is furthest from the AWP measurement location. Winds in the lower atmosphere are typically slowest, so spatial variability in lower atmosphere increases discrepancy between the AWP and sonde measurements.

Due to the high number of collocations with the dropsondes, AWP accuracy can be further evaluated as a function of wind speed (Table 5.4.1). There is strong agreement between AWP and dropsonde measurements across a range of wind conditions. The largest discrepancies occur under the weakest wind conditions (0-2.5 m/s), where directional differences are most pronounced. These larger direction errors are expected, as small variations in the U- and V-wind components can lead to substantial changes in calculated wind direction at low speeds. However, despite the larger directional differences, the wind speed vector bias and RMSD remain small in this regime, indicating that AWP accurately captures the overall wind magnitude even when directional uncertainty is higher. The best agreement occurs at the strongest wind speeds (>20 m/s), where the wind speed bias is negligible and the RMSD is < 0.8 m/s. Directional differences are also smallest in this category, with a bias near zero and an RMSD of just 1.5°, demonstrating excellent consistency between AWP and dropsonde observations in high-wind environments. These results highlight the robustness of AWP wind measurements across a wind range of wind speed regimes, with the largest differences confined to light wind regimes, where small absolute differences can result in relatively larger errors in direction.

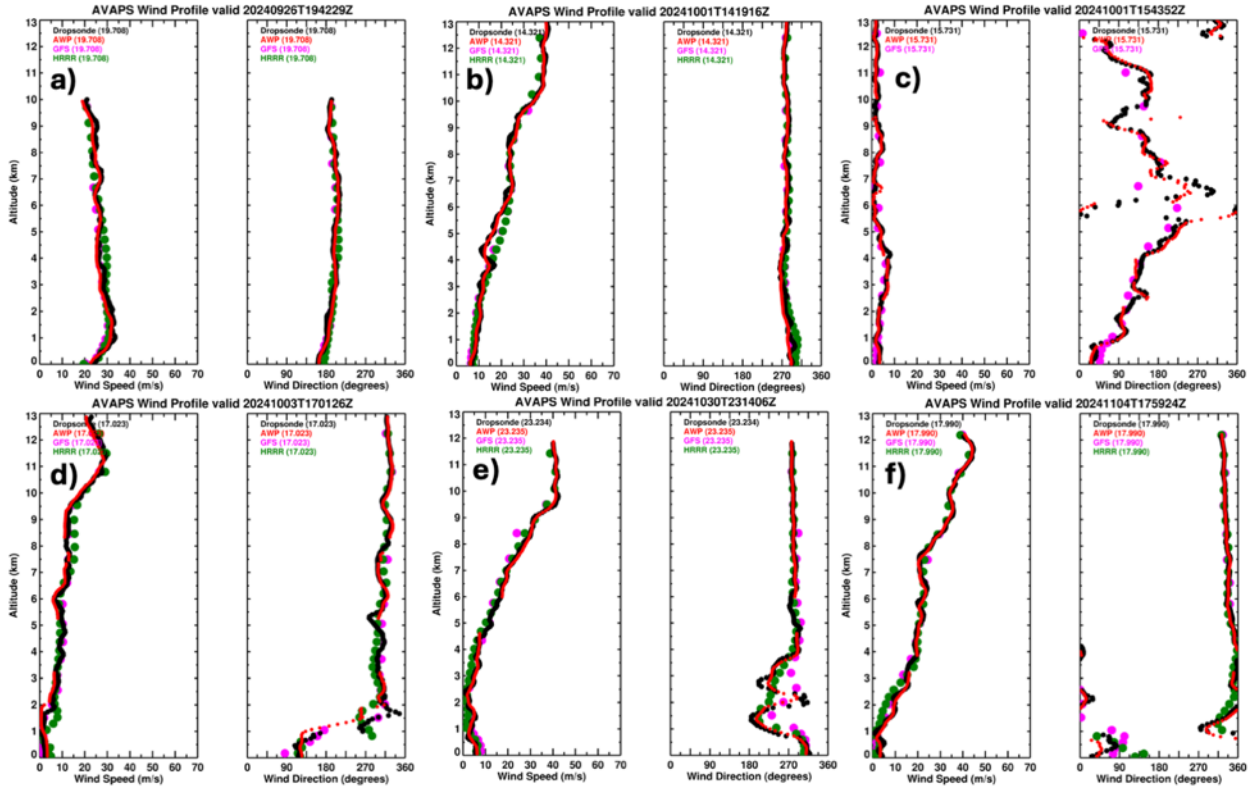

Figure 5.4.1: Six comparisons between AVAPS dropsonde, AWP, NOAA GFS and HRRR model data, and GOES-16/18 AMVs throughout the Fall 2024 flights.

Figure 5.4.2: Comparison between AWP and AVAPS dropsonde wind speed (top), U-component (lower-left), and V-component (lower-right) for all co-locations during the Fall 2024 campaigns.

Wind Speed Range (m/s)	Total Comparisons	Speed Bias ± RMSD (m/s)	U-Component Bias ± RMSD (m/s)	V-Component Bias ± RMSD (m/s)	Direction Bias ± RMSD (°)	Wind Vector Bias ± RMSD (m/s)
0-2.5	343	-0.229 ± 0.786	-0.181 ± 0.834	-0.157 ± 0.797	6.139 ± 32.723	0.902 ± 0.757
2.5-5	984	-0.132 ± 0.862	-0.169 ± 0.934	-0.002 ± 0.810	2.066 ± 14.409	0.954 ± 0.805
5-10	2238	0.192 ± 1.091	0.013 ± 1.151	-0.088 ± 1.000	-0.046 ± 9.271	1.130 ± 1.028
10-15	1449	0.078 ± 1.010	-0.027 ± 0.964	-0.101 ± 0.947	0.414 ± 4.513	1.047 ± 0.860
15-20	1284	-0.053 ± 0.972	-0.136 ± 1.124	-0.090 ± 1.030	0.329 ± 3.980	1.137 ± 1.028
>20	3754	0.058 ± 0.759	-0.001 ± 0.782	-0.077 ± 0.789	0.101 ± 1.491	0.901 ± 0.654

Table 5.4.1: Comparison of AWP wind measurements with collocated dropsonde observations, grouped by dropsonde wind speed. For each wind speed category, the bias and root-mean-square difference (RMSD) are provided for total wind speed, u- and v-wind components, wind direction, and wind speed vector differences – defined as the square root of the squared AWP-AVAPS U- and V- component differences.

5.5. AWP Comparisons with NOAA Numerical Weather Prediction Model Data

AWP data is averaged to the spatial and vertical resolution of the NOAA Global Forecast System (GFS) and High-Resolution Rapid Refresh (HRRR) models to assess their performance. GFS and HRRR data were analyzed at the time of the initial analysis, and then at various forecast lead times out to 168 hours for GFS and 18 hours for HRRR. GFS provides forecasts at 6 hourly timesteps and 0.25° horizontal spacing. HRRR provides forecasts at hourly timesteps and 3 km horizontal spacing. Both models have variable and differing spacing between vertical levels from the surface to the AWP flight altitude which are accounted for in the averaging. For AWP observations between GFS model timesteps, linear interpolation was done. For example, for a 13 UTC AWP observation and comparison against the GFS initial analysis timestep, GFS analyses from the 12 UTC and 18 UTC runs were linearly interpolated to acquire data at 13 UTC. For HRRR, interpolation was not done due to the significantly greater computational resources required to deal with this higher spatio-temporal resolution data. The nearest HRRR timestep to the AWP data was used for comparison.

Figure 5.5.1 shows a histogram comparison of GFS (left) and HRRR (right) forecasts relative to AWP measured wind speed. For both GFS and HRRR, as forecast lead time decreases. the RMSD improves. In addition, the number of comparisons screened out due to wind speed or component wind speed differences > 10 m/s decreases as the forecast lead time decreases (not shown). The mean biases for both models fluctuate between -0.1 and -0.7 m/s, suggesting both models slightly underestimate wind speeds relative to AWP for all forecast hours. While the wind speed mean bias does not consistently decrease as the forecast lead time decreases, the vector wind bias (the square root of the squared AWP-model U and V component differences) does progressively decrease (Figure 5.5.2). For GFS (HRRR), the vector wind difference bias decreases from 5.6 (2.7) m/s at the 168 (18) hour forecast lead time to 2.2 (2.1) m/s at the time of the initial analysis.

To visualize how the GFS and HRRR initial analyses (0-hour forecasts) perform relative to AWP, example curtain plots along the flight track are presented in Figures 5.5.3 and 5.5.4. The figures display AWP wind speed averaged to the GFS/HRRR grid, the GFS/HRRR wind speed, and the wind speed difference between the models and AWP for the 15 October and 15 November flights, respectively. These curtain plots highlight how small differences in the location or altitude can greatly impact model performance. Overall, both models perform well relative to AWP for these flights, with small wind speed differences (indicated by green and yellow shading in the rightmost panels). Comparing the AWP and model wind speed panels (left and middle), the profiles often appear nearly identical. However, there are notable instances where the models struggle to capture key features, leading to large differences in wind speed (dark red and dark blue shading in the rightmost panels). For example, in Figure 5.5.3 between 19-20 UTC on 15 October, the G-3 flew over a mid-level jet. In this case, GFS underestimated the full vertical extent of the jet observed by AWP, while HRRR captured it more accurately, resulting in a large positive bias in the GFS difference panel. Later in the same flight, after 2030 UTC, a similar situation occurred as the G-3 encountered a jet stream. Here, HRRR forecast the jet stream to appear earlier in the flight than observed by AWP, while GFS forecast it to appear later. Additionally, GFS underestimated the wind speeds between 4–6 km compared to the AWP observations.

In Figure 5.5.4, from 17–18 UTC on 15 November, HRRR forecast the jet to occur earlier in the flight than observed. During this time, mountain waves were also present near the surface (2–3 km altitude). While AWP is capable of capturing these small-scale wave features and their associated wind speed variations, even when averaged to the coarser GFS and HRRR grids, the models tend to smooth out these details resulting in larger wind speed differences. Otherwise, the initial analyses from both models performed quite well during this flight.

Figure 5.5.5 shows the same flight as Figure 5.5.3 but for the GFS 168-hour forecast, rather than the initial analysis. Compared to AWP, the 168-hour forecast exhibits substantial wind speed errors throughout the flight. Prior to 20 UTC, the GFS notably overestimates wind speeds within both the mid-level and upper-level jets. After 20 UTC, as the aircraft revisits the upper-level jet, the forecast substantially underestimates the wind speeds, suggesting a timing offset in the model's representation of the jet at this location. In addition to these timing errors, the GFS misplaces the vertical extent and position of the wind features, resulting in pronounced wind speed biases exceeding ±10 m/s. These errors highlight how the model's ability to forecast jet structure and evolution can degrade in longer-range forecasts.

Figure 5.5.1: Comparison between AWP and GFS (left) and HRRR (right) for all co-locations during the Fall 2024 campaigns.

Figure 5.5.2: Vector wind speed bias and RMSD between AWP and GFS (blue) and HRRR (red) forecasts for all co-locations during the Fall 2024 campaigns.

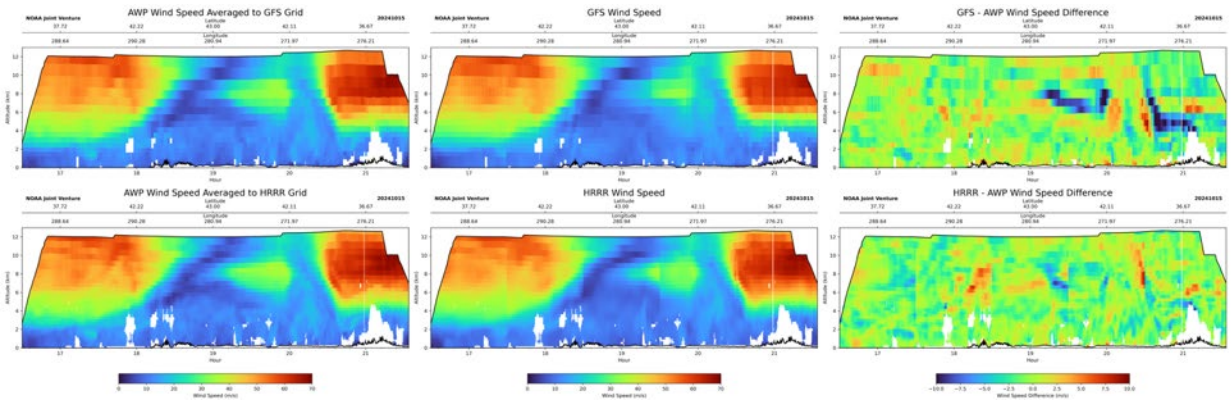

Figure 5.5.3: Curtain plots along the flight track for 15 October 2024. Top) GFS model analysis Bottom) HRRR model analysis. Left) AWP averaged to model grid. Middle) Model analysis wind speed along flight track. Right) Wind speed difference between AWP and model analyses.

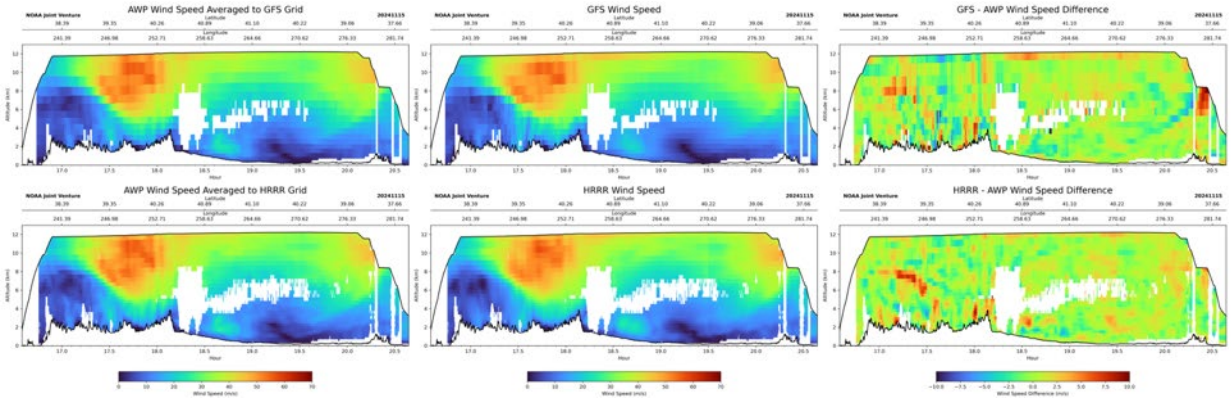

Figure 5.5.4: Curtain plots along the flight track for 15 November 2024. Top) GFS model analysis Bottom) HRRR model analysis. Left) AWP averaged to model grid. Middle) Model analysis wind speed along flight track. Right) Wind speed difference between AWP and model analyses.

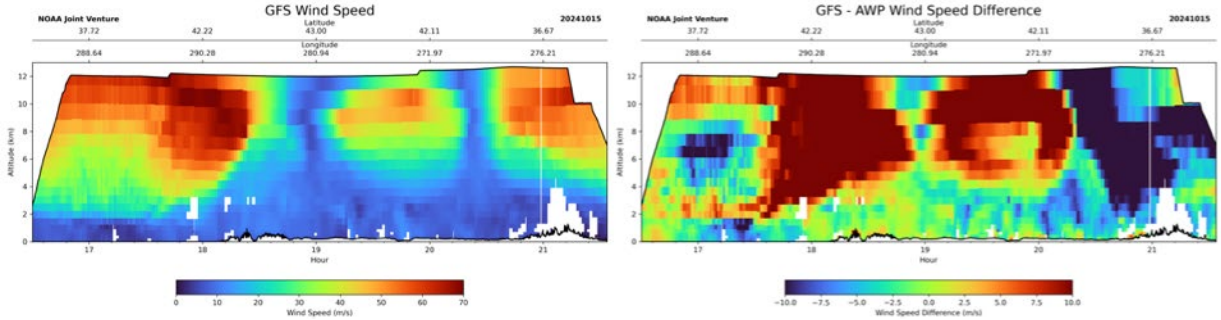

Figure 5.5.5: Left) GFS 168-hour forecast along flight track for the 15 October 2024 flight. Right) Wind speed difference between AWP measured wind speed and 168-hour GFS forecast.

5.6. AWP Comparisons with GOES-16/18 Atmospheric Motion Vectors (AMVs)

AWP data is matched in time and space with GOES-16 (i.e. GOES-East) and GOES-18 (i.e. GOES-West) AMV data to assess their performance. All AMV data was acquired from the Google Cloud Platform GOES data repository (Google, 2025). AMVs are derived from the 0.64 μm visible, the 11.2 μm IR window, the 6.2 μm upper-level (UL) water vapor, 6.9 μm mid-level (ML) water vapor, and 7.3 μm low-level (LL) water vapor (WV) channels. There are two separate products derived from the UL WV channel to differentiate clear sky and cloudy conditions. Because AMV data are provided as a function of pressure, GFS initial analysis pressure and geopotential heights are used to derive AMV altitudes. AMV data are considered a match with AWP if the AMV data was collected within 15 mins temporally, 25 km spatially, and 0.25 km vertically from the AWP measurement and height assignment. If multiple AWP measurements temporally and spatially match with an AMV then the nearest valid AWP measurement in space is used for comparison.

Figure 5.6.1 shows wind speed and direction comparison histograms for AWP and AMVs from various GOES channels. Most comparisons between AWP and GOES were AMVs estimated from the visible channel which exhibits a near zero bias (0.016 m/s and 0.757°) and a relatively narrow uncertainty (±1.469 m/s and ±8.752°). Figure 5.6.2 shows that all of these comparisons with visible AMVs occurred below a 3 km altitude, which is the upper altitude limit for the current GOES visible AMV algorithm. The 11.2 μm IR channel had the next highest number of collocations with AWP and displayed minimal biases and standard deviations. Most of these collocations also came from below 3 km altitude but, unlike the visible channel, there were collocations throughout the atmospheric column. Conversely, the lower-, mid-, and upper-level clear sky WV channels have larger biases and broader spreads, suggesting greater uncertainty in wind speed and direction from these channels. This may be caused by greater

height assignment uncertainty for clear sky WV AMVs, given that WV radiances emanate from a much deeper atmospheric layer than cloudy radiances (Velden and Bedka 2009).

To contextualize the magnitude of wind speed discrepancies relative to the observed winds, the middle panel in Figure 5.6.1 illustrates the cumulative distribution of wind speed percent difference relative to AWP wind speed. Approximately 80% of the visible, cloudy UL WV, and IR channel retrievals fall within ±20% of AWP wind speeds, with the cloudy UL WV notably achieving the steepest cumulative rise, reflecting high consistency. While visible AMVs had lowest overall uncertainty, winds in the 0-3 km are typically weakest. UL WV cloudy AMVs measured stronger winds, and had also a better relative agreement with respect to AWP speed. In contrast, clear sky WV channels exhibit greater percent differences, with only around 60–70% of samples within ±20%, and more gradual cumulative distributions, emphasizing greater variability. These results further indicate enhanced performance of the visible, IR, and cloudy UL WV channels in capturing accurate wind speeds, compared to the more uncertain clear sky WV-derived winds.

AMV data are further evaluated relative to the time interval between GOES images, specifically if they were derived from GOES 10-min Full-Disk, 5-min CONUS sector, or 1-min Mesoscale Domain Sector (MDS) data. GOES MDS data were requested and granted for many AWP flights, enabling an assessment of AMVs performance as a function of image temporal resolution, summarized in Table 5.6.1. Across all scan strategies combined, GOES wind speed retrievals exhibit a near-zero bias with RMSD < 1.8 m/s. As noted previously, this is largely attributed to the predominance of collocations with the 0.64 μm visible channel in 0-3 km altitude layer. When broken down by scan strategy, the MDS provides the most samples despite not being available for not every flight. MDS collocations also exhibit the greatest precision relative to AWP, with the smallest standard deviations in wind speed and direction. These results suggest that the higher temporal resolution of MDS sampling likely contributes to improved wind retrievals. In contrast, Full Disk scan collocations exhibit the poorest precision, likely due to greater challenges with feature tracking when there is a greater time interval between images.

Though AWP and AMV agreement was generally quite favorable, a key issue commonly attributed to AMVs is height assignment error. Cloud top and base could be estimated from AWP data to quantify height assignment error, with the inherent assumption that the AMV should have been assigned to the physical cloud top. Velden and Bedka (2009) showed that AMVs best agree with a layer mean wind flow extending over some distance beneath the AMV height assignment. Our team was not able to complete a quantitative assessment of height assignment accuracy prior to submission of this report. This will be a topic for future work. But, a curtain plot of AWP SNR and height assignment for the 24 September flight, where cloud top and base are evident for many clouds throughout the flight, is shown in Figure 5.6.3 to highlight examples of varying AMV height assignment accuracy. AMVs were assigned over 1 km deep into the cloud for clouds within the 8 to 12 km altitude layer from ~1530-1600 UTC, 1645-1700 UTC 1715 UTC, and 1830-1900 UTC. Height assignments were 1+ km too low for clouds at the PBL top around 18 UTC. Height assignment was quite good for low cloud at 1630-1645 and 1855-1930 UTC. AMVs outside of cloudy regions between 6 and 9 km at various times during the flight were derived from clear sky WV feature tracking. It is difficult to disentangle how much AWP and AMV wind agreement would change if AMVs were assigned nearer to the tops of observed cloud features.

Figure 5.6.1: Comparison between AWP and GOES channel AMV wind measurements (color coded by GOES channel) for all co-locations during the Fall 2024 campaigns. GOES-16 (used for flights out of Virginia) and GOES-18 (used for flights out of California) were both used in identifying co-located AMVs. Left) AWP and GOES AMV wind speed difference histogram. Middle) AWP and GOES AMV wind speed percent difference cumulative frequency histogram. Right) AWP and GOES AMV wind direction difference histogram.

Figure 5.6.2: GOES AMV altitude assignments that were collocated with AWP for a variety of GOES ABI channels.

Satellite Scan Pattern	Speed Bias ± RMSD (m/s)	Direction Bias ± RMSD (°)	Vector Bias ± RMSD (m/s)	Number of Samples
All	-0.011 ± 1.786	0.569 ± 8.834	1.945 ± 1.607	48326
Full Disk	-0.028 ± 2.122	0.998 ± 9.910	2.294 ± 1.798	2457
CONUS	-0.058 ± 1.849	0.783 ± 9.670	2.039 ± 1.643	15225
MDS	0.014 ± 1.723	0.428 ± 8.287	1.870 ± 1.566	30644

Table 5.6.1: Comparison between AWP and GOES derived AMVs stratified by satellite scan strategy.

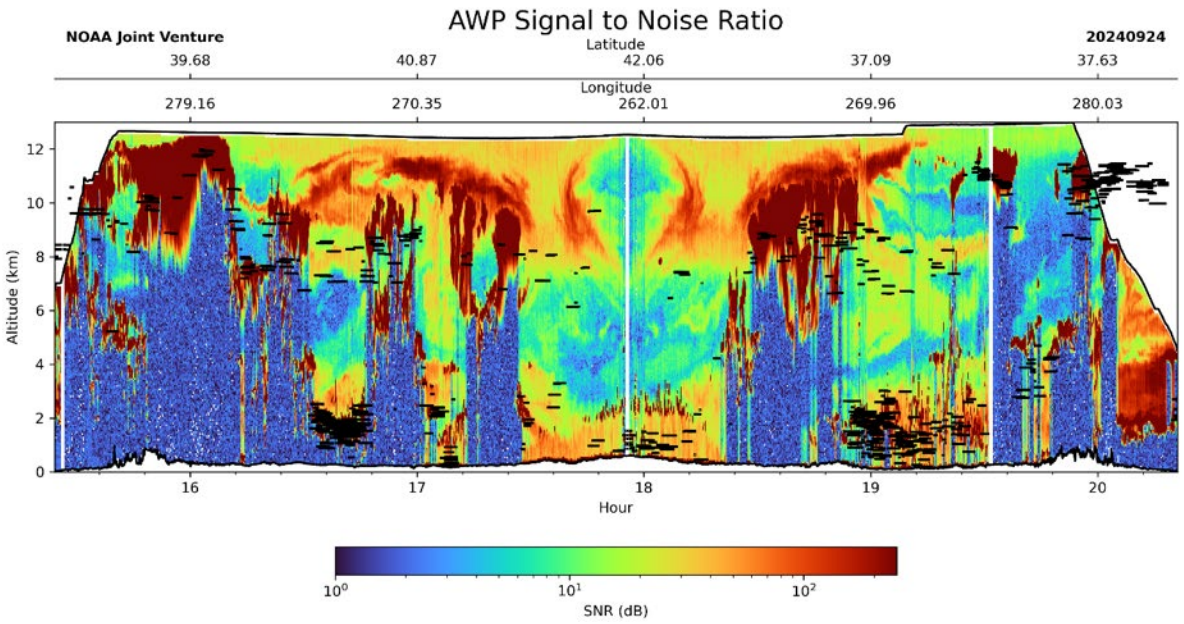

Figure 5.6.3: AWP SNR curtain on 24 September 2024, overlaid with GOES-16 AMV heights (horizontal black symbols) derived from a combination of AMVs from 10-min Full Disk, 5-minute CONUS, and 1-minute Mesoscale Domain Sector scans that were co-located in time and space with AWP data. Co-located AMVs are displayed for up to a 3 min period to improve their visibility atop the SNR curtain. Clouds are indicated by deep maroon color shading in the SNR data.

6. Space-Based Simulation of a Heterodyne Wind Lidar Performance

A NASA LaRC Earth-orbiting, coherent Doppler wind lidar mission concept, the Orbiting Wind Profiler (OWP), utilizes a novel, compact, state-of-the-art 2-micron wavelength, pulsed, Ho:LuLiF solid-state laser that would transmit pulses alternately in two line-of-sight (LOS) directions. A small fraction of the total transmitted pulse is backscattered by atmospheric aerosols and cloud particles directly into the lidar receiver which is coaxial with the transmitted pulse. The LOS wind velocity is measured using only light frequency measurements by determining the frequency change between the transmitted and backscattered light. Accurate frequency measurement is much easier to do than intensity measurement. This is accomplished using coherent (heterodyne) detection, which translates the entire signal spectrum at 146 THz to the MHz range permitting data digitization by commercial-off-the-shelf analog-to-digital converters (ADCs). The conversion from frequency to LOS velocity is 1.026 (m/s)/MHz. Contextual information from the orbit, satellite, earth, and beam direction is used to calculate and remove spacecraft velocity and earth rotation velocity from the measurement. The OWP measurement concept is depicted in Figure 6.1.

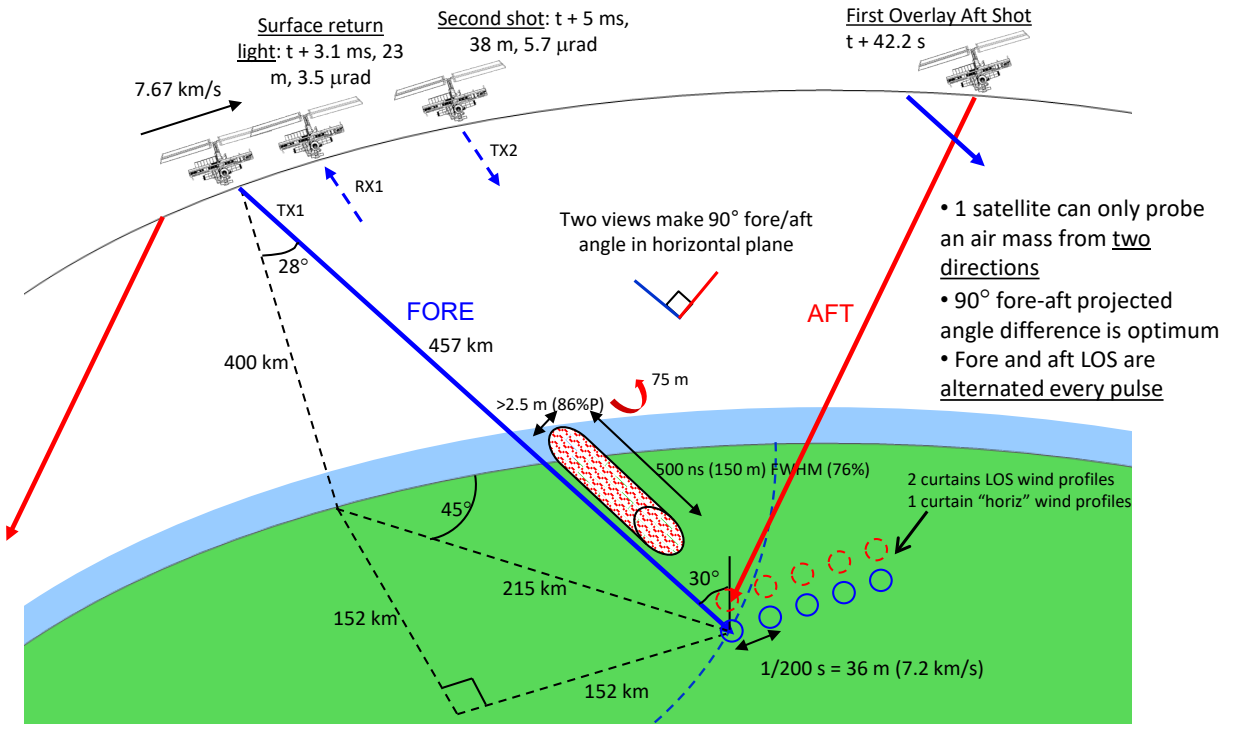

Figure 6.1: Example of the dual-LOS OWP orbit geometry and lidar pulse orientations from 400 km orbit with a 400 Hz laser rep rate, 30° off-nadir, and 2 LOS at 45° and 135° azimuth angles.

6.1. Geometry

Only a few of the 16,880 laser pulses over 42.2 seconds are depicted for clarity (~2.2 million shots per orbit). In actuality, the fore (drawn blue) and aft (drawn red) pulses transmit alternately every 2.5 ms in their respective LOS directions. The satellite and lidar are orbiting left to right at 7.7 km/s. The spacecraft is assumed to be 400 km above the earth ellipsoid where the average earth radius occurs (6,371,315 m). The difference between the ellipsoid and local earth radius is used in obtaining the wind altitudes and measurement nadir angle. The fore and aft laser shots both intersect the surface 152 km to the right of the ground track, and 152 km ahead or behind, respectively, the sub-satellite point. We model the laser's nadir angle at the surface to be 30 deg which requires the transmit nadir angle to be 28 deg. due to the modeled spherical earth and average earth radius. The beam intersect point at the earth surface moves left to right at 7.2 km/s. Each of the two LOS effectively has a laser pulse rate of 200 Hz so that the satellite will have moved 38 m, and the surface spot will have moved 36 m during each 5 ms LOS period. The beam's slant range to the surface is 457 km leading to a light round-trip time of 3.05 ms. During the round-trip time the satellite nadir angle, and therefore the uncorrected receiver axis, will nominally tip by 3.5 microradians. This nadir angle tip is compensated to obtain maximum carrier-to-noise ratio (CNR). The satellite forward motion of 23 m does not misalign the receiver axis, does not lower CNR, and does not require any compensation. The equal fore and aft distances from the ground track will cause the aft laser pulses to approximately coincide at the surface with the fore laser pulses, after a delay time of 42.2 s. At the equator, the earth rotation during 42.2 s will be 19.5 km, falling to zero as latitude goes to 90°. The two azimuth angles may be slightly modified to reduce this gap at the equator.

6.2. Measurement Location

The laser pulse's temporal intensity full width at half-maximum (FWHM) will be in the range of 200-500 ns. A 500-ns duration pulse will travel at the speed of light (c) with a spatial length of 150 m. However, the round-trip distance causes the lidar's instantaneous received signal at time t to come from only half the pulse length or 75 m located at

distance c*t/2. The beam's cross section exp(-2) intensity diameter with respect to the beam center intensity will be 2.5 m or greater, depending on the beam quality transmitted.

6.3. Range Gates

The received signal's time duration requiring capture depends on the minimum and maximum altitude to be processed. For example, the LOS signal duration from 30 km to the surface lasts 231 microseconds given the 34.6 km slant range. The conversion factor is 149.9 m/microsecond. Once digitized this signal is divided up into selectable-length range gates that are typically longer than the half-pulse duration lower limit. The range gate signals are each processed by an FFT into a periodogram (that is, the magnitude squared of the time signal's FFT). The selectable number of shot accumulations (shot averaging) is performed by adding these periodograms for each range gate. The range gate length determines both the vertical resolution and the frequency resolution of the LOS wind measurement. In practice, adaptive integration will be used where both the length of the range gates and the number of shots averaged may be variable with altitude and changed and reprocessed repeatedly depending on atmospheric conditions and science goals.

6.4. Data Digitization

The heterodyne detector output is amplified and captured by an ADC with a sampling rate sufficiently high to accommodate the highest design signal frequency. For example, a 500 MHz ADC sampling rate will yield a periodogram with a range of 250 MHz. This bandwidth easily accommodates a ±100 m/s horizontal velocity (±50 m/s LOS velocity or 97 MHz LOS frequency) capture range, with extra bandwidth for the signal bandwidth, any signal position jitter before correction, a guard band from DC to prevent aliasing, and/or higher wind speeds. As an example, consider a desired vertical resolution of 250 m which needs a LOS range gate length of 289 m for a range gate time duration of 1.9 microseconds. During this time the ADC will collect 963 signal samples. Before calculating the periodogram, the 963 signal samples must be zero padded to at least 1024 samples total or more (to a value of 2^n). If 1024 total samples, then each periodogram will output values at 1024 frequencies of which half are repeated numbers. The frequency precision (calculation spacing) of the periodogram is the inverse of the range gate total signal time of 1.9 microseconds. The periodogram will have a frequency precision of 0.49 MHz which equals a wind magnitude precision of 0.5 m/s. The independent calculated frequencies will range from 0 to 250 MHz for 512 independent channels. The shot averaged periodogram will ideally have the signal peak, in the case of 1 signal frequency bin only, higher than any of the noise peaks in the other 511 channels. If the signal peak occupies more than 1 periodogram channel, then a matched filter step will be used to estimate the signal peak and its frequency, and the number of noise channels will be correspondently less than 511.

6.5. Laser Pulse/Shot Averaging

The range gate length of 289 m and the >2.5 m beam footprint diameter define the range gate measurement volume for a single laser pulse (or "shot"). For laser shot averaging several periodograms are added for each range gate. This stretches the measurement volume in the along-track direction. To prevent the shot averaged signal spectrum from being widened by system frequency jitter, which degrades velocity accuracy, the periodograms must be added after alignment in frequency to each other. This frequency registration of the periodograms is accomplished by employing an outgoing frequency difference heterodyne detector, mixing the LO laser beam with a small portion of the transmitted beam. This is needed since the pulsed laser frequency is close to the LO or seed laser frequency, but different for each pulse, with MHz variations. If the periodograms are registered using only the 1024 range gate samples, the frequency alignment will have a precision of 0.5 m/s. To improve upon this precision, the 1024 samples are zero padded even more before the FFT. If zero padding is done to a total of 2048 samples, for example, then the periodogram registration will be accurate to 0.25 m/s. Although zero padding adds no new information, the wind measurement velocity precision may approach 0.25 m/s with sufficient shot averaging.

6.6. Wind Measurement Figures of Merit

By far the most common types of lidar use direct-detection, including CALIPSO and Aeolus, that measure backscattered light intensity. For this type of wind lidar, the figure of merit (FOM) is the wind accuracy standard deviation in m/s. However, the situation is much different for coherent-detection lidars. After shot averaging including the frequency registration of all the periodograms, the signal peak chosen in data processing to be the wind velocity peak may either be the wind signal peak or a noise peak in other periodogram frequency bins. If the chosen peak is from the wind, then the measurement will be highly accurate. If a noise peak is mistakenly chosen, the calculated wind will have no relationship to the true wind. We refer to a measurement as "good" or "bad" depending on this bifurcation. The probability of a "good" estimate (referred to below as "success rate") can decline from 95% to 5% in as little as one order of magnitude of CNR values. This is called the "probability of good cliff". Because of the "cliff" in "good" probability and the very slow change in wind measurement precision with CNR, the probability of "good" wind estimates becomes the primary FOM for coherent wind lidar measurements. The precision of the "good" wind estimates is always excellent except with very high wind turbulence or wind shear which broadens the signal spectrum.

6.7. Theoretical Definitions and Expressions for Lidar Signal, Carrier-to-Noise Ratio, Signal-to-Noise Ratio, and Detectivity SNR

The purpose of this section is to provide a theoretical background on lidar signal detection and to outline the dependencies of various lidar system parameters on the backscatter measured by the lidar. Such system and data processing parameters can be modulated for space-based instrument design to improve/degrade backscatter sensitivity (e.g. the minimum backscatter that could be measured by the lidar) which also impacts instrument cost/complexity and science data quality. Such parameters include satellite orbit height, telescope primary mirror size, and science data horizontal and vertical resolution.

Four important differences of coherent detection lidar compared to direct detection lidar are that: 1) the mixing of the signal light with the local oscillator (LO) light on the detector translates the 146 THz optical signal frequencies to MHz electronic frequencies for the total signal spectrum including phase to be digitized and further processed in a computer; 2) sufficient LO power on the signal detector enables near shot-noise-limited coherent detection which effectively eliminates all detection noise sources except the local oscillator (LO) shot noise on the detector; 3) the signal information consists of frequencies which are estimated in the frequency domain instead of the time domain eliminating noise in other frequency regions, and 4) the measurement is sensitive to the phase and phase matching of both LO and backscattered light, in addition to their intensities. A depiction of a frequency-registered and shot-averaged periodogram is shown in Figure 6.7.1, which is analogous to periodograms shown in Figure 3.4. The periodogram is calculated from signals collected over a temporal window of duration τ_w (1.9 microseconds in the above example) and typically the periodograms from multiple pulses and/or range gates are averaged prior to signal detection and frequency (velocity) estimation. The differences of coherent detection from direct detection leads to a simplification of the expression for noise and a more complex expression for the signal.

For coherent lidar there are two key quantities that characterize the signal level above the noise. The first of these is the narrowband carrier-to-noise ratio (CNR) which is defined in the periodogram as $CNR_n = \mu_s/\mu_n$, where μ_s is the mean height of the signal above the mean noise floor, μ_n. The second is the detectivity signal-to-noise ratio (SNR), SNR_d, which is defined in the periodogram as $SNR_d = \mu_s/\sigma_n$, where σ_n is the standard deviation of the noise floor fluctuations. These quantities are depicted in Figure 6.7.1. The detectivity SNR is the best indicator of being able to make a successful wind measurement.

Both the signal and the noise fluctuate with exponential statistics for individual measurements. By averaging over multiple statistically independent samples the noise and signal fluctuations become Gamma distributed which approaches the Gaussian distribution when the number of averages is large. The standard deviation of both the noise and signal are reduced as $\sigma_i = \mu_i/\sqrt{M_T}$ where M_T is the number of statistically independent samples in the measurement. We will describe CNR_n and SNR_d in more detail below. Further details may be found in Henderson et al. (2005).

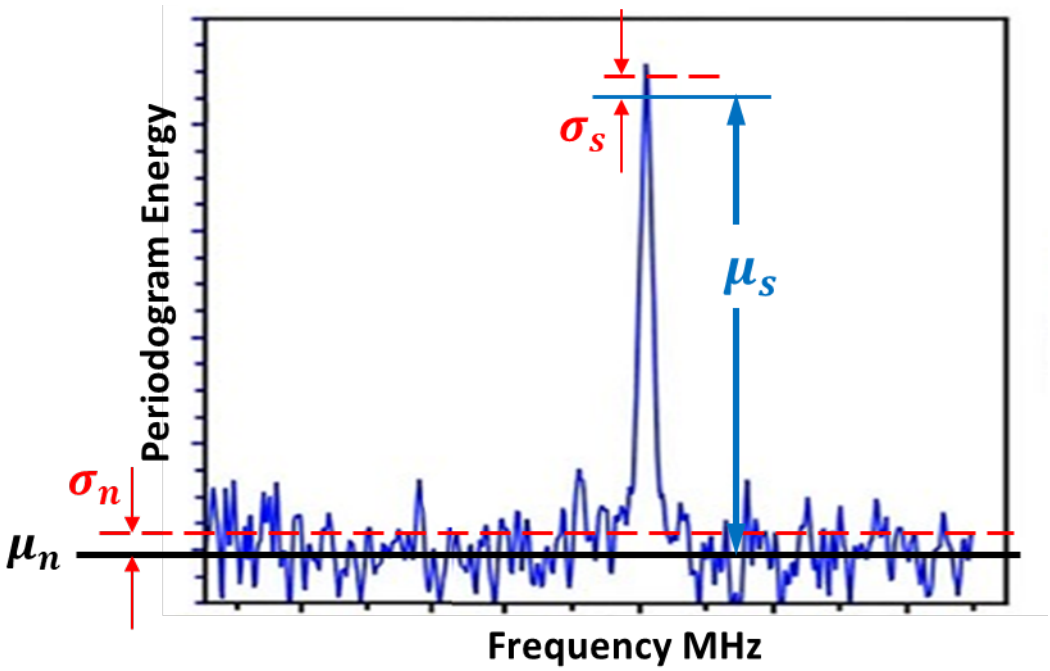

Figure 6.7.1: Example of a Shot-Averaged Periodogram that illustrates parameters used to derive SNR and CNR.

The mean backscattered optical signal power P_s (after averaging over speckle fluctuations) incident on the receiver telescope primary mirror follows the direct-detection lidar equation:

$$P_s(R) = \frac{\eta_{ot}\eta_{tt}E_l T^2(R) c\beta(R) A_r}{2R^2}, \quad Eq\ 1$$

where η_{ot} is the transmission efficiency of the transmit optical path, η_{tt} is the truncation efficiency of the Gaussian cross section transmit beam through the telescope, E_l is the transmit laser's pulse energy, , T^2 is the 2-way transmission to the backscattering target and back, c [unit in m/s] is the speed of light, β $[m^{-1}sr^{-1}]$ is the aerosol or cloud backscattering coefficient per atmospheric interaction length and per steradian at the receiver, A_r $[m^2]$ is the receiver area (for a circular aperture $A_r = \pi D^2/4$, with D [m] being the receiver diameter), and R is the distance to the backscattering target. The differences from direct detection do not change the key parameter dependences in Eq. (1). The signal is inversely proportional to the square of the range to target and is proportional to the square of the receiver diameter. The signal is linearly proportional to the pulse energy and aerosol or cloud backscatter coefficient. Atmospheric extinction lowers the signal on both transmit and on backscattering paths.

As the receiver diameter D is changed, the transmitted Gaussian beam size must be changed for maximum signal. The optimum size relationship for the typical lidar configuration is Gaussian beam exp(-2) intensity diameter should be 0.8 D. Larger transmit beams will suffer greater truncation of power at the telescope primary mirror, and smaller transmit beams will diffract more, creating larger far field patterns that have speckle patterns at the receiver that are too small leading to phase cancellation of the signal on the detector.

Pulsed coherent wind lidars typically transmit circular polarization and the receiver is designed for the opposite circular polarization signal. This is part of the overall transmit/receive (T/R) switch that protects the pulsed laser and signal detector from the very large interference from transmit light backscattering off transmit optical surfaces. The T/R switch ideally maximizes the backscattered signal from a hypothetical mirror in the far field and normal to the beam. Although we use the parameter β as a scalar variable in Eq. (1), it is more generally a 4 x 4 Mueller matrix that operates on the polarization Stokes vector of the transmitted beam to create the polarization Stokes vector of the backscattered beam. For a typical coherent wind lidar, the return signal depends on 4 of the 16 aerosol/cloud

Mueller matrix components, namely it is proportional to $0.5(\beta_{11} \pm \beta_{14} \mp \beta_{41} - \beta_{44})$ with the upper/lower signs for transmitting right/left circular polarization. Several aerosol backscatter Mueller matrix models have been proposed that depend on aerosol symmetry and depolarization assumptions. Direct detection depolarization (cross-polarization) lidars that transmit and receive linear polarization have a different dependence on the 16 matrix elements; hence will measure different backscatter coefficients if the matrix elements are large enough.
The fraction of the signal power on the receiver that is coherently detected P_{sc} is given by:

$$P_{sc}(R) = \eta_q \eta_{or} \eta_h(R) P_s(R) = \frac{\eta_{eo-} \eta_a(R) E_l T^2(R) c\beta(R) A_r}{2R^2}, \quad Eq\ 2$$

where:

- $\eta_{eo-} = \eta_{eo}/\eta_{sn} = \eta_q \eta_{or} \eta_{ot}$ is the electrooptic efficiency divided by the shot noise efficiency, with η_{eo} being the total electrooptic efficiency, η_{sn} being the shot noise efficiency of the coherent receiver which is the shot noise power divided by the total receiver noise power, η_{or} being the transmission efficiency of the receive optical path, and η_q being the quantum efficiency of the detector.
- $\eta_a = \eta_{tt} \eta_h$ is the antenna efficiency of the coherent lidar, with η_h being the heterodyne detection efficiency of the lidar which is a measure of the fraction of the signal power that is coherently matched to the single mode coherent receiver.

In general, the narrowband coherent detection CNR is defined as

$$CNR_n(R) = \eta_{sn} \frac{P_{sc}(R)}{h\nu B} = \frac{\eta_{eo} \eta_a(R) T^2(R) \beta(R) \lambda E_l A_r}{2hR^2 B}, \quad Eq\ 3$$

where the shot noise efficiency factor, η_{sn}, accounts for the fact that most coherent receivers are not fully shot noise limited, h is Planck's constant, $\nu = c/\lambda$ is the signal frequency, λ is the signal wavelength, and B is the noise equivalent bandwidth of the receiver. Most well-designed coherent detection lidar receivers have η_{sn} being between 0.9 and 0.98.

In summary, the optical power incident on the receiver telescope includes efficiency factors η_{ot} and η_{tt}, the power coherently matched to the single mode coherent receiver further includes $\eta_h(R)$, the coherently detected power further includes $\eta_q \eta_{or}$, and coherent detection CNR further includes η_{sn}, the laser's frequency ν, and the receiver bandwidth B. The product $h\nu$ is the energy per photon.

There are several combinations of atmospheric properties, lidar characteristics, and data processing parameters. These define many different conditions, and the equations diverge for different cases. For example, there are different regimes for the relative sizes of the pulse duration, the range gate duration, the amount of wind turbulence, the backscattered signal inverse bandwidth, and the receiver inverse bandwidth. The CNR is maximized when the receiver bandwidth is minimized to match the signal bandwidth. If the backscattered signal spectrum is Gaussian with standard deviation of σ_{fs}, the noise equivalent bandwidth of a receiver that optimally matches the signal bandwidth is given by $B_g = \sqrt{2\pi}\sigma_{fs}$. This is the noise equivalent bandwidth since a rectangular spectrum of height $\frac{1}{\sqrt{2\pi}\sigma_{fs}}$ and width of $\sqrt{2\pi}\sigma_{fs}$ has the same area as a normalized Gaussian with standard deviation of σ_{fs}, $g(f) = \frac{1}{\sqrt{2\pi}\sigma_{fs}} exp\left[\frac{1}{2}\left(\frac{f-\mu_f}{\sigma_{fs}}\right)^2\right]$.

For the usual case of a periodogram calculated using signal and noise in a temporal sampling window of duration τ_w, which defines the range gate, 1.9 microseconds in the example above, the CNR of the windowed signal is given by:

$$CNR_{nw}(R) = \frac{\mu_s}{\mu_n} = \frac{\eta_{eo} \eta_a(R) T^2(R) \beta(R) \lambda E_l A_r \tau_{cw}}{2hR^2}, \quad Eq\ 4$$

where τ_{cw} is the duration over which the complex amplitude of the windowed heterodyne signal is coherent, the

windowed signal coherence time. An analytic expression for τ_{cw} can be derived for the special case of a Gaussian signal spectrum and a rectangular window duration:

$$\tau_{cw} = \tau_{ci}\left\{\operatorname{erf}\left(\sqrt{\pi}\cdot\frac{\tau_w}{\tau_{ci}}\right) - \frac{1-e^{-\pi\left(\frac{\tau_w}{\tau_{ci}}\right)^2}}{\pi\cdot\frac{\tau_w}{\tau_{ci}}}\right\}. \quad Eq\ 5$$

τ_{cw} varies from the intrinsic coherence time of the window τ_w for short sampling window durations τ_w, to the intrinsic coherence time τ_{ci} of the unwindowed backscattered signal for long window durations. The mean noise μ_n may be measured in a separate experiment or from signal samples known to have no signal. It should be used to "whiten" or "flatten" the experimental mean noise curve vs. frequency. If the noise standard deviation differs across the periodogram spectrum, the value near the signal peak should be used.

The total diversity M_T, the number of statistically independent samples, in the LOS wind measurement is the product of the individual range gate diversity M_w, the number of range gates averaged M_r, and the number of laser pulses averaged M_p. The latter two diversities are selectable during signal processing and as they are increased, the vertical and horizontal resolutions, respectively, are degraded. The diversity of an individual range gate goes from the value 1 for short sampling window durations to the value τ_w/τ_{ci} for long windows. Analytic expressions for any window duration can be found for rectangular windows and a Gaussian signal spectrum, called the coherent diversity. The coherent diversity accurately defines the number of noise equivalent periodogram frequency bins that contain signal.

For a single shot (single pulse) and single range gate the noise floor of the periodogram consists of exponentially distributed noise with the standard deviation of the noise fluctuations equaling the mean value. If we assume that independent signal and noise samples from M_p pulses and M_r range gates are averaged, the noise floor then consists of gamma distributed noise with the standard deviation of the noise fluctuations being defined by $\sigma_n = \mu_n/\sqrt{M_pM_r}$. Similarly, signals from individual coherence times within single shots are exponentially distributed due to scattering from the randomly distributed aerosol particles in the atmosphere. Therefore, the standard deviation of the signal peak fluctuations also depends on the number of incoherent signals in the average, $\sigma_s = \mu_s/\sqrt{M_pM_r}$.
The detectivity SNR of the windowed signal in the periodogram is defined as:

$$SNR_{dw} = \frac{\mu_s}{\sigma_n} = \sqrt{M_pM_r}\frac{\mu_s}{\mu_n} = \sqrt{M_pM_r}CNR_{nw} = \sqrt{M_pM_r}\frac{\eta_{eo}\eta_a(R)T^2(R)\beta(R)\lambda E_l A_r\tau_{cw}}{2hR^2} \quad Eq\ 6$$

Solving Eq. (6) for the aerosol backscatter sensitivity yields:

$$\beta(R) = SNR_{dw}\frac{2hR^2}{\sqrt{M_pM_r}\eta_{eo}\eta_a(R)T^2(R)\lambda E_l A_r\tau_{cw}} \quad Eq.7$$

The backscatter sensitivity depends on many lidar, atmospheric, and data processing conditions. Parameters we further explore with our performance modeling in the following section are 1) range to the aerosol target R (i.e. satellite orbit height), 2) size of the telescope area A_r which is dependent on the receiver diameter D, 3) the number of independent samples used for wind retrieval M_p which is modulated by the lidar pulse repetition frequency (PRF) and spatial integration distance (horizontal resolution), and 4) the number of range gates averaged M_r (vertical resolution).

6.8. Wind Measurement Performance Computer Simulations

6.8.1. The NASA Langley Space-Based Coherent Wind Lidar Performance Simulation

The LaRC team has access to several independently developed wind lidar space mission performance computer simulations that have various ways to represent performance, but which have been shown to agree closely with each other. We show below in Figure 6.8.1 one of the ways to indicate wind measurement performance. The red

data points show aerosol backscatter at 2-µm wavelength (in units km^{-1} sr^{-1}) vs altitude for hypothetical lidar orbits across the globe, derived from a NASA GSFC Global Modeling and Assimilation Office (GMAO) GEOS-5 Nature Run (G5NR) (see description below). The yellow, black, and blue solid lines show the 10%, 50%, and 90% cumulative probability curves vs. altitude for all the calculated 2-µm aerosol backscatter. For example, at each altitude, half the calculated backscatter values are to the right of the black line.

We model the OWP Earth-orbiting coherent wind lidar concept depicted in Figure 6.1 with assumed parameters shown in the Figure 6.8.1.1 inset and discussed above. The mission orbit is 400 km, the fore and aft laser shots have a 30-deg nadir angle at the surface, the laser produces 60 mJ pulses at 400 Hz, and the two telescopes are each 60 cm clear aperture. Our simulations did not include clouds or wind shear but did include atmospheric transmission and wind turbulence vs. altitude. The 2-way atmospheric transmission fell from 100% at higher altitudes to a minimum of 72% at the surface, using a high atmospheric transmission window at 2.053 microns wavelength. The wind turbulence model began at the surface at 0.5 m/s and linearly increased to 2 m/s at 10 km. It remained at 2 m/s above 10 km. We assumed, after data processing iterations using all available contextual information, that the final search bandwidth for the horizontal wind peak was ±20 m/s. We assume a 90% success rate with picking the correct signal peak in our modeling. If we required a 100% success rate, then the amplitude of the signal peak in the periodogram would need to be larger, which requires greater lidar backscatter sensitivity. For this example, the vertical resolution is varied with increasing altitude from 250 m to 1,000 m. The simulation combines all the input values and uses an exhaustive and meticulous NASA-funded coherent wind lidar performance parameterization (Frehlich 2004). The performance parameterization utilized a Monte Carlo computer simulation to carefully simulate coherent wind lidar signals from atmospheric aerosols. The simulation included wind and aerosol backscatter fluctuations, wind shear and turbulence, shot averaging, wind velocity search range, number of digitized data points for each range gate, and Capon velocity estimation (Lottman and Frehlich 1997). Over 80,000 realizations of the wind field and velocity estimates were generated. The simulation results for the fraction of good wind estimates and the standard deviation error of the good estimates were fit to empirical model equations having up to seven fitting parameters. The two figures of merit were each calculated from two coefficients and other measurement parameters. The total of four coefficients were separated into two ranges of the number of independent samples per range gate, 0.25-2 and 2-32. This resulted in eight tables of the seven fitting parameters. The tables of fitting parameters covered 27 values of the probability of good wind estimates from 30% to 99.9999%. The 27 probabilities, two cases of number of independent samples result in 54 measurement conditions parameterized, each having a selectable value of the number of laser shots averaged.

The computer simulation utilizing the results of Frehlich (2004) does not directly utilize the analytic equations from Section 6.7. The parameterization is a separate method of characterizing performance. It includes many elements that are not treated in the simplified analytic equations presented above, and covers many other cases of parameter values. However, comparisons between the two methods show dependences on major parameters in agreement with each other. The backscatter sensitivity between the two methods is also in good agreement.

The green, magenta, and orange nearly vertical solid lines in Figure 6.8.1.1 show the simulation's calculated required aerosol backscatter vs. altitude to yield the specified 90% success rate for 15, 40, and 75 km horizontal resolution, respectively. The science parameter "horizontal resolution" is linearly related to the lidar performance input value of number of laser shots averaged. As expected, the 15 km resolution requires higher backscatter values than poorer resolutions. The science parameter "vertical resolution" is linearly related to the range gate length which also determines the number of photons received per gate and which affects the number of independent samples per gate. For each of these aerosol backscatter curves, called the Beta (90%) curves, there will be 90% good wind estimates at the curve's backscatter number. For higher backscatter to the right of the curves, the probability of good estimates will increase. For lower backscatter to the left of the curves, the probability of good estimates will decrease. For example, the green 15 km resolution curve will measure more than 90% of the atmosphere with 250 m vertical resolution up to the yellow 10% CDF curve at 1 km, then more than 50% of the atmosphere with 500 m vertical resolution up to the black 50% CDF curve at 3 km, and finally more than 10% of the atmosphere with 1000 m vertical resolution up to the blue 90% CDF curve at 16 km. Decreasing the horizontal resolution to 40 or 75 km covers correspondingly more of the atmosphere. In general, the required aerosol backscatter levels scale as the

square root of both horizontal and vertical resolutions, and linearly with the pulse energy and receiver area. It is important to acknowledge that the actual performance will fluctuate based on aerosol loading (seasonal variations, time of day, dust or smoke events, volcanic activity), cloud cover, and the statistical nature of heterodyne lidar signals. Thus the statistics cited above that are gleaned from Figure 6.8.1.1. are an oversimplification of measurement performance.

Coherent detection, with its signal spectrum translation from THz to MHz permits data to be digitized and data processing to be performed by computer on the entire signal spectrum. The data may be reprocessed numerous times with different resolution values to yield a final 3-D wind product. Degraded resolution values may be used when needed to make a successful wind measurement. Furthermore, vertically and horizontally adjacent successful wind measurements may be used to narrow the frequency range of the periodograms that are searched for the wind peak. Other contextual information may also permit a narrower search bandwidth. These steps will increase atmospheric coverage compared to the simulation results presented here.

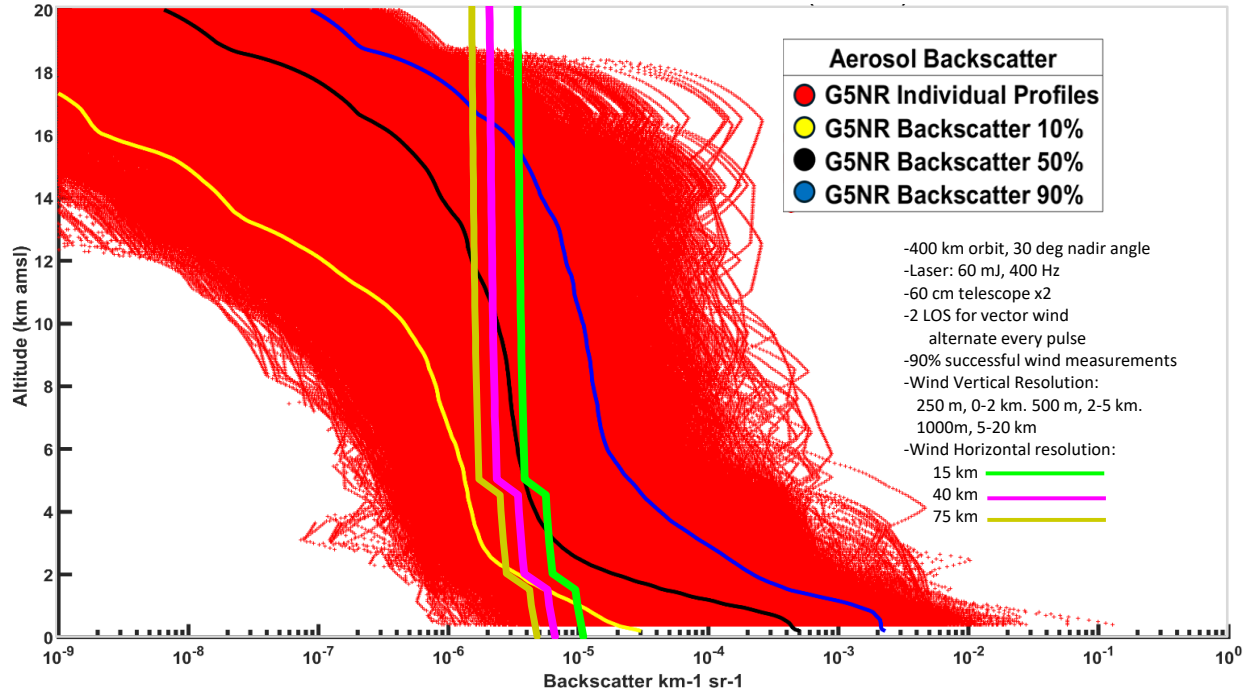

Figure 6.8.1.1: NASA GMAO GEOS-5 Nature Run (G5NR) 2 µm backscatter as a function of altitude (red) derived from one day of simulation on 15 July 2006. The 10th, 50th, and 90th percentiles of G5NR backscatter are plotted in yellow, black, and blue, respectively. OWP lidar aerosol backscatter sensitivity curves derived from 15, 40, and 75 km integrations with 3 different vertical integration depths specified in the legend are shown in green, magenta, and gold, respectively. Other parameters used within the performance simulation are included in the legend. The data used to generate this plot is available at NASA GMAO (2025).

6.8.2. The GMAO GEOS-5 Nature Run (G5NR)

The GMAO GEOS-5 Nature Run (G5NR) and a method to obtain aerosol optical properties such as aerosol backscatter from the model run are described by Castellanos et al. (2018). The output of the global, 7-km horizontal resolution, 72-level, 30-minute step size G5NR includes grid point profiles of atmospheric variables and five aerosol tracers–dust (5 bins), sulfate, sea salt (5 bins), black carbon and organic carbon -- which were created by coupling the GEOS-5 radiation code, realistic sources and emissions (anthropogenic, biogenic and volcanic) and the Goddard Chemistry, Aerosol, Radiation and Transport (GOCART) model. The G5NR covers the period June 2005 through May 2007. Following the method developed by Castellanos et al. at GMAO, aerosol optical properties including backscatter are computed in a method where aerosols are treated as external mixtures and properties are computed assuming

external emissions and Mie Theory code. These aerosol optical properties vary with DWL wavelengths, aerosol type and size, and humidity and are linked through a series of look up tables and include hygroscopic and hydrophobic binning; log normal size distributions for sulfate, black carbon (BC), and organic carbon (OC); and 5 size bins for sea salt and dust. Sulfate and hydrophilic OC/BC have prescribed growth factors based on humidity taken from previous studies, and sea salt growth factors are modeled after previous studies. For the figures in this report, we calculated aerosol backscatter and aerosol optical properties at 2-µm wavelength for every model grid point and level for one day (15 July 2006) of the G5NR using the method developed by Castellanos et al. (2018) and utilizing the same lookup tables used by Karpowicz and Prive (2024) for a 2-µm DWL simulation study. An example of a 2-µm backscatter curtain for one hour of simulated data from a hypothetical sun-synchronous orbit offshore of the U.S. East Coast is shown in Figure 6.8.2.1. According to Figure 6.8.1.1, OWP would be sensitive to backscatter between 10^{-5} and 10^{-6} km^{-1} sr^{-1} which would yield successful wind retrievals throughout the majority of the depth of this curtain, especially after 17:30 UTC where retrievals could be made at 75 km resolution up to 15-17.5 km.

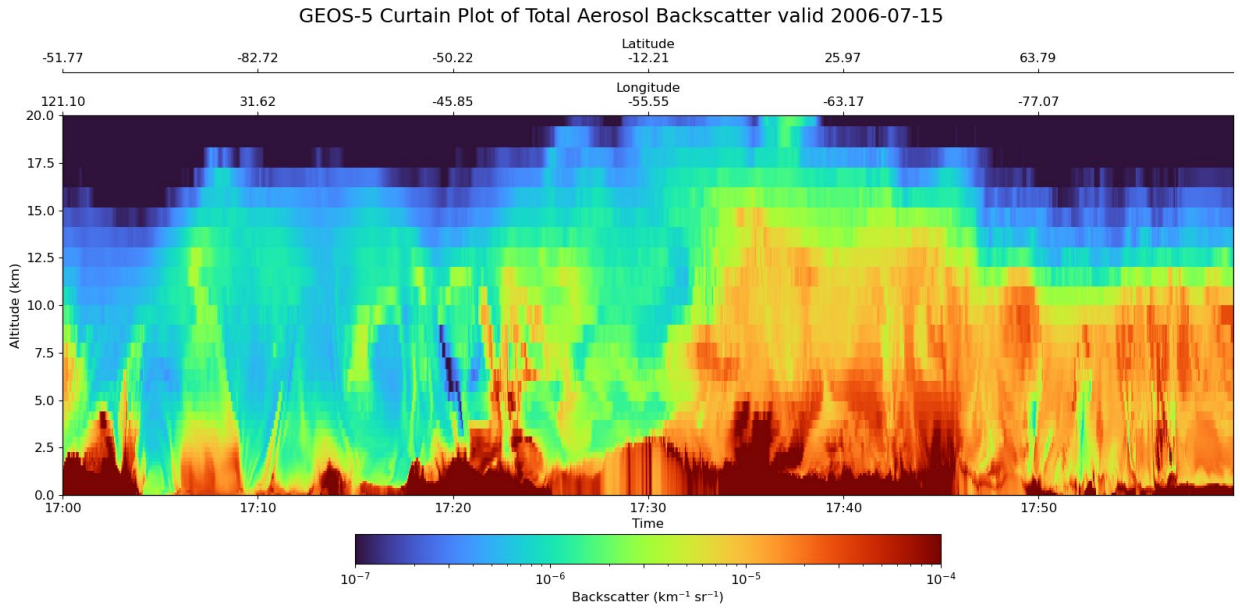

Figure 6.8.2.1: A 2-µm backscatter curtain simulated from a hypothetical sun-synchronous orbit from the NASA GMAO G5NR for one hour of data at 17 UTC on 15 July 2006. G5NR data is available from NASA GMAO (2025).

The relationship between the vertical coverage of successful wind retrieval, and spatial resolution and changes in the lidar instrument/mission parameters is not easily seen in Figure 6.8.1.1 above due to the number of plotted aerosol backscatter points in red. To better depict aerosol backscatter variability with height, single altitude histograms of the G5NR backscatter values were generated and shown in Figure 6.8.2.2. The histogram horizontal axes are the base 10 log of the backscatter values (-5 here equates to 10^{-5} on the x-axis in Figure 6.8.1.1). The histograms show altitudes of 0.5, 5, 10 and 15 km, and they reveal narrowly peaked Gamma distributions. This means that design operation near these narrow peaks will experience large degradation or improvement with changes in resolution and lidar parameters.

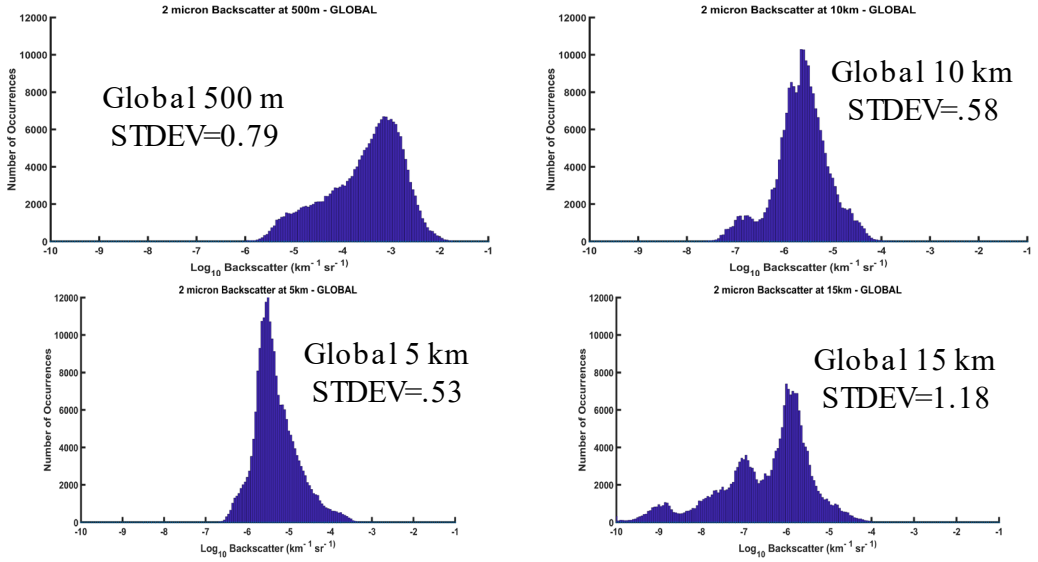

Figure 6.8.2.2: Aerosol backscatter histograms of G5NR backscatter values for altitude slices of Figure 6.8.1.1. Number of occurrences from 0 to 12000 vs. Log_{10} aerosol backscatter km^{-1} sr^{-1} from -10 to -1.

Pulse Energy (mJ)	PRF (Hz)	Pulse Duration (ns)	Wavelength (nm)	Vertical Resolution (m)	Horizontal Resolution (km)	Velocity Error (m/s)	Relative SNR (dB)	NOHD (m)
800	400	100	1064	30	3	0.42	0.00	3580000
60	400	200	2053	30	3	0.63	-10.87	0
60	400	200	2053	300	3	0.42	-4.71	0
60	400	200	2053	300	10	0.41	-2.03	0

Table 6.8.2.1: Maximum altitude, velocity error, and relative SNR estimates for an instrument with 60cm telescope aperture and orbiting at 300km. Relative SNR is compared to the estimated signal attainable with 800mJ, 30m vertical resolution, and 3 km horizontal resolution.

To optimize the design of a spaceborne heterodyne wind lidar, extensive simulations were performed, varying key system parameters. Table 6.8.2.1 presents a subset of these parameter set simulations and their impact on performance metrics. This table is not exhaustive but showcases the sensitivity of relative Signal-to-Noise Ratio (SNR) and Nominal Ocular Hazard Distance (NOHD) to changes in vertical and horizontal resolution. Coherent detection pulsed lidar does not permit spreading of the transmit beam, making eye safe operating wavelengths (NOHD=0) mandatory, negating the possibility of flying an 800 mJ laser. Note that LOS velocity error remains excellent for all cases, and the OWP-like wind lidar 300 meter vertical resolution and 10 km spatial resolution that both exceed NOAA's maximum measurement requirement (Table 1.1), would have 2 dB (~37%) lower sensitivity than the extremely high powered laser with extremely high resolution.

The slant range squared (R^2) term in the CNR and SNR equations (Eq. 4 and 6 in Section 6.7) is a parameter that notably affects performance. The maximum measurement altitude for a given spatial resolution can be improved by flying at a lower orbit (see Figure 6.8.2.3). Flying at 200 km orbit ensures a much higher percentage of good wind measurements, but achieving a lengthy mission lifetime at such a low orbit altitude is costly and challenging. A 400 km orbit enables a mission lasting several years and at least 10% success rate up to 16 km.

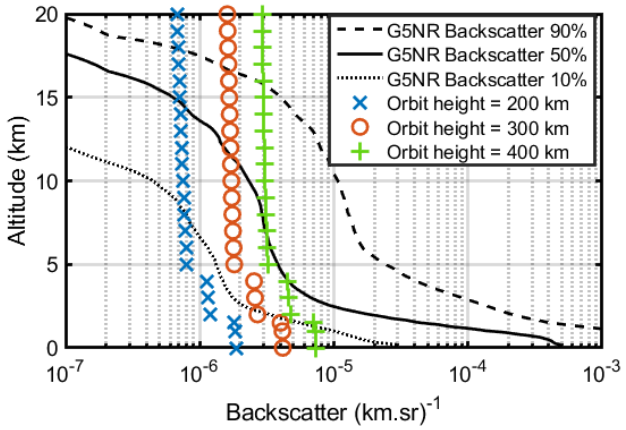

Figure 6.8.2.3: Modeled backscatter sensitivity for 200, 300, and 400 km orbits. E = 60 mJ. D = 0.6 m, τp = 200 ns, PRF = 200 Hz, horizontal resolution = 40 km, vertical resolution = 0.25, 0.5, and 1 km for 0-2 km, 2-5 km, and >5 km altitudes, respectively. (Green crosses have the same settings as the magenta curve in Figure 6.8.1.1).

Increasing the telescope diameter will expand backscatter sensitivity and the vertical depth of successful wind measurements. Doubling the telescope diameter increases receiver area by 4 and improves backscatter sensitivity by 4x or 6 dB. Wind measurements can be achieved up to a 20 km altitude if a 1.5-m telescope is used (see Figure 6.8.2.4). However, to accommodate two telescopes on a satellite for wind vector measurements, a 0.6-m telescope is being baselined for OWP. Manufacturing a 0.6-m telescope with the stringent requirements imposed by heterodyne detection is more cost effective. Another result of larger telescopes is a stricter requirement for correcting the pulse round-trip time-of-flight nadir tipping of the satellite. For constant wind measurement performance, the product of the telescope diameter and the maximum uncorrected tipping angle must remain constant, that is, the angle correction requirement is inversely proportional to the diameter.

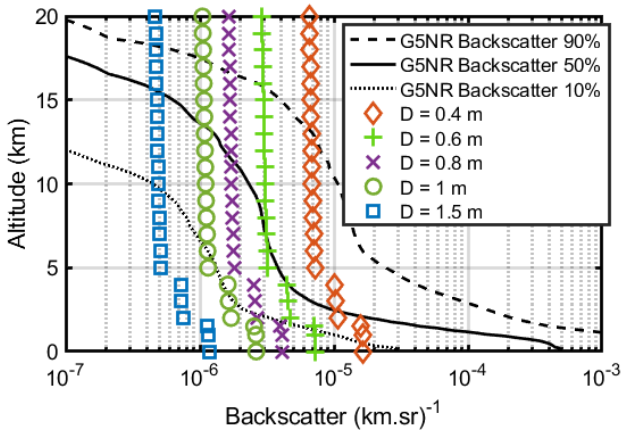

Figure 6.8.2.4: Modeled backscatter sensitivity for 0.4, 0.6, 0.8, 1, and 1.5 m. E = 60 mJ. Orbit height = 400 km, τ_p = 200 ns, PRF = 200 Hz, horizontal resolution = 40 km, vertical resolution = 0.25, 0.5, and 1 km for 0-2 km, 2-5 km, and >5 km altitudes, respectively. (Green crosses have the same settings as the magenta curve in Figure 6.8.1.1)

Laser pulse interference can occur if a pulse is transmitted while the backscattered signal from an earlier pulse is being received by the lidar. The easiest solution to avoid pulse interference is to complete the signal reception of a pulse before transmitting the next pulse. To avoid pulse interference, the maximum Pulse Repetition Frequency (PRF) (or pulse rate) of the 60 mJ transmitter is baselined at 400 Hz PRF. However, the transmitter is shared between the two lines of sight which reduces the effective pulse-averaging effect to 200 Hz. Each of the two telescopes transmits a pulse at 200 Hz. The maximum pulse rate without causing pulse interference is approximately 325 Hz for

our assumed geometry. While operating at 200 Hz slightly reduces the operational range, the wind vector measurement is a unique data product that can have a larger impact on reducing the errors of weather prediction models. Figure 6.8.2.5 compares backscatter sensitivity for four values of pulse rate.

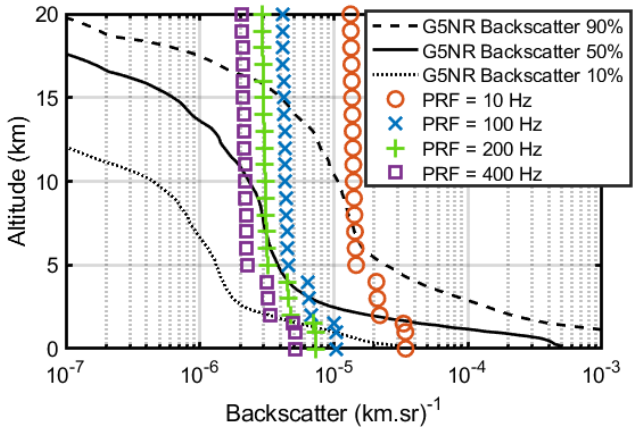

Figure 6.8.2.5: Modeled backscatter sensitivity for 10, 100, 200, and 400 Hz PRF. E = 60 mJ. Orbit height = 400 km, τp = 200 ns, horizontal resolution = 40 km, vertical resolution = 0.25, 0.5, and 1 km for 0-2 km, 2-5 km, and >5 km altitudes, respectively. (Green crosses have the same settings as the magenta curve in Figure 6.8.1.1)

Eq. 7 also shows a relationship between backscatter sensitivity and laser pulse energy (E_l). Figure 6.8.2.6 compares sensitivity for five values of pulse energy. The compact transceiver developed by Beyond Photonics that is being considered for OWP has been shown to generate up to 75 mJ of pulse energy, with the potential for greater energy with additional laser pump power (Henderson et al. 2025). We have benchmarked OWP with 60 mJ energy (green crosses) to be conservative and allow for margin as the transceiver operates for several years in space and potentially declines in performance.

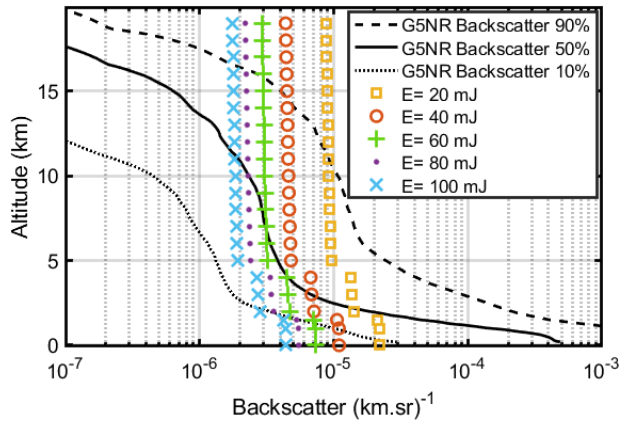

Figure 6.8.2.6: Modeled backscatter sensitivity for E = 20, 40, 60, 80, and 100 mJ. Orbit height = 400 km, τp = 200 ns, horizontal resolution = 40 km, vertical resolution = 0.25, 0.5, and 1 km for 0-2 km, 2-5 km, and >5 km altitudes, respectively. (Green crosses have the same settings as the magenta curve in Figure 6.8.1.1)

While a lidar with a 1.5-m telescope, 100 mJ pulse energy, 400 Hz PRF, and 200 km orbit height will have far superior performance than the OWP mission concept baselined in this report, we believe the parameters selected for OWP will yield a mission that has significant impact on weather prediction models while also enabling a cost effective, multi-year operation. This assessment is evaluated and quantified in the following section by combining the DWL instrument performance with a NWP model.

6.8.3. Simpson Weather Associates Doppler Lidar Simulation Model (DLSM)

Next, we present measurement performance using a second computer simulation developed at partner Simpson Weather Associates (SWA). To facilitate the evaluation of space mission concepts involving a Doppler Wind Lidar, they developed a Doppler Lidar Simulation Model (DLSM, SWA 2025). The DLSM is designed to be coupled with an NWP model to generate a realistic set of wind observations that can be used to characterize the vertical and horizontal data coverage and accuracy for a given lidar configuration, and the potential impact these observations may have on the predictive skill of NWP models. The DLSM has been used for several decades to conduct Observing System Simulation Experiments (OSSEs) and to perform system trade studies to define optimal instrument configurations. It was developed using the European Centre for Medium-Range Weather Forecasts (ECMWF) T511 nature run (NR). The main NR is a 13-month forecast using cycle 30r1 of ECMWF's Integrated Forecasting System (IFS) with T511 horizontal resolution (40 km) and 91 levels in the vertical; the output is saved every 3 hours. The initial condition is the operational analysis on 12 UTC on 1 May 2005 and the NR ends at 00 UTC on 1 June 2006. The simulations shown below used the original atmospheric variables including winds, temperature, relative-humidity, geopotential height, and pressure from the T511 nature run (35 km resolution). The aerosols and clouds are from the NASA GMAO G5NR run at a coarse 0.5° resolution (~55 km), for the same day and time as T511. Backscatter sensitivity and SNR is based on parameterizations of Frehlich and colleagues described in the previous Section 6.8.2. More information about the DLSM can be found in SWA (2025).

One way of summarizing the vertical distribution of successful DWL wind observations is the DLSM performance plot, a vertically stacked histogram of horizontally projected observational wind speed uncertainty σ_V derived from the calculated line of sight speed. Vertical resolution of the analysis is 1 km. The green and yellow color bars express the global % of all observation attempts, made in each layer, that met various bracket values of σ_V. The σ_V estimates include the effects of aerosols, sample scale turbulence, opaque clouds, and cirrus clouds. For instance, the dark green segment represents LOS wind retrievals under conditions that have high backscatter values, are mostly cloud free and exhibit weak wind variability. In these cases, the σ_V (RMSD) <1 m/s is primarily determined by the lidar system design and platform stability. The yellow ($2 < \sigma_V < 3$ m/s) bar segment can be interpreted as a consequence of dwell cases where partially cloudy conditions result in only a subset of the full set of shots and range gates available to participate in the averaging of the Nature Run derived wind turbulence; or the attenuated backscatter within the integration volume is close to the Beta (90%) value for the lidar system allowing a "white noise" contribution to the σ_V calculation depending upon the width of the signal search window. In the latter case, our simulations limit the "white noise" contribution to 10% given the use of Beta (90%) as a filter threshold for any wind product. The simulation run time is one day and follows a simulated sun-synchronous satellite orbit for about 16 orbits of earth. The 400 km orbit is assumed to be sun-synchronous with an inclination angle of 97°. Figure 6.8.3.1 shows the 15 km horizontal resolution case, following the horizontal backscatter sensitivity values of Figure 6.8.1.1, and is the strictest case. The horizontally projected velocity error never exceeds 3 m/s, meaning that the LOS wind error never exceeds 1.5 m/s. Successful observations at these resolutions occur for about half the measurement attempts up to about 11 km, and then decrease above that. The hatched areas represent the frequency of cloud returns and their wind measurements.

Figure 6.8.3.2 below duplicates Figure 6.8.3.1 but with a horizontal resolution of 40 km. The 50% success rate increases to about 14 km, and below that altitude the success rate is much better. Once again excellent wind accuracy is maintained, a key feature of coherent detection and frequency measurement. Figure 6.8.3.3 below shows the case of 72 km horizontal resolution. The measurement success rate is 80-90% up to about 13 km, and then tapers off up to 19 km. Note that even if pulse energy and/or telescope aperture were dramatically increased, there would still be measurement dropouts due to clouds. This shows the great importance of including clouds in performance simulations of any proposed wind lidar. Figure 6.8.3.4 below shows the test case of 72 km horizontal resolution with the 60 mJ laser pulse increased by 1667x to 100 J to clearly show the continued blockage by thick clouds (double cross hatching). However, the thick clouds do provide accurate cloud top winds with known altitudes.

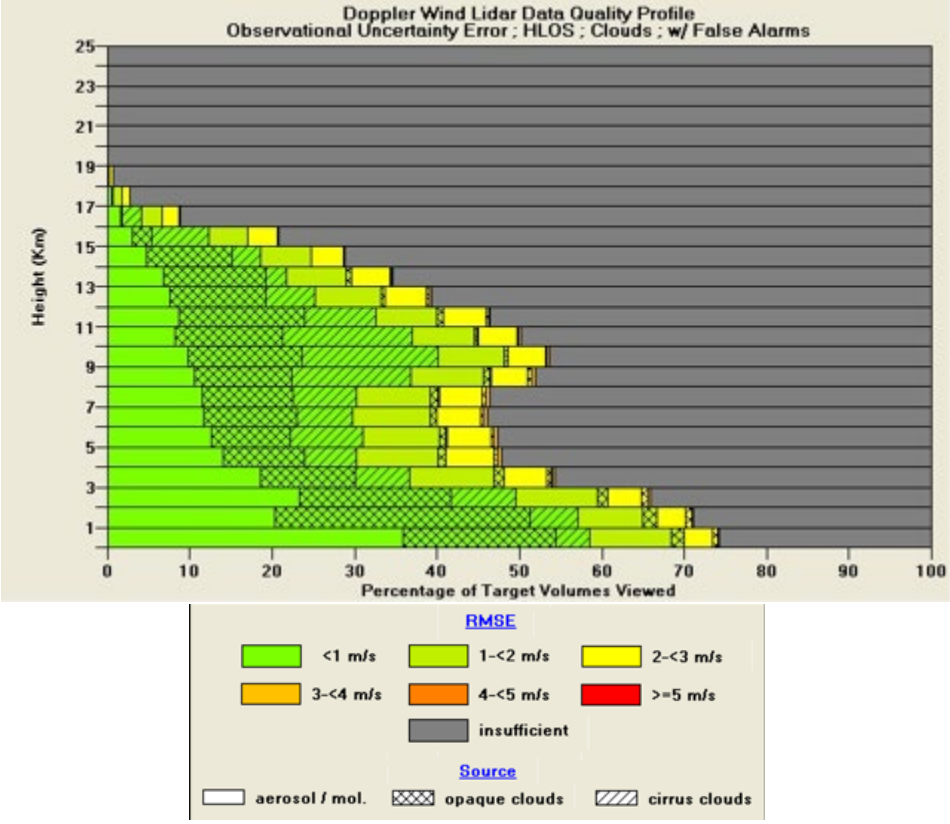

Figure 6.8.3.1: Wind measurement performance derived from the DLSM. Mission parameters follow Figure 6.8.1.1 and horizontal resolution is 15 km (2.2 secs shot integration).

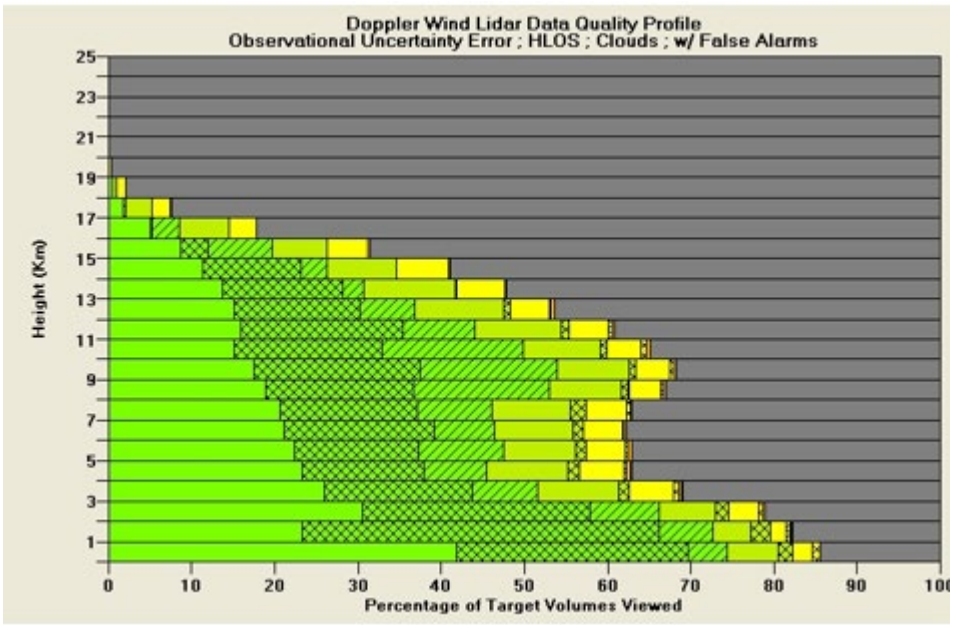

Figure 6.8.3.2: Same as Figure 6.8.3.1 but 40 km horizontal resolution (5.5 secs).

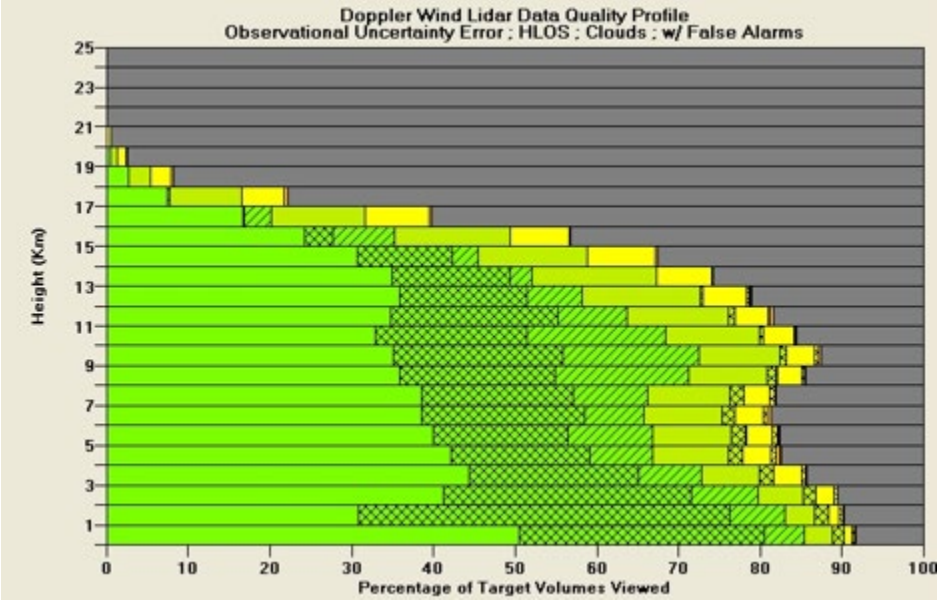

Figure 6.8.3.3: Same as Figure 6.8.3.1 but 72 km horizontal resolution (10 secs).

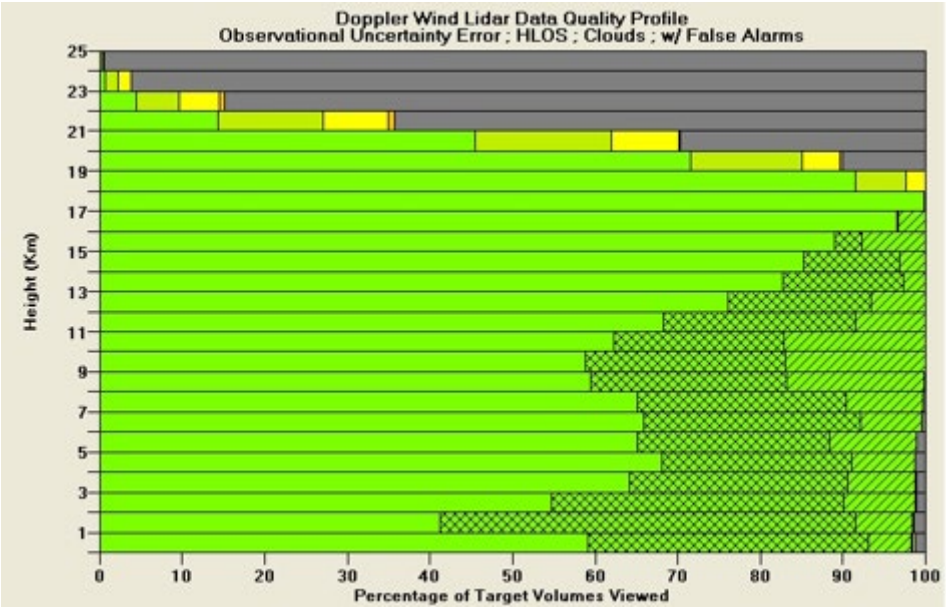

Figure 6.8.3.4: Same as Figure 6.8.3.3 but with 100 J pulse energy rather than 0.06 J (60 mJ).

7. Summary and Path to Space

This report provides a description of Aerosol Wind Profiler (AWP) technology and data processing methods, and a summary of AWP airborne data collected in support of the NOAA Joint Venture Program "Measuring the Atmospheric Wind profile (3-D Winds): Call for Studies and Field Measurement Campaigns for NOAA/NESDIS" Broad Agency Announcement (BAA, NOAA NESDIS 2022). This project sought to 1) demonstrate AWP wind measurement capability from a broad spectrum of weather regimes and aerosol conditions, 2) demonstrate how AWP data compares with NOAA NWP model and GOES AMV wind estimates, and 3) estimate how an AWP-like wind lidar would have performed from space. During the Fall 2024 NOAA 3-D Wind Demonstration (based in Hampton, VA) and WH^2yMSIE/APEX (based in central CA) campaigns which extended from 18 September to 15 November, AWP generated laser pulses at a 2.0592 µm near-IR wavelength, with ~40 mJ per pulse and 200 Hz repetition rate. AWP

flew aboard the NASA LaRC Gulfstream-3 aircraft, which offered a 6-hour maximum endurance and 41 kft altitude limit. AWP observed the atmosphere with two LOS and 6 sec dwell time per LOS in its most common scanning mode. Two LOS operation mimics what would be done from a satellite, and provides wind vector observations with ~1.6 km horizontal spacing between profiles and 66-132 meter vertical spacing between altitude bins. Nearly 100 hours of data were collected by AWP data during these campaigns. Many flights featured long, straight flight segments with flight altitude above 11 km that sampled a variety of aerosol, cloud, and wind patterns necessary for addressing project objectives 1) and 2). A few flights during WH^2yMSIE/APEX were confined to a small region to study cloud and planetary boundary layer processes, at a lower flight altitude than most flights. Only flight data relevant for addressing the project objectives listed above were delivered to NOAA, which spanned ~74 hours. When combined with the lesser-quality AWP ecoDemonstrator dataset (see Sections 4 and 5.1), ~125 hours of AWP data was delivered, which greatly exceeded the 60 hours initially proposed for the project.

AWP demonstrated the ability to detect a wide range of aerosol backscatter conditions, with aerosol signal detection that met or exceeded detection from a current state-of-the-art aerosol profiling lidar, the LaRC High Altitude Lidar Observatory (HALO). Flights were focused over the Eastern and Western U.S, but two transit flights between Hampton, VA and central CA sampled conditions over the Central U.S and Rocky Mountain regions. A wide variety of weather regimes and aerosol/cloud conditions important for weather analysis and prediction such as jet streams, low- and high-pressure systems, a tropical cyclone, dry continental, mid-latitude marine, and tropical airmasses, and many other phenomena were sampled. AWP retrieved winds with 55-100% success rate between the aircraft and surface on average. The highest success rates were in the upper troposphere and lower stratosphere, and in the PBL. The lowest success rate was in the altitude layer from 4-8 km where aerosol backscatter was typically weakest. AWP demonstrated the capability to profile through thin to moderately opaque clouds, and its high rep rate penetrated through breaks in small clouds to reach the PBL and surface. Dense aerosol layers were present in the stratosphere during several flights, which was not expected based on the observed weather regimes and model forecasts. Data processing incorporating longer temporal integration per LOS (up to 15 seconds) improved sensitivity to thin aerosol, resulting in improved vertical coverage of successful wind retrieval compared to 6 sec integrations commonly used during other flights.

AWP demonstrated excellent agreement with AVAPS dropsonde profiles, which allows AWP to be used to validate other wind observations and model predictions. AWP featured negligible bias (~0.05 m/s) and small uncertainty (~0.92 m/s) based on statistics derived from 10,052 AWP altitude bins closely co-located with dropsonde measurements. This exceeded the performance achieved by LaRC wind lidars during previous NASA airborne campaigns. AWP was used to quantify the accuracy of the NOAA GFS global NWP model and the HRRR regional NWP model, and AMVs derived from GOES-16 and -18 image sequences. Both HRRR and GFS demonstrated a near linear increase in deviation from AWP measurements with increased forecast lead time. Differences between AWP and the NOAA model initial analyses were typically along sharp wind gradients, indicating a slight misplacement of a wind pattern in the models. GOES visible AMVs had the best overall agreement with AWP, but wind speeds measured from visible channel cloud tracking in this channel were likely lower than other GOES channels because they are limited to a layer 0-3 km above the surface, making statistics between channels a bit challenging to compare and interpret. AMVs derived from 6.2 µm cloudy WV radiances performed best when analyzed as a function of percent difference from AWP wind speed, which normalized for differences in measured wind speeds from the various GOES channels. Cloud tracking from visible and IR window channel had similar normalized difference from AWP. AMVs from clear-sky WV gradients in three GOES WV absorption channels (6.2, 6.9, and 7.3 µm) exhibited a weaker overall agreement with AWP, which may be due to height assignment challenges given that WV radiances emanate over a deeper atmospheric layer than the typically shallow layer near cloud top measured from other channels. The project requested and was granted many 1-minute GOES Mesoscale Domain Sector (MDS) scan periods across the flight domains. AMVs derived from the MDS data were slightly more precise on average than AMVs derived from 5-min CONUS or 10-min Full Disk scans. AWP data could be used in the future to further improve and validate AMV retrieval using methods such as Dense Optical Flow, as had previously been done with DAWN airborne wind lidar data (Apke et al. 2022).

Lidar system performance modeling was completed to simulate the expected performance and the frequency

of successful wind retrieval as a function of altitude for a spaceborne Doppler wind lidar mission concept called the Orbital Wind Profiler (OWP) to address project objective 3), leveraging decades of experience within the project team. OWP is expected to feature a 60 mJ and 400 Hz laser transceiver with a 2 line-of-sight (LOS) viewing perspective (equating to 200 Hz per LOS) to achieve wind vector observations, a dual 60 cm telescope architecture, and a 400 km orbit altitude. Modeling is based on a combination of 1) 2 µm wavelength aerosol backscatter distribution derived from a NASA GMAO GEOS-5 Nature Run (G5NR), 2) aerosols and clouds derived from an ECMWF T511 Nature Run, 3) a previous NASA-funded wind lidar performance parameterization, and 4) the Simpson Weather Associates Doppler Lidar Simulation Model (DLSM). Our simulations show median aerosol backscatter sensitivity between 10^{-5} and 10^{-6} km^{-1} sr^{-1}, which exceeded the median G5NR backscatter aggregated across the globe with lidar pulse integration durations ranging from 15 km (0-2 km altitude layer), 40 km (2-5 km), and 75 km (5+ km). Instrument trade analysis indicated that OWP operating with a very low 200 km orbit and/or a very large telescope (1.5 m primary mirror diameter) would be sensitive to extremely weak aerosol backscatter (< 10^{-6} km^{-1} sr^{-1}) that would result in a very high wind retrieval success rate. But such an instrument would have either very short mission lifetime due to the low orbit or would be complex, large, and costly to build. This trade analysis guided us to baseline instrument parameters listed above to achieve a reasonable cost and complexity. The DLSM indicated successful retrievals for 30-85% of all profiling opportunities throughout the troposphere and lower stratosphere (surface to 16 km altitude) at NOAA's Mid-Point (40 km) spatial resolution requirement, with the greatest frequency occurring within and near to the Planetary Boundary Layer (PBL, 0-2 km altitude) and lowest frequency in the lower stratosphere. Above 16 km, the rate of successful retrieval steadily decreased up to a 20 km altitude where aerosol backscatter diminished. The retrieval success rate increased (decreased) by about 20% when 75 km (15 km) pulse integrations are employed. This performance from OWP would be a significant improvement over Aeolus-1 Mie channel wind retrieval success rate.

An addendum to this report indicates a clear and tangible path to space for OWP Doppler wind lidar technology. In summary, recent NASA-funded technology developments at Beyond Photonics have led to an 8x reduction in laser transmitter volume, a 10x reduction in laser cavity length, and 60+ W reduction in power requirement compared to the AWP airborne system laser (Diamond et al. 2024; Henderson et al. 2025). This laser transmitter would generate 60+ mJ pulse energy, a 400 Hz rep rate, and high beam quality (< 1.1 M^2), performance that is sufficient for space-based operation. We are baselining a 3-year mission duration for an initial OWP spaceflight demonstration. Analysis indicates that this compact pulsed laser module, coupled with a Thulium pump laser analogous to the Fibertek unit described in Section 2.4 (Engin et al. 2020), and other required instrument components could be accommodated on an ESPA Grande SmallSat. We currently estimate an instrument mass of 200 kg and a power requirement of 600 W. This size, weight and power could be accommodated by many SmallSats currently on the market (NASA Spacecraft Platforms, 2025). Flying aboard a SmallSat has the potential to greatly reduce satellite bus and launch costs over larger satellite buses. As shown in Figure 6.1, the two 60-cm telescopes would be oriented orthogonally to each other, with beam direction switching done every other pulse. OWP would measure a continuous curtain of wind vectors and 2 µm aerosol backscatter with variable horizontal (10-100 km) and vertical spacing (0.25 – 1 km) that can be adaptively modulated within ground-segment processing depending on backscatter return, and aerosol and cloud conditions. In the event that two telescopes could not be accommodated, we would collect single LOS wind speed measurements that were found to be impactful to NWP models based on experience with Aeolus-1 data. A study recently conducted by Aerospace Corporation indicates that all OWP data collected per day could be reliably downlinked to a network of ground stations and stored within cloud computing, allowing wind retrieval products to be distributed to the community 30-90 minutes after initial data collection. A 2-µm lidar has never been flown in space and would provide valuable aerosol backscatter data to complement measurements from the ESA EarthCare 355, 532, and 1064 nm or EUMETSAT Aeolus-2 355 nm data, as well as any other lidar(s) that may fly within the NASA Atmosphere Observing System (AOS) constellation. Winds could be successfully measured for ≥ 50% of all profile opportunities within the free troposphere and lower stratosphere, and ~85% of opportunities in the PBL, with an estimated precision better than 3 m/s. This would greatly exceed the success rate from the Aeolus-1 Mie channel, and therefore is likely to have significant positive impact on global weather forecast models like Aeolus-1 Mie data (Rennie 2023). OWP would be a highly capable wind lidar system that can be built, launched, and operated with an

affordable cost. After an initial OWP demonstration mission that would incur non-recurring engineering costs associated with instrument design, environmental testing, and algorithm development (among others), follow-on OWP units could be built much more affordably, enabling the potential for a wind lidar constellation. Such a constellation would greatly complement and improve LEO or GEO imager- and sounder-based wind measurements that are expected to be more common in the 2030's, through improved height assignment and bias correction (e.g. Nguyen et al. 2024).

For OWP to become a reality, technology maturation is needed to space-qualify (including thermal vacuum and vibration test) the laser transceiver, lidar electronics, and auxiliary lasers (the SWIFT LO and MO units). We would also need to evaluate options to compensate for spacecraft movement in the ~4 ms time period between lidar pulse transmission from 400 km altitude and atmospheric backscatter return to the satellite, commonly referred to as "lag-angle". The baseline compensation approach is an actively controlled beam steering mechanism with pitch/yaw mirror control using voice-coil actuators, and an alternative passive approach is being explored at NASA LaRC. We would also need to complete a dual LOS telescope design, and to design and build instrument Engineering Test Unit(s). Efforts are also required to develop onboard data collection, signal processing, data compression methods, and a data downlink scheme for low-latency processing. While these activities are challenging and require a funded mission to execute them, we view these as standard engineering and do not currently envision any obstacles to their completion during Phases-A and -B of a space mission.

8. References

Apke, J. M., Y. Noh, and K. Bedka, 2022: Comparison of Optical Flow Derivation Techniques for Retrieving Tropospheric Winds from Satellite Image Sequences. *J. Atmos. Oceanic Technol.*, **39**, 2005–2021, https://doi.org/10.1175/JTECH-D-22-0057.1.

Atlas, R., and Coauthors, 2015*:* Observing system simulation experiments (OSSEs) to evaluate the potential impact of an optical autocovariance wind lidar (OAWL) on numerical weather prediction. *J. Atmos. Oceanic Technol.*, ***32***, 1593–1613, https://doi.org/10.1175/JTECH-D-15-0038.1

Baker, W. E., and Co-authors, 2014: Lidar-Measured Wind Profiles: The Missing Link in the Global Observing System. *Bull. Amer. Meteor. Soc.*, **95**, 543–564, https://doi.org/10.1175/BAMS-D-12-00164.1.

Baron, P., S. Ishii, K. Okamoto, K. Gamo, K. Mizutani, C. Takahashi, T. Itabe, T. Iwasaki, T. Kubota, T. Maki, R. Oki, S. Ochiai, D. Sakaizawa, M. Satoh, Y. Satoh, T. Y. Tanaka, and M. Yasui, 2017: Feasibility study for future spaceborne coherent Doppler wind lidar. Part 2: Measurement simulation algorithms and retrieval error characterization. *J. Meteor. Soc. Japan*, **95**, 319-342. https://doi.org/10.2151/jmsj.2017-018

Bedka, K. M., Nehrir, A. R., Kavaya, M., Barton-Grimley, R., Beaubien, M., Carroll, B., Collins, J., Cooney, J., Emmitt, G. D., Greco, S., Kooi, S., Lee, T., Liu, Z., Rodier, S., and Skofronick-Jackson, G., 2021: "Airborne lidar observations of wind, water vapor, and aerosol profiles during the NASA Aeolus calibration and validation (Cal/Val) test flight campaign," Atmos. Meas. Tech., 14 (6), 4305–4334, (2021) https://doi.org/10.5194/amt-14-4305-2021

Bedka, K., Marketon, J., Henderson, S., Kavaya, M., 2024: AWP: NASA's Aerosol Wind Profiler Coherent Doppler Wind Lidar. In: Singh, U.N., Tzeremes, G., Refaat, T.F., Ribes Pleguezuelo, P. (eds) Space-based Lidar Remote Sensing Techniques and Emerging Technologies. LIDAR 2023. Springer Aerospace Technology. Springer, Cham. https://doi.org/10.1007/978-3-031-53618-2_3

Carroll, B. J., Nehrir, A. R., Kooi, S. A., Collins, J. E., Barton-Grimley, R. A., Notari, A., Harper, D. B., and Lee, J., 2002: Differential absorption lidar measurements of water vapor by the High Altitude Lidar Observatory (HALO): retrieval framework and first results, Atmos. Meas. Tech., 15, 605–626, https://doi.org/10.5194/amt-15-605-2022

Castellanos, P., Da Silva, A.M., Darmenov, A.S., Buchard, V., Govindaraju, R.C., Ciren, P. and Kondragunta, S., 2018. A geostationary instrument simulator for aerosol observing system simulation experiments. Atmosphere, 10(1), https://www.mdpi.com/2073-4433/10/1/2

Diamond, J., P. A. Fernandez, and S. Henderson, 2024: Compact High-Power 2-micron Transmitter for Coherent

Lidar Applications. 2024 Coherent Laser Radar Conference, Landshut, Germany (June 23-28, 2024). https://beyondphotonics.com/wp-content/themes/beyondphotonics/img/CLRC_2024-Compact_Transmitter.pdf (CLRC 2024 website is down)

DuVivier, A. K., J. J. Cassano, S. Greco, and G. D. Emmitt, 2017: A Case Study of Observed and Modeled Barrier Flow in the Denmark Strait in May 2015. Mon. Wea. Rev., 145, 2385–2404, https://doi.org/10.1175/MWR-D-16-0386.1.

Engin, D., W. Rudd, M. Storm, M. Long, V. Litvinovitch, L. Holley, and N. W. Sawruk, 2020: High Power Thulium Fiber Laser Systems for Airborne and Spaceborne Missions," Proc. SPIE 11261, Components and Packaging for Laser Systems VI (2020); https://doi.org/10.1117/12.2547955

ESA, 2023: https://www.esa.int/Applications/Observing_the_Earth/FutureEO/Aeolus/Trailblazing_Aeolus_mission_winding_down#:~:text=On%2030%20April%202023%2C%20all,end%2Dof%2Dlife%20activities

Eyre, J.R., Bell, W., Cotton, J., English, S.J., Forsythe, M., Healy, S.B., and Co-authors, 2022: Assimilation of satellite data in numerical weather prediction. Part II: Recent years. *Q J R Meteorol Soc*, 521–556. Available from: https://doi.org/10.1002/qj.4228

Feng, C. and Pu, Z., 2023: The impacts of assimilating Aeolus horizontal line-of-sight winds on numerical predictions of Hurricane Ida (2021) and a mesoscale convective system over the Atlantic Ocean, Atmos. Meas. Tech., 16, 2691–2708, https://doi.org/10.5194/amt-16-2691-2023

Feng, C. Z. Pu, A. R. Nehrir, K. M. Bedka, and J. Doyle, 2025: The Impacts of Assimilating DAWN and HALO Observations on Numerical Simulations of Tropical Convective Systems Associated with African Easterly Waves During NASA's CPEX-AW and CPEX-CV. Provisionally Accepted to *Monthly Weather Review*

Flament, T., Trapon, D., Lacour, A., Dabas, A., Ehlers, F., and Huber, D., 2021: Aeolus L2A aerosol optical properties product: standard correct algorithm and Mie correct algorithm, Atmos. Meas. Tech., 14, 7851–7871, https://doi.org/10.5194/amt-14-7851-2021

Folger, K. and Weissmann, M., 2014: Height correction of atmospheric motion vectors using satellite lidar observations from CALIPSO. *Journal of Applied Meteorology and Climatology*, **53**, 1809–1819. https://doi.org/10.1175/JAMC-D-13-0337.1.

Frehlich, R. G., 2004: Velocity Error for Coherent Doppler Lidar with Pulse Accumulation. *J. Atmos. and Oceanic Technol.,* 21, 905. DOI: https://doi.org/10.1175/JTECH1596

Frehlich, R. G., 1996: Simulation of Coherent Doppler Lidar Performance in the Weak-Signal Regime. *J. Atmos. Oceanic Technol.*, **13**, 646–658, https://doi.org/10.1175/1520-0426(1996)013<0646:SOCDLP>2.0.CO;2.

Frehlich, R. G. and M. J. Yadlowsky, 1994: Performance of Mean-Frequency Estimators for Doppler Radar and Lidar," J. Atmos. and Oceanic Technology 11, 1217. https://doi.org/10.1175/1520-0426(1994)011<1217:POMFEF>2.0.CO;2

Garrett, K., Liu, H., Ide, K., Hoffman, R.N. and Lukens, K.E., 2022: Optimization and impact assessment of Aeolus HLOS wind assimilation in NOAA's global forecast system. *Quarterly Journal of the Royal Meteorological Society*, **148**, 2703–2716. https://doi.org/10.1002/qj.4331

Google, 2025: https://console.cloud.google.com/marketplace/product/noaa-public/goes?pli=1&inv=1&invt=AboFRA&project=rock-logic-242020

Greco, S.; Emmitt, G.D.; DuVivier, A.; Hines, K.; Kavaya, M., 2020a: Polar Winds: Airborne Doppler Wind Lidar Missions in the Arctic for Atmospheric Observations and Numerical Model Comparisons. Atmosphere, 11, 1141. https://doi.org/10.3390/atmos11111141

Greco, S.; G. D. Emmitt, M. Garstang, and M. Kavaya, 2020b: Doppler Aerosol WiNd (DAWN) Lidar during CPEX 2017: Instrument Performance and Data Utility. Remote Sens. 2020, 12, 2951. https://doi.org/10.3390/rs12182951

Hair, J. W., C. A. Hostetler, A. L. Cook, D. B. Harper, R. A. Ferrare, T. L. Mack, W. Welch, L. R. Izquierdo, and F. E.

Hovis, 2008: Airborne High Spectral Resolution Lidar for profiling aerosol optical properties," Appl. Opt. 47, 6734-6752. https://doi.org/10.1364/AO.47.006734

Henderson, S., P. Gatt, D. Rees, and R. M. Huffaker, 2005: Wind Lidar. Book Chapter 7 in *Laser Remote Sensing (1st ed.)*. CRC Press. Fujii, T., & Fukuchi, T. (Editors). https://doi.org/10.1201/9781420030754

Henderson, S. W. and C. P. Hale, 2017: Fast widely-tunable single-frequency 2-micron laser for remote-sensing applications, Proc. SPIE 10406, Lidar Remote Sensing for Environmental Monitoring 2017, 104060C (30 August 2017); https://doi.org/10.1117/12.2277089

Henderson, S. W., M. Kavaya, J. Yu, P. Kratovil, C. Hale, J. Diamond, D. Bruns, J. Marketon, D. Emmitt, Z. Liu, and K. Bedka, 2022: Advanced Eyesafe Lidar for Atmospheric Wind Measurements. 2022 Coherent Laser Radar Conference, Big Sky, Montana (June 26 – July 1, 2022). https://beyondphotonics.com/wp-content/themes/beyondphotonics/img/CLRC_2022-Wind-SP_Tech.pdf

Henderson, S. W., J. Diamond, P. Alvarez, and P. Kratovil, 2025: Technology Advances for Airborne and Space-Based Coherent Lidar for Atmospheric Wind Measurements. 2025 NOAA-NASA. College Park, Maryland. (February 19-20 2025) https://beyondphotonics.com/wp-content/themes/beyondphotonics/img/3D_Winds_2025-Coherent_Lidar_Tech_Advances.pdf

Hristova-Veleva, S., Zhang, S. Q., Turk, F. J., Haddad, Z. S., and Sawaya, R. C., 2021: Assimilation of DAWN Doppler wind lidar data during the 2017 Convective Processes Experiment (CPEX): impact on precipitation and flow structure, *Atmos. Meas. Tech.,* 14, 3333–3350, https://doi.org/10.5194/amt-14-3333-2021

Ishii, S., P. Baron, M. Aoki, K. Mizutani, M. Yasui, S. Ochiai, A. Sato, Y. Satoh, T. Kubota, D. Sakaizawa, R. Oki, K. Okamoto, T. Ishibashi, T. Y. Tanaka, T. T. Sekiyama, T. Maki, K. Yamashita, T. Nishizawa, M. Satoh, and T. Iwasaki, 2017: Feasibility study for future space-borne coherent Doppler wind lidar, Part 1: Instrumental overview for global wind profile observation. *J. Meteor. Soc. Japan*, **95**, 301-317. https://doi.org/10.2151/jmsj.2017-017

Joshi, A. M, and S. Datta, 2020: Space flight of 2.2-micron wavelength extended InGaAs optical receivers to the International Space Station," Proc. SPIE 11388, Image Sensing Technologies: Materials, Devices, Systems, and Applications VII, 1138808 (20 May 2020); https://doi.org/10.1117/12.2558755

Karpowicz, B. M., and N. C. Privé, 2024: Using the GEOS-5 Nature Run to Simulate 2053-nm Coherent Doppler Wind Lidar Observations. *J. Atmos. Oceanic Technol.*, **41**, 665–683, https://doi.org/10.1175/JTECH-D-23-0117.1.

Kavaya, M. J., J. Y. Beyon, G. J. Koch, M. Petros, P. J. Petzar, U. N. Singh, B. C. Trieu, and J. Yu, 2014: The Doppler Aerosol Wind (DAWN) Airborne, Wind-Profiling Coherent-Detection Lidar System: Overview and Preliminary Flight Results. *J. Atmos. Oceanic Technol.*, **31**, 826–842, https://doi.org/10.1175/JTECH-D-12-00274.1

Kiriakidis, P., Gkikas, A., Papangelis, G., Christoudias, T., Kushta, J., Proestakis, E., Kampouri, A., Marinou, E., Drakaki, E., Benedetti, A., Rennie, M., Retscher, C., Straume, A. G., Dandocsi, A., Sciare, J., and Amiridis, V., 2023: The impact of using assimilated Aeolus wind data on regional WRF-Chem dust simulations, Atmos. Chem. Phys., 23, 4391–4417, https://doi.org/10.5194/acp-23-4391-2023

Lottman, B. T., and R. G. Frehlich, 1997: Evaluation of Doppler radar velocity estimators, *Radio Sci.,* 32(2), 677–686, https://doi.org/10.1029/96RS03329

Lux, O., Lemmerz, C., Weiler, F., Marksteiner, U., Witschas, B., Rahm, S., Geiß, A., Schäfler, A., and Reitebuch, O., 2022: Retrieval improvements for the ALADIN Airborne Demonstrator in support of the Aeolus wind product validation, *Atmos. Meas. Tech*., 15, 1303–1331, https://doi.org/10.5194/amt-15-1303-2022

Ma, Z., L. P. Riishøjgaard, M. Masutani, J. S. Woollen, and G. D. Emmitt, 2015: Impact of Different Satellite Wind Lidar Telescope Configurations on NCEP GFS Forecast Skill in Observing System Simulation Experiments. *J. Atmos. Oceanic Technol.*, **32**, 478–495, https://doi.org/10.1175/JTECH-D-14-00057.1.

Marseille, G. J. , Stoffelen , A. and Barkmeijer , J. 2007: A cycled sensi-tivity observing system experiment on simulated Doppler wind li-dar data during the 1999 Christmas storm “Martin” . *Tellus 60A*, DOI: https://doi.org/10.1111/j.1600-0870.2007.00290.x

Marseille, G. J., Stoffelen, A., & Barkmeijer, J., 2008: Impact assessment of prospective spaceborne Doppler wind

lidar observation scenarios. *Tellus A: Dynamic Meteorology and Oceanography*, *60*(2), 234–248. https://doi.org/10.1111/j.1600-0870.2007.00289.x

Martin, C. and Suhr, I., 2021: NCAR/EOL Atmospheric Sounding Processing ENvironment (ASPEN) software. Version 3.4.5. Available Online: https://www.eol.ucar.edu/content/aspen, Accessed on: Mar. 9, 2021.

Martin, A., Weissmann, M. and Cress, A., 2023: Impact of assimilating Aeolus observations in the global model ICON: A global statistical overview. *Quarterly Journal of the Royal Meteorological Society*, 149(756), 2962–2979. Available from: https://doi.org/10.1002/qj.4541

NASA, 2023: https://www.nasa.gov/centers-and-facilities/armstrong/nasa-partners-explore-sustainable-fuels-effects-on-aircraft-contrails/

NASA GMAO 2025: https://g5nr.nccs.nasa.gov/data/OBS/A-CCP/SS450/LevelC2/Y2006/M07/D15/

NASA Spacecraft Platforms, 2025: https://www.nasa.gov/smallsat-institute/sst-soa/platforms/#2.2.1

National Academies of Sciences, Engineering, and Medicine. 2018. *Thriving on Our Changing Planet: A Decadal Strategy for Earth Observation from Space*. Washington, DC: The National Academies Press. https://doi.org/10.17226/24938

Nguyen, H., Posselt, D., Yanovsky, I., Wu, L., and Hristova-Veleva, S., 2024: Atmospheric motion vector (AMV) error characterization and bias correction by leveraging independent lidar data: a simulation using an observing system simulation experiment (OSSE) and optical flow AMVs, Atmos. Meas. Tech., 17, 3103–3119, https://doi.org/10.5194/amt-17-3103-2024

NOAA NESDIS, 2018: The NOAA Satellite Observing System Architecture (NSOSA) Study, NOAA-NESDIS-2018-0053-0002 (May 31, 2018); https://www.regulations.gov/document/NOAA-NESDIS-2018-0053-0002

NOAA NESDIS, 2022: Broad Agency Announcement: Measuring the Atmospheric Wind profile (3D Winds): Call for Studies and Field Measurement Campaigns for NOAA/NESDIS; https://sam.gov/opp/058f74a44553411d9f50417a315e745f/view

NOAA NCEI, 2022: ETOPO 2022 15 Arc-Second Global Relief Model. NOAA National Centers for Environmental Information. DOI: 10.25921/fd45-gt74.

Nowottnick, E. P., and Coauthors, 2024: Dust, Convection, Winds, and Waves: The 2022 NASA CPEX-CV Campaign. Bull. Amer. Meteor. Soc., 105, E2097–E2125, https://doi.org/10.1175/BAMS-D-23-0201.1.

NSF NCAR - Earth Observing Laboratory, 1993: NCAR Airborne Vertical Atmospheric Profiling System (AVAPS). NSF NCAR - Earth Observing Laboratory. https://doi.org/10.5065/D66W9848

Okamoto, K., Ishibashi, T., Ishii, S., Baron, P., Gamo, K., Tanaka, T. Y., Yamashita, K., and Kubota, T., 2018: Feasibility Study for Future Space-Borne Coherent Doppler Wind Lidar, Part 3: Impact Assessment Using Sensitivity Observing System Simulation Experiments, J. Meteorol. Soc. Jpn., 96, 179–199, https://doi.org/10.2151/jmsj.2018-024

Ouyed, A., Smith, N., Zeng, X., Galarneau, T. Jr., Su, H., & Dixon, R. D., 2023: Global three-dimensional water vapor feature-tracking for horizontal winds using hyperspectral infrared sounder data from overlapped tracks of two satellites. *Geophysical Research Letters*, 50, e2022GL101830. https://doi.org/10.1029/2022GL101830

Rennie, M, 2023: A consolidated assessment of the impact of Aeolus winds in NWP at ECMWF. 2023 Aeolus Science Conference. Rhodes, Greece, 24 May 2023. Available online at: https://www.dropbox.com/s/ps1y18kpvv219cj/1.%20ECMWF_NWP_impact_Aeol_winds_Rennie_Rhodes_sci_conf.pdf?dl=0

Riishojgaard, L. P., Z. Ma, M. Masutani, J. S. Woollen, G. D. Emmitt, S. A. Wood, and S. Greco, 2012*:* Observation system simulation experiments for a global wind observing sounder. *Geophys. Res. Lett.*, ***39***, L17805, doi:10.1029/2012GL051814.

RP Photonics, 2025: https://www.rp-photonics.com/optical_heterodyne_detection.html

Sakaeda, N., and Coauthors, 2024: Synoptic Influences on the Diurnal Cycle of Rainfall over Western Puerto Rico. *Mon. Wea. Rev.*, **152**, 2341–2359, https://doi.org/10.1175/MWR-D-24-0035.1.

Singh, U. N., B. M. Walsh, J. Yu, M. Petros, M. J. Kavaya, T. F. Refaat, and N. P. Barnes, 2015: Twenty years of Tm:Ho:YLF and LuLiF laser development for global wind and carbon dioxide active remote sensing," Opt. Mater. Express 5, 827-837

SWA, 2025: https://swa.com/images/LidarSpaceBased/TheDopplerLidarSimulationModel.pdf

Straume-Lindner, A.G., and Co-authors: 2021: ESA'S Wind Mission Aeolus - Overview, Status and Outlook, *2021 IEEE International Geoscience and Remote Sensing Symposium IGARSS*, Brussels, Belgium, 2021, pp. 755-758, doi: 10.1109/IGARSS47720.2021.9554007. https://ieeexplore.ieee.org/document/9554007

Teixeira, J., J. R. Piepmeier, A. R. Nehrir, C. O. Ao, S. S. Chen, C. A. Clayson, A. M. Fridlind, M. Lebsock, W. McCarty, H. Salmun, J. A. Santanello, D. D. Turner, Z. Wang, and X. Zeng, 2021: Toward a Global Planetary Boundary Layer Observing System: The NASA PBL Incubation Study Team Report. NASA PBL Incubation Study Team. 134 pp. Available online at: https://smd-cms.nasa.gov/wp-content/uploads/2023/05/NASA_PBL_Incubation_Final_Report_2.pdf

Velden, C. S., and K. M. Bedka, 2009: Identifying the Uncertainty in Determining Satellite-Derived Atmospheric Motion Vector Height Attribution. *J. Appl. Meteor. Climatol.*, **48**, 450–463, https://doi.org/10.1175/2008JAMC1957.1

Weiler, F., Rennie, M., Kanitz, T., Isaksen, L., Checa, E., de Kloe, J., Okunde, N., and Reitebuch, O., 2021: Correction of wind bias for the lidar on board Aeolus using telescope temperatures, Atmos. Meas. Tech., 14, 7167–7185, https://doi.org/10.5194/amt-14-7167-2021

Witschas, B., Lemmerz, C., Geiß, A., Lux, O., Marksteiner, U., Rahm, S., Reitebuch, O., Schäfler, A., and Weiler, F., 2022: Validation of the Aeolus L2B wind product with airborne wind lidar measurements in the polar North Atlantic region and in the tropics, Atmos. Meas. Tech., 15, 7049–7070, https://doi.org/10.5194/amt-15-7049-2022

Yu, J., B. C. Trieu, E. A. Modlin, U. N. Singh, and M. J. Kavaya, S. Chen, Y. Bai, and P. J. Petzar, 2006: 1 J /pulse Q-switched 2 μm solid-state laser," Opt. Lett. 31(4), 462-464 (2006) https://doi.org/10.1364/OL.31.000462

Yu, J., J. Lee, T.-H. Wong, L. Petway, A. Traore, S. Chen, J. Marketon, M. Kavaya, S. Henderson, P. Kratovil, C. Hale, J. Diamond, D. Bruns, N. Vanasse, D. D'Epagnier, 2022: Efficient Ho:LuLiF MOPA laser transmitter for space pathfinder coherent wind lidar," Invited Paper, 2022 Coherent Laser Lidar Conference, Big Sky, MT (June 26 – July 1, 2022) Available online at: https://ntrs.nasa.gov/api/citations/20220008811/downloads/Yu%20CLRC-2022-summary.pdf (CLRC 2022 website is down).

Zeng, X., and Co-Authors, 2024: Vientos—A New Satellite Mission Concept for 3D Wind Measurements by Combining Passive Water Vapor Sounders with Doppler Wind Lidar. *Bull. Amer. Meteor. Soc.*, 105, E357–E369, https://doi.org/10.1175/BAMS-D-22-0283.1

9. Acronyms and Abbreviations

AA – Automatic-Alignment
AAC – Automatic Alignment Controller
ADC – Analog-to-Digital Converter
ALADIN - Atmospheric LAser Doppler INstrument
AMV – Atmospheric Motion Vector
AOM – Acousto-Optic Modulator
APEX – Active Passive PBL Profiling Experiment (APEX)
AVAPS - Airborne Vertical Atmospheric Profiling System
AWP – Aerosol Wind Profiler (LaRC)
BAA – Broad Agency Announcement
BP – Beyond Photonics
BPLO – Back-Propagating Local Oscillator
Cal/Val – Calibration and Validation
CALIPSO – Cloud-Aerosol Lidar and Infrared Pathfinder Satellite Observation (CALIPSO)
CDF – Cumulative Distribution Function
CDWL – Coherent Doppler Wind Lidar
CFC – Carbon Fiber Composite
CNR – Carrier-to-Noise Ratio
CNR – Carrier-to-Noise Ratio
CW – Continuous Wave
DAWN – Doppler Aerosol WiNd (lidar) (LaRC)
DEEVA - Data Evaluation, Exploitation, and Value

Assessment team (NOAA)
DIAL – Differential Absorption Lidar
DLSM – Doppler Lidar Simulation Model (Simpson Weather Associates)
ECMWF – European Center for Medium Range Weather Forecasting
EF – Exposed Facility (JEM)
ESA – European Space Agency
ESD – Earth Science Division (NASA SMD)
ESTO – Earth Science Technology Office (NASA ESD)
ETOPO – Earth TOPOgraphy
FFT – Fast Fourier Transform
FIRMS - Fire Information for Resource Management System (NASA)
FOM – Figure Of Merit
FOV – Field Of View
FWHM – Full Width at Half Maximum
G-3 – Gulfstream-3 (NASA LaRC)
G5NR – GEOS Version 5 Nature Run
GEO - Geostationary
GEOS – Goddard Earth Observing System
GFS – Global Forecast System
GMAO – Global Modeling and Assimilation Office (GSFC)
GOES – Geostationary Operational Environmental Satellite
GPS – Global Positioning System
GSFC – Goddard Space Flight Center
GWOS – Global Wind Observing System
HALO – High Altitude Lidar Observatory
HPM – High-Power Module
HRRR – High Resolution Rapid Refresh model (NOAA)
HSRL – High Spectral Resolution Lidar
HYSPLIT - HYbrid Single-Particle Lagrangian Integrated Trajectory
IFOV – Instantaneous Field-of-View
IF – Intermediate Frequency
IFS – Integrated Forecast System (ECMWF)
INS – Inertial Navigation System
ISS – International Space Station
JEM – Japanese Experiment Module (ISS)
LaRC – Langley Research Center (NASA)
LCM – Laser Control Module
LEM – Local Electronics Module
LEO – Low-Earth Orbit
LLF – LuLiF
LO – Local Oscillator (CW laser)
LOS – Line-Of-Sight
LPM – Low-Power Module
MO – Master Oscillator (CW laser, seed laser)
MODIS – MODerate resolution Imaging Spectrometer
NASA – National Aeronautics & Space Administration
NCEP – National Center for Environmental Prediction
NESDIS – National Envionmental Satellite, Data, and Information Service
NOAA – National Oceanic & Atmospheric Administration
NR – Nature Run
NSOSA – NOAA Satellite Observing System Architecture
NWP – Numerical Weather Prediction
OAWL – Optical Auto-covariance Wind Lidar
OSC - Oscillator
OSE – Observing System Experiment
OSEE – Optically Stimulated Electron Emission
OSSE – Observing System Simulation Experiment
OWP – Orbital Wind Profiler (LaRC)
PAN - Polyacrylonitrile
PBL – Planetary Boundary Layer
PRF – Pulse Repetition Frequency (Laser Pulse Rate)
PZT - Piezoelectric Transducer or lead (Pb) Zirconate Titanate
QC – Quality Control
RMS – Root (of the) Mean (of the) Squares
RMSD – Root (of the) Mean (of the) Squares Difference
SBIR – Small Business Innovative Research
SEM/EDS - Scanning Electron Microscopy/Energy Dispersive X-ray Spectroscopy
SEM/WDS – Scanning Electron Microscopy/ Wavelength Dispersive Spectrometer (also called EPM)
SM – Seed Mirror
SMD – Science Mission Directorate (NASA)
SNR – Signal-to-Noise Ratio
SP – Space Pathfinder
SWA – Simpson Weather Associates
SWIFT – Super-Wide Frequency-Tunable laser (Beyond Photonics)
TEC – Thermo-Electric Cooler
TEM – Transverse Electromagnetic
TFP – Thin Film Polarizer
TRL – Technology Readiness Level
3-D – Three Dimensional
T/R – Transmit/Receive
TRL – Technology Readiness Level
UTC - Coordinated Universal Time
UV - Ultraviolet
VIIRS – Visible Infrared Imaging Radiometer Suite

WDM – Wavelength Division Multiplexer
WFIP-3 – Wind Forecast Improvement Project – 3 (NOAA/Dept. of Energy)
WH^2YMSIE - Westcoast & Heartland Hyperspectral Microwave Sensor Intensive Experiment
WIND-SP – Wind Space Pathfinder (or SP)
WMO – World Meteorological Organization
WV – Water Vapor
Xmit - Transmit